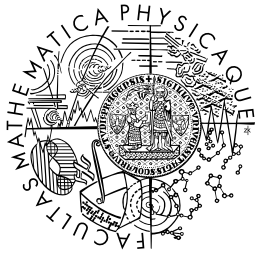

FACULTY
OF MATHEMATICS
AND PHYSICS
Charles University

MASTER THESIS

Bc. Michal Vančík

Physical properties of doped and non-doped $Tb_3Fe_5O_{12}$ studied by optical spectroscopies

Institute of Physics of Charles University

Supervisor of the master thesis: RNDr. Martin Veis, PhD.

Study programme: Physics

Study branch: Optics and optoelectronics

Prague 2022

I declare that I carried out this master thesis independently, and only with the cited sources, literature and other professional sources. It has not been used to obtain another or the same degree.

I understand that my work relates to the rights and obligations under the Act No. 121/2000 Sb., the Copyright Act, as amended, in particular the fact that the Charles University has the right to conclude a license agreement on the use of this work as a school work pursuant to Section 60 subsection 1 of the Copyright Act.

In ..... date ....

Author's signature

I would like to thank my supervisor, RNDr. Martin Veis, PhD., for his advices and patience during my work on this thesis. One big thank you goes to my girlfiend, parents and also my friends, who supported me during my study of physics.

Title: Physical properties of doped and non-doped $Tb_3Fe_5O_{12}$ studied by optical spectroscopies

Author: Bc. Michal Vančík

Institute: Institute of Physics of Charles University

Supervisor: RNDr. Martin Veis, PhD., Institute of Physics of Charles University

Abstract: This thesis focuses on systematic study of optical and magneto-optical properties of non-doped and doped $Tb_3Fe_5O_{12}$ thin films, on gadolinium gallium garnet and silicon substrates. Spectroscopic ellipsometry measurements were performed to obtain optical properties, thicknesses and surface roughness values of studied samples. The magneto-optical properties were investigated using the Kerr and Faraday effect measurements. Obtained experimental data were used to calculate the spectral dependence of the off-diagonal components of permittivity tensor. The results were compared with literature, and the effect of doping was discussed. On three samples, the spectral magneto-optical Kerr rotation hysteresis loops were measured, for the purpose of separating the individual contributions of sublattices. The analysis revealed that the method is probably insensitive to sublattice contributions but is sensitive to the contributions of regions with different magnetic anisotropy within the deposited layer.

Keywords: ferrimagnetic garnets magneto-optical spectroscopy sublattice contributions

Contents

Introduction **3**

1 Polarized light **5**
1.1 Wave equation . . . 5
1.2 Plane wave . . . 5
1.2.1 Conductive medium . . . 6
1.3 Polarization . . . 7
1.3.1 Polarization representation . . . 8
1.4 Magneto-optical angles . . . 11

2 Interaction of light and matter **13**
2.1 Reflection and refraction at an interface . . . 13
2.1.1 Reflection and refraction between absorbing media . . . 14
2.2 Permittivity tensor . . . 15
2.3 Wave equation in anisotropic media . . . 15
2.3.1 Propagation along magnetization vector . . . 16
2.4 Yeh formalism . . . 17
2.4.1 Eigenmodes in isotropic layers . . . 19
2.5 Reflection and transmission coefficients . . . 20
2.6 Microscopic origin of optical and magneto-optical response . . . 21
2.6.1 Lorentz model . . . 21
2.6.2 Tauc- and Cody-Lorentz models . . . 21
2.6.3 Drude model . . . 22
2.6.4 Magneto-optical transitions . . . 22
2.6.5 Kramers-Krönig relations . . . 24

3 Magnetism **26**
3.1 Diamagnetism . . . 26
3.2 Paramagnetism . . . 26
3.3 Exchange interaction . . . 27
3.4 Ferromagnetism . . . 28
3.5 Antiferromagnetism . . . 29
3.6 Ferrimagnetism . . . 29
3.7 Magnetic anisotropy . . . 29

4 Experimental techniques **32**
4.1 Spectroscopic ellipsometry . . . 32
4.2 Magneto-optical spectroscopies . . . 33
4.3 Pulsed laser deposition . . . 35

5 Studied samples **36**
5.1 Ferrimagnetic garnets . . . 36

6 Results and discussion **39**
6.1 Optical properties . . . 39
6.2 Magneto-optical properties . . . 44

7 Conclusion **58**

Bibliography **60**

List of Figures **65**

List of Acronyms **68**

Introduction

The ever increasing demand for computer technology in modern world requires computers to work faster and faster than before. One of the ways to increase the computational power is to make the transistors in microchips smaller, which increase the computational power density. This miniaturization, however, cannot be done indefinitely because of the heat generated by the transistors, eventually resulting in their damage. Another problem is that at nanoscale dimensions, the electrons can more easily tunnel through thin gates of the transistors, thus making them unreliable.

Nonentheless, there is a room for improvement elsewhere. One of the speed bottlenecks of computers are electric wires between individual components. The speed of the electrical signal inside the wires is significantly smaller than the speed of light. It is not surprising that the communication speed could be improved by replacing the wiring with optical waveguides. Furthermore, the information could be transmitted simultaneously at multiple wavelengths at the same time, increasing the performance even more. The goal is to scale down the existing optical communication solutions to the microscopic scale and integrate them on the silicon microchips.

One of the important components of such optical system is the magneto-optical (MO) isolator. This component can be thought of as a one way for the passing light. It plays an important role in preventing the back reflections from the optical components going into the laser that could destabilize it and therefore lower its performance. The principle of the MO isolator is based on the broken time reversal symmetry of light propagation via applied magnetic field. If circularly polarized light is passing through the magnetic material in one direction and then is reflected back, the rotation sense of the light changes direction and the light is exposed to different environment. This is equivalent to the reversal of the time direction, when the clockwise propagating light changes to anticlockwise.

One of the designs of MO isolator is illustrated in Fig. 1. The magneto-

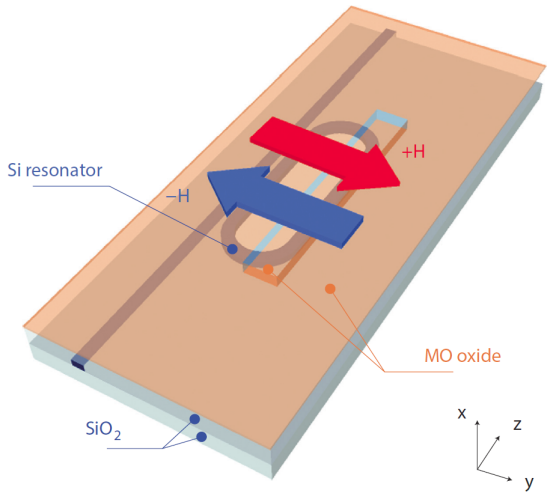

Figure 1: Structure of a non-reciprocal MO isolator. Taken from [1].

optical isolator consists of a silicon resonator on a silicon wafer with a thin SiO_2

layer with a small window that exposes the resonator waveguide. Then a thin layer of MO material is deposited on top. When a magnetic field is applied in-plane and perpendicular to the light propagation, the degeneracy of clockwise and counter-clockwise polarizations is lifted and results in a different phase shift of the two senses. As a result, the counter-clockwise polarization experiences larger transmission loss than the clockwise polarization (Fig. 2).

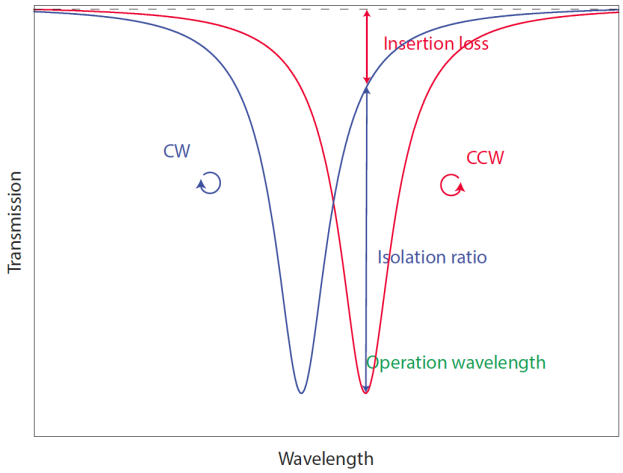

Figure 2: Spectral dependence of the transmission for two senses of circular polarization. Taken from [1].

One of the possible candidates for the MO film are ferrimagnetic rare-earth garnets with the formula $R^{3+}{}_3Fe^{3+}{}_5O^{2-}{}_{12}$, where R stands for rare-earth element. The garnets crystallize in a cubic lattice which consists of three sites defined by the oxygen positions: iron ions are situated in tetrahedral and octahedral sites, while the rare-earth sits at the dodecahedral site. Their magnetic and optical properties can be tailored by a variety of elemental substitutions. These materials exhibit large MO activity and are already used in macroscopic optical isolators [2]. One of the potential garnets with attractive properties is the terbium iron garnet (TbIG). The big advantage of terbium iron garnet is that it does not require a cladding layer for crystallization when grown on silicon substrates [3]. The effectivity of the isolation rapidly decreases with the distance of the MO film and the waveguide.

The purpose of this thesis is a systematic study of the optical and MO properties of the non-doped TbIG and TbIG doped with Ce and Bi on gadolinium gallium garnet (GGG) and silicon substrates. One of the goals is to separate the contributions of the individual sublattices to the MO spectra, which would broaden the knowledge about the complex properties of garnets.

This thesis is divided into seven chapters. The first three chapters describe the basic theory of light, its interaction with matter and magnetism of materials. Fourth chapter presents the measuring methods used in this thesis and a method of preparation of the studied samples. In the fifth chapter, the studied garnets are described in more detail. Next chapter contains the experimental results and their discussion. The last chapter presents the conclusions about the studied samples.

1. Polarized light

1.1 Wave equation

Light is an electromagnetic (EM) wave that can be described by two vectors, electric field $\boldsymbol{E}$ and magnetic induction $\boldsymbol{B}$. Two additional vectors, electric induction $\boldsymbol{D}$ and magnetic field strength $\boldsymbol{H}$ are introduced to describe EM wave inside matter. These four vectors fulfil Maxwell equations [4]

$$\begin{aligned} \nabla \times \boldsymbol{E} + \frac{\partial \boldsymbol{B}}{\partial t} = 0, \qquad & \nabla \cdot \boldsymbol{D} = \rho, \\ \nabla \times \boldsymbol{H} - \frac{\partial \boldsymbol{D}}{\partial t} = \boldsymbol{j}, \qquad & \nabla \cdot \boldsymbol{B} = 0, \end{aligned} \tag{1.1}$$

where $\boldsymbol{j}$ denotes current density and ρ charge density. Another set of equations, called material relations, that describe material response to EM fields, is needed to uniquely determine vectors $\boldsymbol{E}$, $\boldsymbol{B}$, $\boldsymbol{D}$ and $\boldsymbol{H}$. In the simple case, when medium is linear, isotropic and homogeneous, *dielectric permittivity* ε, *magnetic permeability* μ and *conductivity* σ are scalar constants and the equations are

$$\begin{aligned} \boldsymbol{D} &= \epsilon_0 \, \epsilon_\mathrm{r} \boldsymbol{E} = \epsilon \boldsymbol{E} = \varepsilon_0 \boldsymbol{E} + \boldsymbol{P}, \\ \boldsymbol{B} &= \mu_0 \, \mu_\mathrm{r} \boldsymbol{H} = \mu \boldsymbol{H} = \mu_0 \boldsymbol{H} + \boldsymbol{M}, \\ \boldsymbol{j} &= \sigma \boldsymbol{E}. \end{aligned} \tag{1.2}$$

Indices 0, r denote vacuum and relative constants, respectively, $\boldsymbol{M}$ medium magnetization, $\boldsymbol{P}$ medium polarization vectors.

A wave equation that describes the propagation of light can be derived from equations (1.1). In the simple case described above and without sources, the wave equation has the form

$$\Delta \boldsymbol{E} - \varepsilon \mu \frac{\partial^2 \boldsymbol{E}}{\partial t^2} = 0, \tag{1.3}$$

where Δ denotes the Laplace operator. An analogical equation can be derived for $\boldsymbol{H}$. Similarly to the classical wave equation, $v = \frac{1}{\sqrt{\varepsilon \mu}}$ is the speed at which the wave propagates, also called *phase velocity*. If light propagates in vacuum, the phase velocity $v = \frac{1}{\sqrt{\varepsilon_0 \mu_0}} = c = 299\,792\,458\,\mathrm{m} \cdot \mathrm{s}^{-1}$, which is a fundamental physical constant. The ratio

$$\frac{c}{v} = \sqrt{\varepsilon_\mathrm{r} \mu_\mathrm{r}} = n \tag{1.4}$$

is defined as the *index of refraction*.

1.2 Plane wave

One of the solutions of the wave equation (1.3) is a harmonic plane wave [5]

$$\boldsymbol{E}(\boldsymbol{r}, t) = \boldsymbol{E}_0 \cos\left[\omega t - \boldsymbol{k} \cdot \boldsymbol{r} + \delta\right],$$

where $\boldsymbol{E}_0$ denotes the electric field amplitude vector, ω angular frequency, δ phase shift. $\boldsymbol{k}$ is the wave vector defined as

$$\boldsymbol{k} = \frac{2\pi}{\lambda}\boldsymbol{s} = \frac{\omega}{c}n\boldsymbol{s},$$

where λ denotes wavelength and $\boldsymbol{s}$ is a unit vector pointing in the direction of wave propagation. For every instant in time, the plane wave has a constant phase across the plane determined by $\boldsymbol{r} \cdot \boldsymbol{s} = \text{const}$. These planes are perpendicular to the unit vector $\boldsymbol{s}$. For a homogeneous isotropic medium without charges and currents, the wave is *transverse*, i.e. vectors $\boldsymbol{s}$, $\boldsymbol{E}$, $\boldsymbol{B}$ constitute a right-handed coordinate system with relations between vectors

$$\boldsymbol{B} = \frac{1}{v}\boldsymbol{s} \times \boldsymbol{E}, \qquad \boldsymbol{s} \times \boldsymbol{B} = -\frac{1}{v}\boldsymbol{E}. \tag{1.5}$$

If the condition that the medium contains no free charges or currents is not satisfied, the wave is not generally transverse. The equations (1.5) also imply that the electric and magnetic vectors are always in phase. The plane wave is one of the most important solutions to the wave equation. According to Fourier analysis, any other waveform can be expressed as a linear combination of plane waves.

Usually, it is more convenient for mathematical operations if the plane wave is represented by complex numbers as

$$\boldsymbol{E}(\boldsymbol{r}, t) = \frac{1}{2}\left(\boldsymbol{E}_0 \mathrm{e}^{\mathrm{i}(\omega t - \boldsymbol{k}\cdot\boldsymbol{r} + \delta)} + \text{c.c.}\right), \tag{1.6}$$

where c.c. signifies the complex conjugate part. In the rest of this text the 1/2 and the letters c.c. will be omitted.

1.2.1 Conductive medium

For isotropic homogeneous conductive medium without charges, the wave equation (1.3) becomes

$$\Delta\boldsymbol{E} - \varepsilon\mu\frac{\partial^2\boldsymbol{E}}{\partial t^2} - \mu\sigma\frac{\partial\boldsymbol{E}}{\partial t} = 0.$$

Assuming harmonic wave solution (1.6), the wave equation can be written as

$$\Delta\boldsymbol{E} + \tilde{k}^2\boldsymbol{E} = 0,$$

where complex wave number

$$\tilde{k}^2 = \frac{\omega^2}{c^2}\mu_\mathrm{r}\tilde{\varepsilon}_\mathrm{r} = \left(k_\mathrm{R} - \mathrm{i}k_\mathrm{I}\right)^2, \tag{1.7}$$

and complex permittivity

$$\tilde{\varepsilon}_\mathrm{r} = \varepsilon_\mathrm{r} + \mathrm{i}\frac{\sigma}{\omega\varepsilon_0} = \varepsilon' - \mathrm{i}\varepsilon''$$

are introduced. At optical frequencies, relative permeability μ_r is close to 1, so $\mu = \mu_0$. The relation between relative permittivity and refractive index (1.4) becomes

$$\tilde{n}^2 = \tilde{\varepsilon}_\mathrm{r} = (n - \mathrm{i}k)^2 . \tag{1.8}$$

Substituting complex $\tilde{k}$ back into the plane wave solution (1.6), an attenuated wave is obtained

$$\boldsymbol{E}(\boldsymbol{r}, t) = \boldsymbol{E}_0 \mathrm{e}^{-\mathrm{i}(\omega t - \tilde{k}\boldsymbol{r}\cdot\boldsymbol{s})} = \boldsymbol{E}_0 \mathrm{e}^{-k_\mathrm{I}\boldsymbol{r}\cdot\boldsymbol{s}} \mathrm{e}^{-\mathrm{i}(\omega t - \boldsymbol{k}_\mathrm{R}\boldsymbol{r}\cdot\boldsymbol{s})}.$$

1.3 Polarization

For a fixed coordinate in space, the vectors will point in different directions for every instant in time. This time dependence is called *polarization* of the wave. It is common to choose the electric vector for the polarization description because the force exerted by the electric field on electrons is much larger than the force from the magnetic field.

According to (1.5), if the direction of propagation is along the z-direction, $\boldsymbol{E}$ has components only in the xy-plane

$$\begin{aligned} E_\mathrm{x}(z, t) &= E_{0_\mathrm{x}} \cos\left[\omega t - k_\mathrm{z} z + \delta_\mathrm{x}\right], \\ E_\mathrm{y}(z, t) &= E_{0_\mathrm{y}} \cos\left[\omega t - k_\mathrm{z} z + \delta_\mathrm{y}\right]. \end{aligned}$$

Rewriting these equations leads to the equation of an ellipse (Fig. 1.1)

$$\left(\frac{E_\mathrm{x}}{E_{0_\mathrm{x}}}\right)^2 - 2\frac{E_\mathrm{x}}{E_{0_\mathrm{x}}}\frac{E_\mathrm{y}}{E_{0_\mathrm{y}}}\cos\delta + \left(\frac{E_\mathrm{y}}{E_{0_\mathrm{y}}}\right)^2 = \sin^2\delta,$$

where $\delta = \delta_\mathrm{y} - \delta_\mathrm{x}$. Four quantities, E_{0_x}, E_{0_y}, δ_x, and δ_y are needed to completely describe the light polarization state.

In the case of general elliptical polarization, it is convenient to introduce different parameters that determine the polarization [6]:

- auxiliary angle $\alpha \in \left\langle 0, \frac{\pi}{2} \right\rangle$:

$$\tan\alpha = \frac{E_{0_\mathrm{x}}}{E_{0_\mathrm{y}}},$$

- the azimuth angle between the major axis of the ellipse and the x-axis $\theta \in \langle 0, \pi)$:

$$\tan 2\theta = \frac{2E_{0_\mathrm{x}}E_{0_\mathrm{y}}\cos\delta}{E_{0_\mathrm{x}}^2 - E_{0_\mathrm{y}}^2} = \tan(2\alpha)\cos\delta,$$

- the ellipticity angle $\epsilon \in \left\langle -\frac{\pi}{4}, \frac{\pi}{4} \right\rangle$:

$$\tan\epsilon = \mp\frac{b}{a}.$$

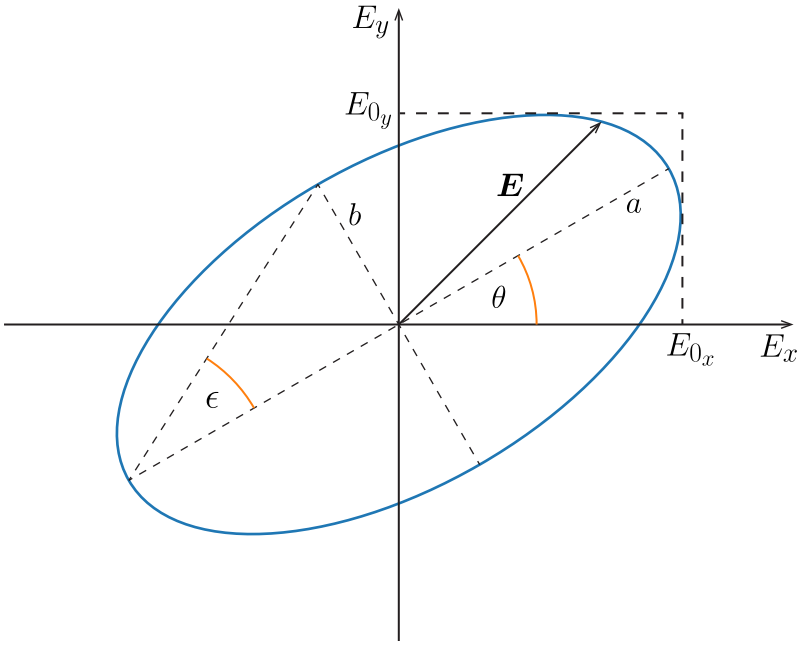

Figure 1.1: The polarization ellipse.

Additionally, the ellipse semiaxes and the components of the electric field amplitude satisfy relation $a^2 + b^2 = E_0^2 = E_{0_\mathrm{x}}^2 + E_{0_\mathrm{y}}^2$.

The electric field $\boldsymbol{E}$ can describe the ellipse in two senses. When looking against the propagation direction, the polarization is said to be *right-handed* for clockwise sense and *left-handed* for anti-clockwise sense. The handedness is indicated by the sign of the ellipticity angle ϵ, i.e. positive sign indicates right-handed polarization.

There are two special cases of light polarization of great importance (Fig. 1.2):

1. *linear polarization* for $\delta = 0$ or π:

   - for $\delta = 0$: $E_\mathrm{y} = \frac{E_{0_\mathrm{y}}}{E_{0_\mathrm{x}}} E_\mathrm{x}$
   - for $\delta = \pi$: $E_\mathrm{y} = -\frac{E_{0_\mathrm{y}}}{E_{0_\mathrm{x}}} E_\mathrm{x}$

   or if one component of $\boldsymbol{E}$ is equal to zero,

2. *circular polarization* for $E_{0_\mathrm{y}} = E_{0_\mathrm{x}}$ and $\delta = \pm\frac{\pi}{2}$ where the sign indicates *right-handed circular polarization* (RCP) and *left-handed circular polarization* (LCP) respectively.

1.3.1 Polarization representation

In physical experiments it is convenient to represent polarized light and effect of optical elements by vectors and matrices. The most used formalism for completely polarized light is *Jones formalism*.

Harmonic plane wave can be written as

$$E_\mathrm{x} = E_{0_\mathrm{x}} \mathrm{e}^{\mathrm{i}(\omega t - k_\mathrm{z} z + \delta_\mathrm{x})} = A_\mathrm{x} \mathrm{e}^{\mathrm{i}(\omega t - k_\mathrm{z} z)}, \quad \text{where } A_\mathrm{x} = E_{0_\mathrm{x}} \mathrm{e}^{\mathrm{i}\delta_\mathrm{x}}$$
$$E_\mathrm{y} = E_{0_\mathrm{y}} \mathrm{e}^{\mathrm{i}(\omega t - k_\mathrm{z} z + \delta_\mathrm{y})} = A_\mathrm{y} \mathrm{e}^{\mathrm{i}(\omega t - k_\mathrm{z} z)}, \quad \text{where } A_\mathrm{y} = E_{0_\mathrm{y}} \mathrm{e}^{\mathrm{i}\delta_\mathrm{y}}.$$

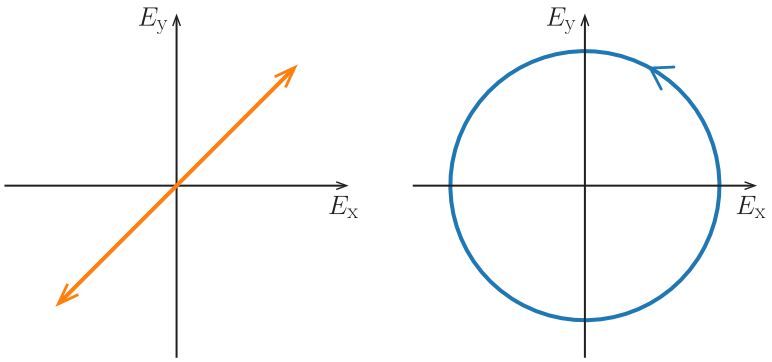

Figure 1.2: Examples of a) linear polarization and b) LCP.

The Jones polarization vector is then defined as

$$\boldsymbol{J} = \begin{pmatrix} A_x \\ A_y \end{pmatrix}. \tag{1.9}$$

To get the original wave, the Jones vector is simply multiplied by the phase factor $e^{i(\omega t - k_z z)}$. The light intensity $I \sim |A_x|^2 + |A_y|^2 = A_x^* A_x + A_y^* A_y = \boldsymbol{J}^\dagger \boldsymbol{J}$. Jones vectors are commonly normalized, so $I = 1$.

Some examples of Jones polarization vectors for various polarization states are given below:

- linear polarization along axes x, y, and rotated by arbitrary angle β with respect to x-axis

$$\boldsymbol{J}_x = \begin{pmatrix} 1 \\ 0 \end{pmatrix}, \qquad \boldsymbol{J}_y = \begin{pmatrix} 0 \\ 1 \end{pmatrix}, \qquad \boldsymbol{J}_\beta = \begin{pmatrix} \cos\beta \\ \sin\beta \end{pmatrix},$$

- RCP and LCP

$$\boldsymbol{J}_{\mathrm{RCP}} = \frac{1}{\sqrt{2}} \begin{pmatrix} 1 \\ i \end{pmatrix}, \qquad \boldsymbol{J}_{\mathrm{LCP}} = \frac{1}{\sqrt{2}} \begin{pmatrix} 1 \\ -i \end{pmatrix}, \tag{1.10}$$

- elliptical polarization with angle θ between major axis and x-axis and ellipticity angle ϵ

$$\boldsymbol{J}_{\theta,\varepsilon} = \begin{pmatrix} \cos\theta\cos\epsilon - i\sin\theta\sin\epsilon \\ \sin\theta\cos\epsilon + i\cos\theta\sin\epsilon \end{pmatrix}.$$

The sets of Jones vectors of linear polarizations along cartesian axes and circular polarizations are orthogonal. Therefore arbitrary polarization can be represented by a linear combination of two orthogonal polarization vectors forming a base.

Optical elements that modify the polarization state can be represented by Jones matrices in the form

$$\boldsymbol{T} = \begin{pmatrix} T_{11} & T_{12} \\ T_{21} & T_{22} \end{pmatrix}. \tag{1.11}$$

The new polarization state $\boldsymbol{J}'$ after interaction with the optical element is then

$$\boldsymbol{J}' = \boldsymbol{T}\boldsymbol{J}.$$

If n optical elements are arranged in a row, their respective matrices are multiplied in the order in which they interact with light

$$\boldsymbol{T} = \boldsymbol{T}_n \dots \boldsymbol{T}_2 \boldsymbol{T}_1.$$

Matrices for common optical elements are shown below:

1. linear polarizer along the x-axis and polarizer rotated by an arbitrary angle β
$$\boldsymbol{T}_{\mathrm{x}} = \begin{pmatrix} 1 & 0 \\ 0 & 0 \end{pmatrix}, \qquad \boldsymbol{T}_{\beta} = \begin{pmatrix} \cos^2\beta & \sin\beta\cos\beta \\ \sin\beta\cos\beta & \sin^2\beta \end{pmatrix},$$

2. phase plate, which introduces additional phase shift $\delta = \delta_{\mathrm{y}} - \delta_{\mathrm{x}}$
$$\boldsymbol{T}_{\delta} = \begin{pmatrix} 1 & 0 \\ 0 & \mathrm{e}^{\mathrm{i}\delta} \end{pmatrix},$$

3. polarization rotator, which rotates the polarization plane by angle γ
$$\boldsymbol{T}_{\gamma} = \begin{pmatrix} \cos\gamma & -\sin\gamma \\ \sin\gamma & \cos\gamma \end{pmatrix}.$$

Often, the optical elements are rotated with respect to the coordinate system. In that case, the Jones matrix of the element must be multiplied by the coordinate rotation matrix and its inverse

$$\boldsymbol{T}(\alpha) = \boldsymbol{R}^{-1}(\alpha)\boldsymbol{T}\boldsymbol{R}(\alpha),$$

where

$$\boldsymbol{R}(\alpha) = \begin{pmatrix} \cos\alpha & \sin\alpha \\ -\sin\alpha & \cos\alpha \end{pmatrix}, \qquad \boldsymbol{R}^{-1}(\alpha) = \begin{pmatrix} \cos\alpha & -\sin\alpha \\ \sin\alpha & \cos\alpha \end{pmatrix}.$$

A simpler description of polarized light can be used if the amplitude and absolute phase information is not needed. Only azimuth angle θ and ellipticity angle ε are essential to describe the state of the polarization. A new parameter can be defined as the ratio of the components of the Jones vector [7]

$$\chi = \frac{A_{\mathrm{x}}}{A_{\mathrm{y}}}.$$

For general elliptical polarization

$$\chi = \frac{\tan\theta + \mathrm{i}\tan\epsilon}{1 - \mathrm{i}\tan\theta\tan\epsilon}. \tag{1.12}$$

By limiting the angles to ranges $-\frac{1}{2}\pi \leq \theta \leq \frac{1}{2}\pi$ and $-\frac{1}{4}\pi \leq \epsilon \leq \frac{1}{4}\pi$, every polarization state can be uniquely represented by the complex parameter χ.

1.4 Magneto-optical angles

Materials placed in an external magnetic field become optically anisotropic and therefore modify reflected and transmitted light. The material can be described by Jones matrices. The coordinate system is chosen with respect to two orthogonal linear polarizations. The polarization parallel to the plane of incidence is called *p*-polarization, and the polarization perpendicular is called *s*-polarization. The plane of incidence is defined by the wave vector of the incoming wave and the normal to the surface. The Jones matrices for the sample transmission and reflection take the form

$$\boldsymbol{T} = \begin{pmatrix} t_{\mathrm{ss}} & t_{\mathrm{sp}} \\ t_{\mathrm{ps}} & t_{\mathrm{pp}} \end{pmatrix}, \qquad \boldsymbol{R} = \begin{pmatrix} r_{\mathrm{ss}} & r_{\mathrm{sp}} \\ r_{\mathrm{ps}} & r_{\mathrm{pp}} \end{pmatrix}. \tag{1.13}$$

The elements of the matrices are the transmission and reflection coefficients for the s- and p-polarizations and are described in the following chapter.

The output polarization, which will generally be elliptical, can be described by the complex parameter χ (1.12). It is advantageous to use linear incident polarization for which azimuth angle θ is equal to 0 or π, and ellipticity angle is $\epsilon = 0$. This way, it is easy to determine the change of θ and ϵ caused by the magnetization of the sample in the resulting polarization. Additionally, if the polarization is not chosen carefully, it can change by simple reflection or refraction at an interface.

Usually, the angles are small and an approximation can be made

$$\chi = \frac{\tan\theta + \mathrm{i}\tan\epsilon}{1 - \mathrm{i}\tan\theta\tan\epsilon} \approx \theta + \mathrm{i}\epsilon.$$

The change of polarization upon reflection is called the *magneto-optical Kerr effect* (MOKE) and is defined as [6]

$$\begin{aligned} \Phi_{\mathrm{K_s}} &= -\frac{r_{\mathrm{ps}}}{r_{\mathrm{ss}}} \approx \theta_{\mathrm{K_s}} - \mathrm{i}\epsilon_{\mathrm{K_s}}, \\ \Phi_{\mathrm{K_p}} &= \frac{r_{\mathrm{sp}}}{r_{\mathrm{pp}}} \approx \theta_{\mathrm{K_p}} - \mathrm{i}\epsilon_{\mathrm{K_p}}, \end{aligned} \tag{1.14}$$

for incident s and p polarization, respectively. Similarly, the change after transmission, called the *Faraday effect*, is defined as

$$\begin{aligned} \Phi_{\mathrm{F_s}} &= \frac{t_{\mathrm{ps}}}{t_{\mathrm{ss}}} \approx \theta_{\mathrm{F_s}} - \mathrm{i}\epsilon_{\mathrm{F_s}}, \\ \Phi_{\mathrm{F_p}} &= -\frac{t_{\mathrm{sp}}}{t_{\mathrm{pp}}} \approx \theta_{\mathrm{F_p}} - \mathrm{i}\epsilon_{\mathrm{F_p}}. \end{aligned} \tag{1.15}$$

There are three basic configurations of measuring MOKE that are defined by the mutual orientations of the sample, magnetization $\boldsymbol{M}$ and the propagation vector (Fig. 1.3). The $\boldsymbol{M}$ and the propagation vector are parallel to each other, and perpendicular to the sample in the polar configuration. For the longitudinal configuration, $\boldsymbol{M}$ lies in the plane of the sample and the plane of incidence. Finally, for the transverse geometry, $\boldsymbol{M}$ is in the plane of the sample but perpendicular to the plane of incidence. Faraday effect is measured only in polar configuration at normal incidence.

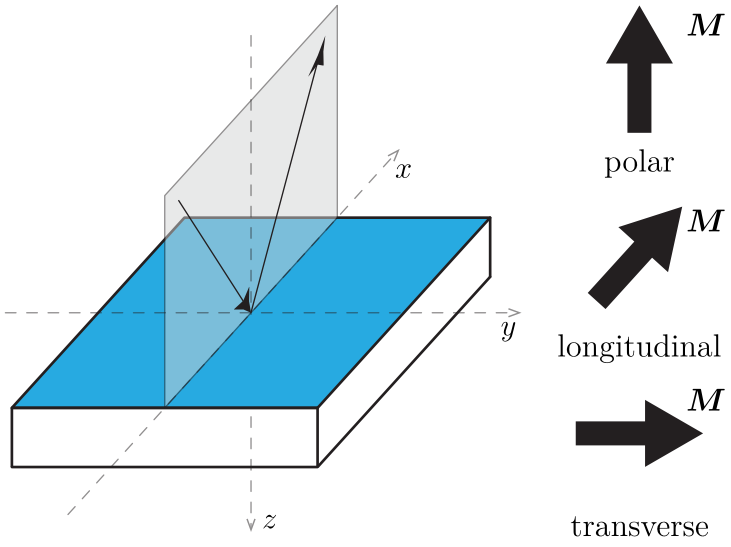

Figure 1.3: Basic configurations of measuring MOKE.

2. Interaction of light and matter

2.1 Reflection and refraction at an interface

The interface between two media introduces an abrupt change of optical constants (e.g. ε, σ, etc.). Therefore, the behaviour of the propagating wave also has to change. This change is often exploited in physical measurements to obtain information about the media that compromise the interface.

At the interface of two homogeneous isotropic dielectric media with different refractive indices n_1 and n_2, three waves can be defined (Fig. 2.1):

- the incident wave $\boldsymbol{E}_\mathrm{i}$ on the interface at an angle α_i,
- the wave $\boldsymbol{E}_\mathrm{t}$ transmitted at an angle α_t,
- the wave $\boldsymbol{E}_\mathrm{r}$ reflected at an angle α_r.

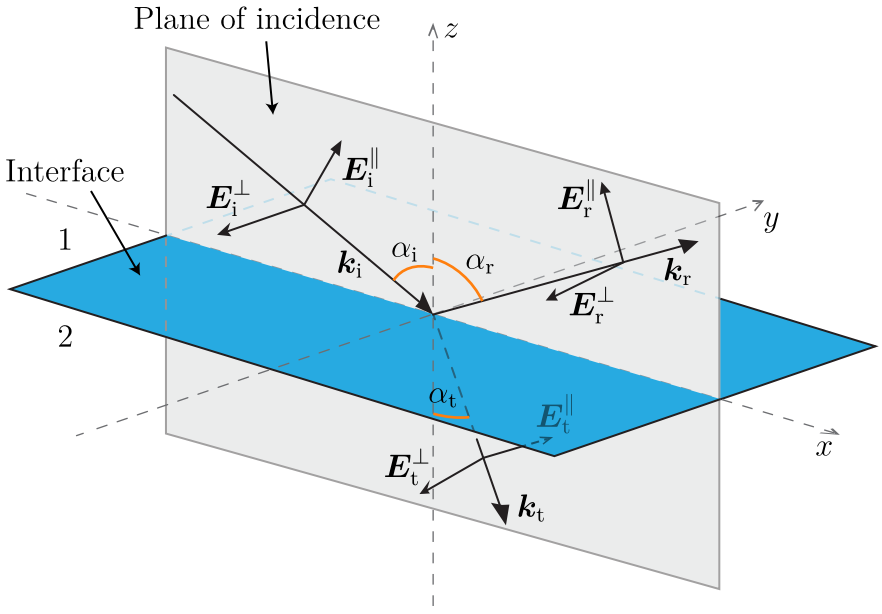

Figure 2.1: Reflection and refraction at an interface, field orientations.

All three waves lie in the plane of incidence, defined by the vector $\boldsymbol{k}_\mathrm{i}$ of the incoming wave and the normal to the surface. The angles are related through the law of reflection

$$\alpha_\mathrm{i} = \alpha_\mathrm{r}$$

and Snell's law

$$n_1 \sin \alpha_\mathrm{i} = n_2 \sin \alpha_\mathrm{t}. \tag{2.1}$$

The amplitudes of transmitted and reflected waves are dictated by *Fresnel equations*. They are a consequence of boundary conditions imposed on electric and magnetic fields. The boundary conditions require the tangent components of the fields to be continuous at the boundary. Since the magnitude of the tangent

component depends on the vector orientation, Fresnel equations differentiate between p-polarization ($\parallel$) and s-polarization ($\perp$). The reflection and transmission coefficients take the form [5] (Fig. 2.2)

$$\begin{aligned} r^{\mathrm{p}} &= \frac{E_{\mathrm{r}}^{\mathrm{p}}}{E^{\mathrm{p}}} = \frac{n_2 \cos\alpha_{\mathrm{i}} - n_1 \cos\alpha_{\mathrm{t}}}{n_2 \cos\alpha_{\mathrm{i}} + n_1 \cos\alpha_{\mathrm{t}}}, \\ r^{\mathrm{s}} &= \frac{E_{\mathrm{r}}^{\mathrm{s}}}{E^{\mathrm{s}}} = \frac{n_1 \cos\alpha_{\mathrm{i}} - n_2 \cos\alpha_{\mathrm{t}}}{n_1 \cos\alpha_{\mathrm{i}} + n_2 \cos\alpha_{\mathrm{t}}}, \\ t^{\mathrm{p}} &= \frac{E_{\mathrm{t}}^{\mathrm{p}}}{E^{\mathrm{p}}} = \frac{2n_1 \cos\alpha_{\mathrm{i}}}{n_2 \cos\alpha_{\mathrm{i}} + n_1 \cos\alpha_{\mathrm{t}}}, \\ t^{\mathrm{s}} &= \frac{E_{\mathrm{t}}^{\mathrm{s}}}{E^{\mathrm{s}}} = \frac{2n_1 \cos\alpha_{\mathrm{i}}}{n_1 \cos\alpha_{\mathrm{i}} + n_2 \cos\alpha_{\mathrm{t}}}. \end{aligned} \tag{2.2}$$

The reflectance and transmittance, the intensity coefficients, are given as

$$\begin{aligned} R^{\mathrm{s,p}} &= \left(r^{\mathrm{s,p}}\right)^2, \\ T^{\mathrm{s,p}} &= \frac{n_2 \cos\alpha_{\mathrm{t}}}{n_1 \cos\alpha_{\mathrm{i}}} \left(t^{\mathrm{s,p}}\right)^2, \end{aligned}$$

and for non-absorbing medium $1 = R + T$.

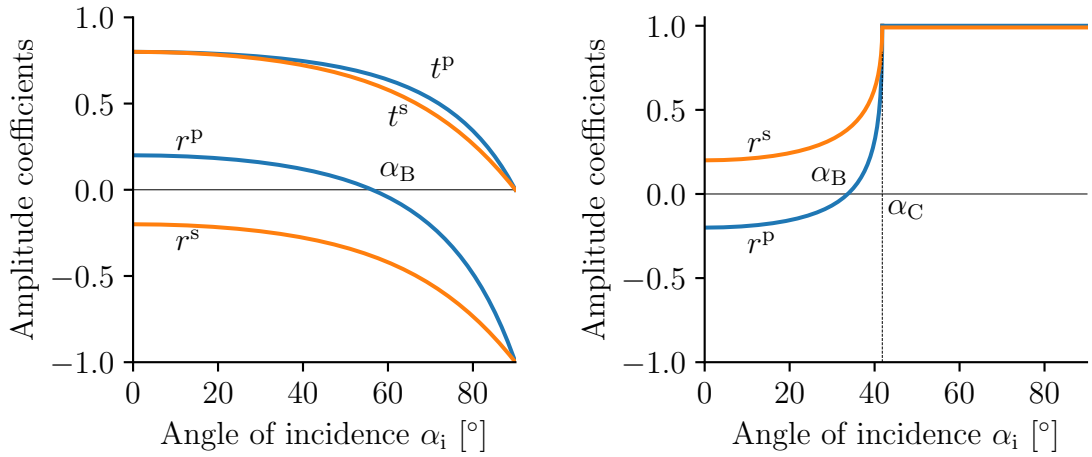

Figure 2.2: Reflection and transmission coefficients for $n_1 = 1$, $n_2 = 1.5$ (left), reflection coefficients for $n_1 = 1.5$, $n_2 = 1$ (right).

In the case of $n_1 > n_2$, the light overgoes *total internal reflection* at angles greater than *critical angle* α_{C}, i.e. all the incoming light is reflected. There is no reflected p-polarization for both cases ($n_1 > n_2$ and $n_1 < n_2$) at the *Brewster angle* (see Fig. 2.2).

2.1.1 Reflection and refraction between absorbing media

In the case of absorbing media, the situation is more complicated [8]. The conditions for transversality of the wave (1.5) hold for the complex wave vector. Because of this, the planes of constant phase do not coincide with planes of constant amplitude. The direction of propagation is determined by the real part of the Poynting vector $\boldsymbol{S} = \boldsymbol{E} \times \boldsymbol{H}^*/2$. Snell's law (2.1) and Fresnel equations (2.2)

imply that the angles and Fresnel coefficients are complex quantities. Consequently, an incident linear polarization can change to elliptical upon reflection and refraction at an interface.

2.2 Permittivity tensor

In the previous chapter, the permittivity was assumed to be a scalar quantity. In general, the permittivity is a tensor of second order

$$\boldsymbol{\varepsilon} = \begin{pmatrix} \varepsilon_{\mathrm{xx}} & \varepsilon_{\mathrm{xy}} & \varepsilon_{\mathrm{xz}} \\ \varepsilon_{\mathrm{yx}} & \varepsilon_{\mathrm{yy}} & \varepsilon_{\mathrm{yz}} \\ \varepsilon_{\mathrm{zx}} & \varepsilon_{\mathrm{zy}} & \varepsilon_{\mathrm{zz}} \end{pmatrix}. \tag{2.3}$$

The permittivity of an isotropic material can be considered a diagonal tensor where all three diagonal values are equal. If the material is placed in an external magnetic field, a non-zero net magnetization $\boldsymbol{M}$ is induced. The magnetization reduces the symmetry, and off-diagonal tensor elements will be non-zero. The external magnetic field can be treated as a small disturbance to the diagonal permittivity tensor. The permittivity tensor can then be expanded as a series with respect to magnetization [9]

$$\varepsilon_{ij} = \varepsilon_{ij}^{(0)} + K_{ijk} M_k + \frac{1}{2} G_{ijkl} M_k M_l + \ldots,$$

where K_{ijk} and G_{ijkl} are linear and quadratic contribution tensors. If only the linear MO effects are discussed, including just the linear contribution tensor is sufficient. Owing to the antisymmetric nature of the tensor, the diagonal elements remain unchanged. Consequently, depending on the magnetization orientation (Fig. 1.3), the diagonal permittivity tensor changes to

$$\boldsymbol{\varepsilon}_{\mathrm{P}} \approx \begin{pmatrix} \varepsilon_{\mathrm{xx}} & \varepsilon_{\mathrm{xy}} & 0 \\ -\varepsilon_{\mathrm{xy}} & \varepsilon_{\mathrm{xx}} & 0 \\ 0 & 0 & \varepsilon_{\mathrm{xx}} \end{pmatrix}, \quad \boldsymbol{\varepsilon}_{\mathrm{L}} \approx \begin{pmatrix} \varepsilon_{\mathrm{xx}} & 0 & -\varepsilon_{\mathrm{xz}} \\ 0 & \varepsilon_{\mathrm{xx}} & 0 \\ \varepsilon_{\mathrm{xz}} & 0 & \varepsilon_{\mathrm{xx}} \end{pmatrix}, \quad \boldsymbol{\varepsilon}_{\mathrm{T}} \approx \begin{pmatrix} \varepsilon_{\mathrm{xx}} & 0 & 0 \\ 0 & \varepsilon_{\mathrm{xx}} & \varepsilon_{\mathrm{yz}} \\ 0 & -\varepsilon_{\mathrm{yz}} & \varepsilon_{\mathrm{xx}} \end{pmatrix}. \tag{2.4}$$

The off-diagonal elements can naturally arise in anisotropic materials. In magneto-optics, the diagonal and off-diagonal elements are sometimes labelled as (in polar geometry, e.g.) $\varepsilon_{\mathrm{xx}} = \varepsilon_1$ and $\varepsilon_{\mathrm{xy}} = -\mathrm{i}\varepsilon_2$ to distinguish the origin in the magnetization[10].

2.3 Wave equation in anisotropic media

The first step in describing the MO response of anisotropic media is solving the wave equation (1.3) with general permittivity tensor (2.3) [9]

$$\Delta \boldsymbol{E} - \nabla \left(\nabla \cdot \boldsymbol{E} \right) = \frac{\boldsymbol{\varepsilon}}{c^2} \frac{\partial^2 \boldsymbol{E}}{\partial t^2}. \tag{2.5}$$

Assuming plane wave solution (1.6)

$$\boldsymbol{E}(\boldsymbol{r}, t) = \boldsymbol{E}_0 \mathrm{e}^{\mathrm{i}(\omega t - \boldsymbol{k}\cdot\boldsymbol{r})}$$

and introducing *reduced wave vector*

$$\boldsymbol{N} = \frac{c}{\omega}\boldsymbol{k} = \left(N_\mathrm{x}\boldsymbol{e}_\mathrm{x} + N_\mathrm{y}\boldsymbol{e}_\mathrm{y} + N_\mathrm{z}\boldsymbol{e}_\mathrm{z}\right),$$

where vectors $\boldsymbol{e}_{\mathrm{x,y,z}}$ denote Cartesian unit vectors, the wave equation (2.5) becomes

$$\boldsymbol{N}^2\boldsymbol{E}_0 - \boldsymbol{N}\left(\boldsymbol{N}\cdot\boldsymbol{E}_0\right) - \boldsymbol{\varepsilon}\boldsymbol{E}_0 = 0.$$

In matrix form, this can be written as

$$\begin{pmatrix} \varepsilon_{\mathrm{xx}} - N_\mathrm{y}^2 - N_\mathrm{z}^2 & \varepsilon_{\mathrm{xy}} + N_\mathrm{x}N_\mathrm{y} & \varepsilon_{\mathrm{xz}} - N_\mathrm{x}N_\mathrm{z} \\ \varepsilon_{\mathrm{yx}} + N_\mathrm{y}N_\mathrm{x} & \varepsilon_{\mathrm{yy}} - N_\mathrm{x}^2 - N_\mathrm{z}^2 & \varepsilon_{\mathrm{yz}} - N_\mathrm{y}N_\mathrm{z} \\ \varepsilon_{\mathrm{zx}} + N_\mathrm{z}N_\mathrm{x} & \varepsilon_{\mathrm{zy}} + N_\mathrm{z}N_\mathrm{y} & \varepsilon_{\mathrm{zz}} - N_\mathrm{x}^2 - N_\mathrm{y}^2 \end{pmatrix} \begin{pmatrix} E_{0\mathrm{x}} \\ E_{0\mathrm{y}} \\ E_{0\mathrm{z}} \end{pmatrix} = 0. \tag{2.6}$$

Without loss of generality, the coordinate system can be oriented such that $N_\mathrm{x} = 0$. This condition greatly simplifies the wave equation. The value of N_y can be obtained from Snell's law

$$\boldsymbol{k}\cdot\boldsymbol{e}_\mathrm{y} = \frac{\omega}{c}N_\mathrm{y}.$$

The equation system has a non-trivial solution when the determinant of the matrix is zero. Solving the characteristic equation leads to four eigenvalues of $N_{\mathrm{z}j}$ and four eigenvectors $\boldsymbol{e}_j$, $j = 1, 2, 3, 4$. The eigenvectors have the form [6]

$$\boldsymbol{e}_j = \begin{pmatrix} -\varepsilon_{\mathrm{xy}}\left(\varepsilon_{\mathrm{zz}} - N_\mathrm{y}^2\right) + \varepsilon_{\mathrm{xz}}\left(\varepsilon_{\mathrm{zy}} + N_\mathrm{y}N_{\mathrm{z}j}\right) \\ \left(\varepsilon_{\mathrm{zz}} - N_\mathrm{y}^2\right)\left(\varepsilon_{\mathrm{xx}} - N_\mathrm{y}^2 - N_{\mathrm{z}j}^2\right) - \varepsilon_{\mathrm{xz}}\varepsilon_{\mathrm{zx}} \\ -\left(\varepsilon_{\mathrm{xx}} - N_\mathrm{y}^2 - N_{\mathrm{z}j}^2\right)\left(\varepsilon_{\mathrm{zy}} + N_\mathrm{y}N_{\mathrm{z}j}\right) + \varepsilon_{\mathrm{zx}}\varepsilon_{\mathrm{xy}} \end{pmatrix}. \tag{2.7}$$

The general solution for the electric field is given by the sum of the four eigenmodes

$$\boldsymbol{E} = \sum_{j=1}^{4} E_{0j}\boldsymbol{e}_j \mathrm{e}^{\mathrm{i}\left(\omega t - \frac{\omega}{c}\left(N_\mathrm{y}y + N_{\mathrm{z}j}z\right)\right)}. \tag{2.8}$$

From the Maxwell equations follows the relation for magnetic field

$$\boldsymbol{B} = \frac{1}{c}\boldsymbol{N}\times\boldsymbol{E}. \tag{2.9}$$

2.3.1 Propagation along magnetization vector

The simplest case occurs for polar configuration. The permittivity tensor takes the form $\boldsymbol{\varepsilon}_\mathrm{P}$ as in (2.4). For normal incidence $N_\mathrm{y} = 0$, wave equation (2.6) becomes

$$\begin{pmatrix} \varepsilon_{\mathrm{xx}} - N_\mathrm{z}^2 & \varepsilon_{\mathrm{xy}} & 0 \\ -\varepsilon_{\mathrm{xy}} & \varepsilon_{\mathrm{xx}} - N_\mathrm{z}^2 & 0 \\ 0 & 0 & \varepsilon_{\mathrm{xx}} \end{pmatrix} \begin{pmatrix} E_{0\mathrm{x}} \\ E_{0\mathrm{y}} \\ E_{0\mathrm{z}} \end{pmatrix} = 0.$$

The solutions to the characteristic equation are then

$$N_\mathrm{z}^2 = \varepsilon_{\mathrm{xx}} \pm \mathrm{i}\varepsilon_{\mathrm{xy}}. \tag{2.10}$$

The solutions represent effective refractive indices for propagating eigenmodes. The eigenvectors corresponding to the eigenvalues are RCP and LCP modes and can be described by their respective Jones vectors (1.10). The four eigenmodes form two pairs. One pair propagates forward while the other propagates backwards, so the two pairs only differ in the sign of N_z.

Non-normal incidence

The equation for polar geometry can be solved without the condition $N_\mathrm{y} = 0$. The solutions (2.10) change to

$$N_\mathrm{z}^2 = \left(\varepsilon_\mathrm{xx} - N_\mathrm{y}^2\right) \pm \mathrm{i}\varepsilon_\mathrm{xy}\sqrt{\frac{\varepsilon_\mathrm{xx} - N_\mathrm{y}^2}{\varepsilon_\mathrm{xx}}}.$$

Upon taking the square roots, this becomes

$$N_{\mathrm{z}\pm} = N_\mathrm{z0}\sqrt{1 \pm \frac{\mathrm{i}\varepsilon_\mathrm{xy}}{N_\mathrm{z0}\sqrt{\varepsilon_\mathrm{xx}}}},$$

where

$$N_\mathrm{z0} = \sqrt{\varepsilon_\mathrm{xx} - N_\mathrm{y}^2}$$

is the z-component of the isotropic reduced wave vector.

The four roots have corresponding eigenvectors obtained from the general solution (2.7)

$$\boldsymbol{e}_j = \begin{pmatrix} -\varepsilon_\mathrm{xy}\left(\varepsilon_\mathrm{zz} - N_\mathrm{y}^2\right) \\ \left(\varepsilon_\mathrm{zz} - N_\mathrm{y}^2\right)\left(\varepsilon_\mathrm{xx} - N_\mathrm{y}^2 - N_{\mathrm{z}j}^2\right) \\ -\left(\varepsilon_\mathrm{xx} - N_\mathrm{y}^2 - N_{\mathrm{z}j}^2\right) N_\mathrm{y} N_{\mathrm{z}j} \end{pmatrix}$$

2.4 Yeh formalism

One way to describe the propagation of EM waves in anisotropic multilayers is a 4×4 matrix formalism developed by Yeh [11] for non-absorbing media and later extended for absorbing media by Višňovský [12]. This formalism uses the results presented in the previous section for anisotropic media and describes the propagation of eigenmodes through the stratified structure.

Consider a structure consisting of N anisotropic layers with thicknesses t_j and complex permittivity tensors $\boldsymbol{\varepsilon}_j$, $j = 1, \ldots, N$. The layers are separated by parallel interfaces whose normals point in the z-direction. Semi-infinite isotropic media labelled 0 and $N + 1$ surround the structure (Fig. 2.3). The components parallel to the interfaces must be conserved for the whole structure due to Snell's law and continuous at the interfaces because of the boundary conditions.

According to equation (2.8), the electric field inside the n-th layer is given as

$$\boldsymbol{E}^{(n)} = \sum_{j=1}^{4} E_{0j}^{(n)}(z_n)\boldsymbol{e}_j^{(n)} \mathrm{e}^{\mathrm{i}\left(\omega t - \frac{\omega}{c}\left(N_\mathrm{y} y + N_{\mathrm{z}j}^{(n)}(z - z_n)\right)\right)}$$

and the magnetic field as in (2.9)

$$\boldsymbol{B}^{(n)} = \frac{1}{c}\sum_{j=1}^{4} E_{0j}^{(n)}(z_n)\boldsymbol{b}_j^{(n)} \mathrm{e}^{\mathrm{i}\left(\omega t - \frac{\omega}{c}\left(N_\mathrm{y} y + N_{\mathrm{z}j}^{(n)}(z - z_n)\right)\right)},$$

where

$$\boldsymbol{b}_j^{(n)} = \boldsymbol{N}^{(n)} \times \boldsymbol{e}_j^{(n)}.$$

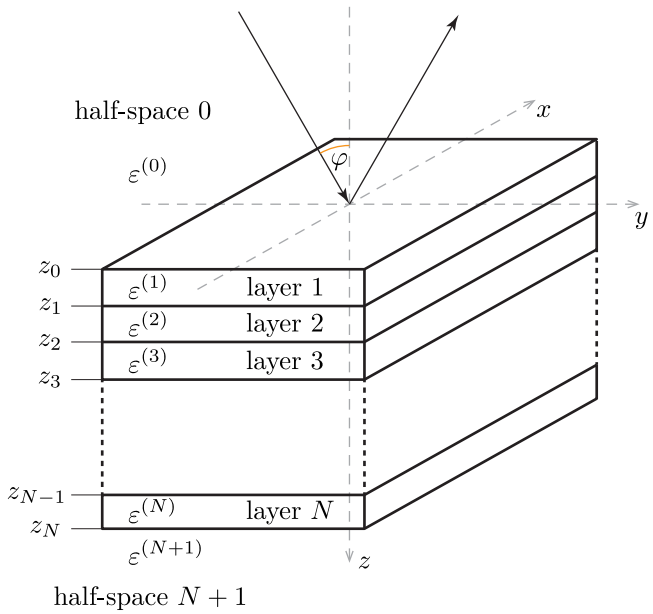

Figure 2.3: Multilayer structure consisting of N layers surrounded by 0 and $N+1$ half-spaces.

The boundary conditions require the tangential components to be equal at the interface of adjacent layers $n-1$ and n leading to

$$\begin{aligned}
\sum_{j=1}^{4} E_{0j}^{(n-1)}(z_{n-1})\boldsymbol{e}_j^{(n-1)} \cdot \boldsymbol{e}_{\mathrm{x}} &= \sum_{j=1}^{4} E_{0j}^{(n)}(z_n)\boldsymbol{e}_j^{(n)} \cdot \boldsymbol{e}_{\mathrm{x}}\, \mathrm{e}^{\mathrm{i}\frac{\omega}{c}N_{\mathrm{z}j}^{(n)}t_n} \\
\sum_{j=1}^{4} E_{0j}^{(n-1)}(z_{n-1})\boldsymbol{b}_j^{(n-1)} \cdot \boldsymbol{e}_{\mathrm{y}} &= \sum_{j=1}^{4} E_{0j}^{(n)}(z_n)\boldsymbol{b}_j^{(n)} \cdot \boldsymbol{e}_{\mathrm{y}}\, \mathrm{e}^{\mathrm{i}\frac{\omega}{c}N_{\mathrm{z}j}^{(n)}t_n} \\
\sum_{j=1}^{4} E_{0j}^{(n-1)}(z_{n-1})\boldsymbol{e}_j^{(n-1)} \cdot \boldsymbol{e}_{\mathrm{y}} &= \sum_{j=1}^{4} E_{0j}^{(n)}(z_n)\boldsymbol{e}_j^{(n)} \cdot \boldsymbol{e}_{\mathrm{y}}\, \mathrm{e}^{\mathrm{i}\frac{\omega}{c}N_{\mathrm{z}j}^{(n)}t_n} \\
\sum_{j=1}^{4} E_{0j}^{(n-1)}(z_{n-1})\boldsymbol{b}_j^{(n-1)} \cdot \boldsymbol{e}_{\mathrm{x}} &= \sum_{j=1}^{4} E_{0j}^{(n)}(z_n)\boldsymbol{b}_j^{(n)} \cdot \boldsymbol{e}_{\mathrm{x}}\, \mathrm{e}^{\mathrm{i}\frac{\omega}{c}N_{\mathrm{z}j}^{(n)}t_n}
\end{aligned}$$

This set of equations can be represented by matrix multiplication as

$$\mathbf{D}^{(n-1)}\boldsymbol{E}_0^{(n-1)} = \mathbf{D}^{(n)}\mathbf{P}^{(n)}\boldsymbol{E}_0^{(n)}. \tag{2.11}$$

The rows of the *dynamical matrix* $\mathbf{D}$ are constructed from components of the eigenvectors

$$\begin{aligned}
D_{1j}^{(n)} &= \boldsymbol{e}_j^{(n)} \cdot \boldsymbol{e}_{\mathrm{x}}, \\
D_{2j}^{(n)} &= \boldsymbol{b}_j^{(n)} \cdot \boldsymbol{e}_{\mathrm{y}}, \\
D_{3j}^{(n)} &= \boldsymbol{e}_j^{(n)} \cdot \boldsymbol{e}_{\mathrm{y}}, \\
D_{4j}^{(n)} &= \boldsymbol{b}_j^{(n)} \cdot \boldsymbol{e}_{\mathrm{x}}.
\end{aligned}$$

The exponential propagation factors through the layer are included in the diagonal *propagation matrix* $\mathbf{P}$

$$P_{ij}^{(n)} = \delta_{ij}\mathrm{e}^{\mathrm{i}\frac{\omega}{c}N_{\mathrm{z}j}^{(n)}t_n}.$$

For the polar configuration (ε_{P} in (2.4)), the rows of the dynamical matrix become

$$\begin{aligned}
D_{1j}^{(n)} &= -\varepsilon_{\mathrm{xy}}^{(n)} \left(\varepsilon_{\mathrm{zz}}^{(n)} - N_{\mathrm{y}}^2\right), \\
D_{2j}^{(n)} &= -\varepsilon_{\mathrm{xy}}^{(n)} \left(\varepsilon_{\mathrm{zz}}^{(n)} - N_{\mathrm{y}}^2\right) N_{zj}^{(n)}, \\
D_{3j}^{(n)} &= \left(\varepsilon_{\mathrm{zz}}^{(n)} - N_{\mathrm{y}}^2\right) \left(\varepsilon_{\mathrm{xx}}^{(n)} - N_{\mathrm{y}}^2 - \left(N_{zj}^{(n)}\right)^2\right), \\
D_{4j}^{(n)} &= -\left(\varepsilon_{\mathrm{xx}}^{(n)} - N_{\mathrm{y}}^2 - \left(N_{zj}^{(n)}\right)^2\right) N_{zj}^{(n)} \varepsilon_{\mathrm{xx}}^{(n)}.
\end{aligned}$$

The matrices in equation (2.11) can be rearranged to get

$$\boldsymbol{E}_0^{(n-1)} = \left(\mathbf{D}^{(n-1)}\right)^{-1} \mathbf{D}^{(n)} \mathbf{P}^{(n)} \boldsymbol{E}_0^{(n)} = \mathbf{T}_{n-1,n} \boldsymbol{E}_0^{(n)}.$$

The *transfer matrix* $\mathbf{T}$ relates the field at the interface $z = z^{(n-1)}$ of the $(n-1)$-th layer and field at $z = z^{(n)}$ in the n-th layer. By multiplying the transfer matrices for each layer, the fields at the surrounding half-spaces can be related

$$\begin{aligned}
\boldsymbol{E}_0^{(0)} = \left(\mathbf{D}^{(0)}\right)^{-1} \mathbf{D}^{(1)} \mathbf{P}^{(1)} \left(\mathbf{D}^{(1)}\right)^{-1} \mathbf{D}^{(2)} \mathbf{P}^{(2)} \dots \\
\dots \left(\mathbf{D}^{(N-1)}\right)^{-1} \mathbf{D}^{(N)} \mathbf{P}^{(N)} \left(\mathbf{D}^{(N)}\right)^{-1} \mathbf{D}^{(N+1)} \boldsymbol{E}_0^{(N+1)}.
\end{aligned}$$

The last transfer matrix consists only of the dynamical matrices since the thickness is undefined

$$\mathbf{T}_{N,N+1} = \left(\mathbf{D}^{(N)}\right)^{-1} \mathbf{D}^{(N+1)}.$$

The multiplication of transfer matrices can be expressed as

$$\boldsymbol{E}_0^{(0)} = \left(\prod_{n=1}^{N+1} \mathbf{T}_{n-1,n}\right) \boldsymbol{E}_0^{(N+1)} = \mathbf{M} \boldsymbol{E}_0^{(N+1)}, \tag{2.12}$$

where the matrix $\mathbf{M}$ describes the response of the whole structure to EM fields.

2.4.1 Eigenmodes in isotropic layers

The Yeh formalism can also be used for isotropic media. The solutions for the anisotropic media will not work because the permittivity tensor is diagonal $\varepsilon_{ii} = N^2$, which means that the eigenvector components (2.7) will be zero. The isotropic eigenmodes are not defined and can be chosen arbitrarily, e.g., linearly polarized. The wave vector has two possible orientations [6]

$$\boldsymbol{k}_{\pm} = \frac{\omega}{c} \left(N_{\mathrm{y}} \boldsymbol{e}_{\mathrm{y}} \pm Q^{(n)} \boldsymbol{e}_{\mathrm{z}}\right),$$

with the requirement $N_{\mathrm{y}} = \text{const}$. The N_{y} is usually calculated for the isotropic half-space (air) in which the sample is placed, which implies $N_{\mathrm{y}} = \sin\varphi$, where φ is the angle of incidence. The parameter $Q^{(n)}$ is the z-component of the reduced wave vector in the isotropic layer

$$Q^{(n)} = \sqrt{\varepsilon_{\mathrm{xx}}^{(n)} - N_{\mathrm{y}}^2}.$$

For the dielectric-absorptive media interface, the complex part of the refractive index is fully included in the parameter $Q^{(n)}$. This means that the attenuation of the wave only happens along the z-direction.

The $N_{\mathrm{z}}^{(n)}$ eigenvalues and corresponding eigenvectors are listed in the following table.

$N_{z1}^{(n)} = Q^{(n)}$	$N_{z2}^{(n)} = -Q^{(n)}$	$N_{z3}^{(n)} = Q^{(n)}$	$N_{z4}^{(n)} = -Q^{(n)}$
$\boldsymbol{e_1^{(n)}} = \begin{pmatrix} 1 \\ 0 \\ 0 \end{pmatrix}$	$\boldsymbol{e_2^{(n)}} = \begin{pmatrix} 1 \\ 0 \\ 0 \end{pmatrix}$	$\boldsymbol{e_3^{(n)}} = \begin{pmatrix} 0 \\ Q^{(n)}/N^{(n)} \\ -N_y^{(n)}/N^{(n)} \end{pmatrix}$	$\boldsymbol{e_4^{(n)}} = \begin{pmatrix} 0 \\ Q^{(n)}/N^{(n)} \\ N_y^{(n)}/N^{(n)} \end{pmatrix}$
$\boldsymbol{b_1^{(n)}} = \begin{pmatrix} 0 \\ Q^{(n)} \\ -N_y^{(n)} \end{pmatrix}$	$\boldsymbol{b_2^{(n)}} = \begin{pmatrix} 0 \\ -Q^{(n)} \\ -N_y^{(n)} \end{pmatrix}$	$\boldsymbol{b_3^{(n)}} = \begin{pmatrix} -N^{(n)} \\ 0 \\ 0 \end{pmatrix}$	$\boldsymbol{b_4^{(n)}} = \begin{pmatrix} N^{(n)} \\ 0 \\ 0 \end{pmatrix}$

The dynamical matrix for an isotropic layer takes the form

$$\mathbf{D} = \begin{pmatrix} 1 & 1 & 0 & 0 \\ Q^{(n)} & -Q^{(n)} & 0 & 0 \\ 0 & & Q^{(n)}/N^{(n)} & Q^{(n)}/N^{(n)} \\ 0 & & -N^{(n)} & N^{(n)} \end{pmatrix}.$$

2.5 Reflection and transmission coefficients

The matrix $\mathbf{M}$ introduced in equation (2.12) describes the optical response of the structure. Consequently, this matrix can be linked to the reflection and transmission Jones matrices (1.13) of the sample.

The eigenmodes $\boldsymbol{e}_1^{(n)}$ and $\boldsymbol{e}_3^{(n)}$ propagate in the positive z-direction while the $\boldsymbol{e}_2^{(n)}$ and $\boldsymbol{e}_4^{(n)}$ propagate in the opposite direction. Suppose that the incident light is in the 0 half-space. Therefore no light is hitting the sample in the $N+1$ half-space and $E_2^{(N+1)} = E_4^{(N+1)} = 0$. The elements of reflection and transmission Jones matrices can be calculated as [9]

$$r_{ss} = r_{21} = \left(\frac{E_{02}^{(0)}}{E_{01}^{(0)}}\right)_{E_{03}^{(0)}=0} = \frac{\mathrm{M}_{21}\mathrm{M}_{33} - \mathrm{M}_{23}\mathrm{M}_{31}}{\mathrm{M}_{11}\mathrm{M}_{33} - \mathrm{M}_{13}\mathrm{M}_{31}},$$

$$r_{ps} = r_{41} = \left(\frac{E_{04}^{(0)}}{E_{01}^{(0)}}\right)_{E_{03}^{(0)}=0} = \frac{\mathrm{M}_{41}\mathrm{M}_{33} - \mathrm{M}_{43}\mathrm{M}_{31}}{\mathrm{M}_{11}\mathrm{M}_{33} - \mathrm{M}_{13}\mathrm{M}_{31}},$$

$$r_{pp} = r_{43} = \left(\frac{E_{04}^{(0)}}{E_{03}^{(0)}}\right)_{E_{01}^{(0)}=0} = \frac{\mathrm{M}_{11}\mathrm{M}_{43} - \mathrm{M}_{41}\mathrm{M}_{13}}{\mathrm{M}_{11}\mathrm{M}_{33} - \mathrm{M}_{13}\mathrm{M}_{31}},$$

$$r_{sp} = r_{23} = \left(\frac{E_{02}^{(0)}}{E_{03}^{(0)}}\right)_{E_{01}^{(0)}=0} = \frac{\mathrm{M}_{11}\mathrm{M}_{23} - \mathrm{M}_{21}\mathrm{M}_{13}}{\mathrm{M}_{11}\mathrm{M}_{33} - \mathrm{M}_{13}\mathrm{M}_{31}},$$

and

$$t_{ss} = t_{11} = \left(\frac{E_{01}^{(N+1)}}{E_{01}^{(0)}}\right)_{E_{03}^{(0)}=0} = \frac{\mathrm{M}_{33}}{\mathrm{M}_{11}\mathrm{M}_{33} - \mathrm{M}_{13}\mathrm{M}_{31}},$$

$$t_{ps} = t_{31} = \left(\frac{E_{03}^{(N+1)}}{E_{01}^{(0)}}\right)_{E_{03}^{(0)}=0} = \frac{-\mathrm{M}_{31}}{\mathrm{M}_{11}\mathrm{M}_{33} - \mathrm{M}_{13}\mathrm{M}_{31}},$$

$$t_{pp} = t_{33} = \left(\frac{E_{03}^{(N+1)}}{E_{03}^{(0)}}\right)_{E_{01}^{(0)}=0} = \frac{\mathrm{M}_{11}}{\mathrm{M}_{11}\mathrm{M}_{33} - \mathrm{M}_{13}\mathrm{M}_{31}},$$

$$t_{sp} = t_{13} = \left(\frac{E_{01}^{(N+1)}}{E_{03}^{(0)}}\right)_{E_{01}^{(0)}=0} = \frac{-\mathrm{M}_{13}}{\mathrm{M}_{11}\mathrm{M}_{33} - \mathrm{M}_{13}\mathrm{M}_{31}}.$$

2.6 Microscopic origin of optical and magneto-optical response

2.6.1 Lorentz model

The Lorentz model is a simple classical model that describes an electron response in dielectrics to the external electric field. This phenomenological model is simple in nature, but it is generally sufficient and widely used for modelling the spectral dependence of the diagonal permittivity elements. The electron is elastically bound to an atomic core and behaves like a harmonic oscillator. The equation of motion has the form

$$m\ddot{\boldsymbol{r}} = q\boldsymbol{E} - m\gamma\dot{\boldsymbol{r}} - k_\mathrm{e}\boldsymbol{r},$$

where $q\boldsymbol{E}$ is the driving force, γ damping constant, k_e elastic force, q is the charge of the electron, m its mass and $\boldsymbol{r}$ its position. For time-harmonic driving field $\boldsymbol{E}$ of the incident EM wave, the solution is

$$\boldsymbol{r} = \frac{q}{m}\frac{\boldsymbol{E}_0\,\mathrm{e}^{-\mathrm{i}(\omega t-\boldsymbol{k}\cdot\boldsymbol{r})}}{\omega_0^2 - i\gamma\omega - \omega^2},$$

where $\omega_0 = \sqrt{k_\mathrm{e}/m}$ is the resonant frequency of the electron.

The electric field induces polarization in the medium. In linear isotropic materials, polarization is proportional to the electric field

$$\boldsymbol{P} = \varepsilon_0\chi_\mathrm{e}\boldsymbol{E}, \tag{2.13}$$

where χ_e is electric susceptibility. The polarization is created by the response of N oscillators to the electric field

$$\boldsymbol{P} = Nq\boldsymbol{r}. \tag{2.14}$$

With equations (2.13), (2.14) and the first equation in (1.2), a relation between electron response and relative permittivity ε_r can be derived

$$\tilde{\varepsilon}_\mathrm{r} = 1 + \tilde{\chi}_\mathrm{e} = 1 + \frac{\omega_\mathrm{p}^2}{\omega_0^2 - \mathrm{i}\gamma\omega - \omega^2}, \tag{2.15}$$

where

$$\omega_\mathrm{p} = \sqrt{\frac{Nq^2}{\varepsilon_0 m}} \tag{2.16}$$

is the *plasma frequency*. Typical spectral dependence of the diagonal permittivity tensor element according to the Lorentz model is shown in Fig. 2.4.

2.6.2 Tauc- and Cody-Lorentz models

The Tauc-Lorentz and Cody-Lorentz model the absorption by the Lorentz line shape but additionally model zero absorption under a band gap [13], [14]. The imaginary part of the Tauc-Lorentz oscillator has the form

$$\varepsilon_2 = \begin{cases} \frac{1}{E}\frac{AE_0\gamma(E-E_\mathrm{g})^2}{\left(E^2-E_0^2\right)^2+\gamma^2E^2}, & \text{for } E > E_\mathrm{g}, \\ 0, & \text{for } E \le E_\mathrm{g}, \end{cases}$$

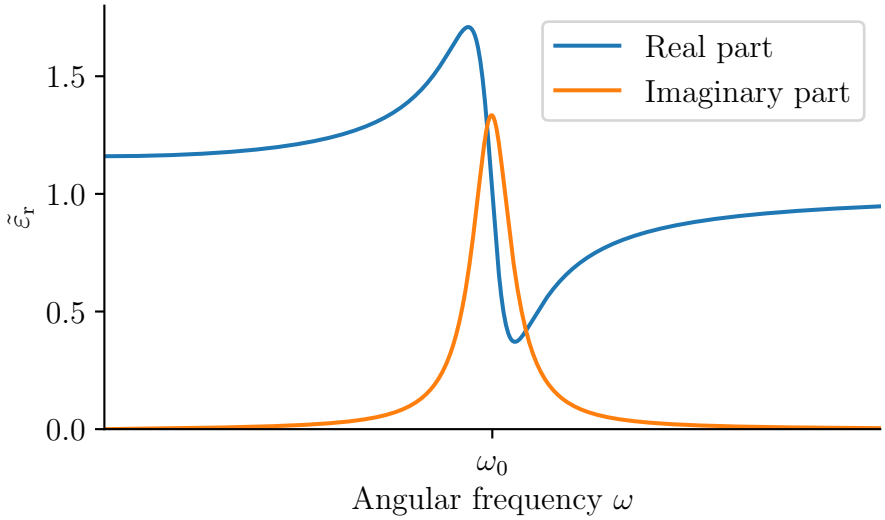

Figure 2.4: Spectral dependence of the diagonal permittivity tensor element near resonance according to the Lorentz model.

where A is the amplitude, E_0 the central energy of the peak, E_g the band gap energy and γ is the broadening.

The Cody-Lorentz oscillator additionally models the absorption under the band gap by the Urbach exponential tail. At the onset of the absorption just above the band gap, the imaginary part or the permittivity is proportional to $(E - E_g)^2$. The Cody-Lorentz model defines two additional transition energies: E_t, where the Urbach tail transitions to the absorption onset behaviour and E_p, where the absorption onset behaviour transitions to Lorentzian behaviour.

2.6.3 Drude model

The Drude model is a special case of the Lorentz model that describes the behaviour of free electrons in a metal. The elastic binding force is equal to zero. The relation (2.15) becomes

$$\tilde{\varepsilon}_r = 1 + \tilde{\chi}_e = 1 - \frac{\omega_p^2}{i\gamma\omega + \omega^2}.$$

The behaviour of metals is dictated by the plasma frequency (2.16) (see Fig. 2.5). Below ω_p, the real part of the refractive index is negligible while the imaginary part is large. This causes the incident light wave to drop exponentially inside the metal, and most of the light is reflected. Above the plasma frequency, the absorption is very low and the metal is transparent.

2.6.4 Magneto-optical transitions

The solution to the wave equation in anisotropic media (2.10) and the eigenmodes suggest that the off-diagonal elements arise because the material interacts differently with the LCP and RCP. The origin of this effect can be described by semiclassical microscopic theory. The different interaction of the circular polarizations results from the splitting of the energy levels by spin-orbit coupling. The

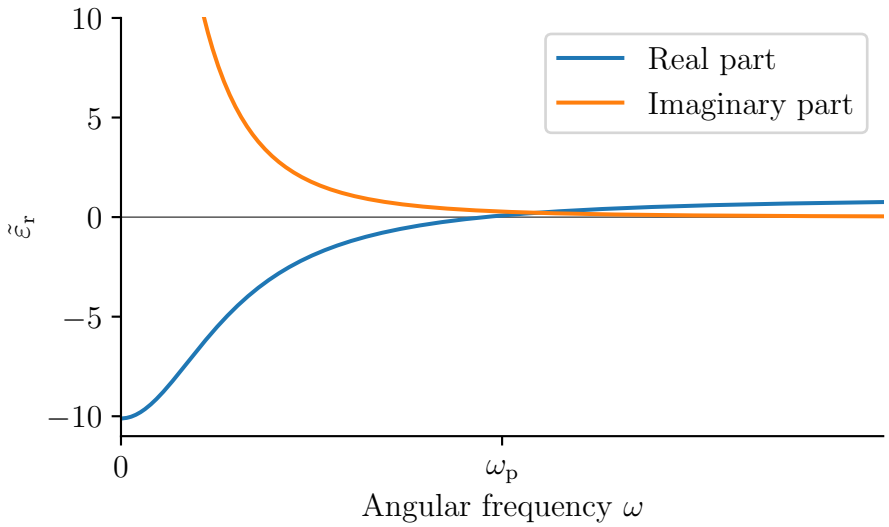

Figure 2.5: Spectral dependence of the diagonal permittivity tensor element according to the Drude model.

circular polarization carries angular momentum $L = 1$ with projections $m_L = \pm 1$. When the circularly polarized photon excites an electron, the electronic transition must conserve the angular momentum, i.e. the angular momentum projection of the electron must change by $\Delta m_L = \pm 1$. When the spin-orbit coupling is absent, the levels are degenerate, and there is no difference for circular polarizations. The effect of an external magnetic field is negligible, and the MO effects mainly come from net spin alignment (magnetization) [15].

There are two types of MO transitions that contribute to the off-diagonal permittivity (Fig. 2.6, Fig. 2.7).

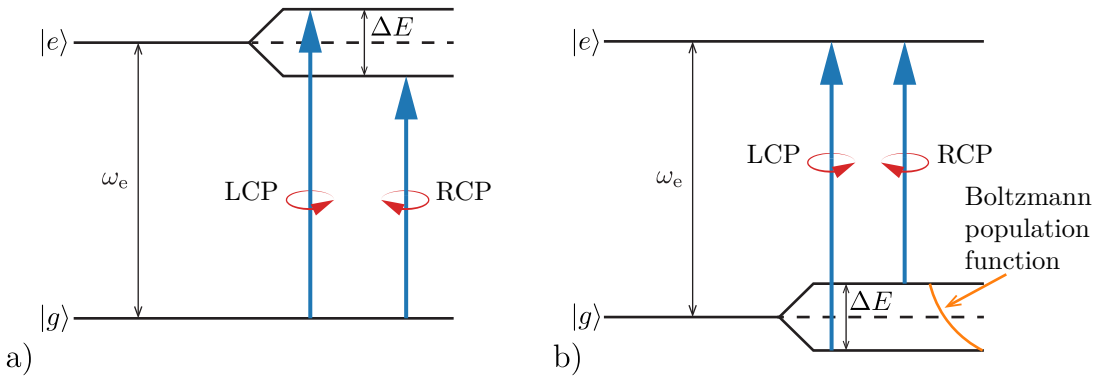

Figure 2.6: Splitting of energy levels for a) type I and b) type II transitions.

Type I, referenced as *double transition* (historically known as *diamagnetic*), originates in excited state splitting. Diamagnetic transitions include, among others, charge transfer transitions [16]. The magnitude of the energy splitting of the excited state is [17]

$$\Delta E = 2\hbar\Delta\omega_e = 2\hbar\left(\omega_{e+} - \omega_{e-}\right),$$

where $\omega_{e\pm}$ are the resonant frequencies for RCP and LCP light. The oscillator

strengths for right and left circular polarizations are equal and expressed as

$$f_{\pm \mathrm{e}(\nu)} = \frac{m\omega_{\mathrm{e}(\nu)}}{\hbar} \left| \langle g | \, x \pm \mathrm{i}y \, | e(\nu) \rangle \right|^2 ,$$

where ν indexes split excited levels and $\omega_{\mathrm{e}(\nu)} = \frac{1}{2}\left(\omega_{\mathrm{e}+} + \omega_{\mathrm{e}-}\right)$.

Assuming $\Delta\omega_{\mathrm{e}} \ll \Gamma_{\mathrm{e}}$, where Γ_{e} is the linewidth, the spectral line shape has the form [18]

$$\varepsilon_2 = -\Gamma_{\mathrm{e}}^2 \left(\varepsilon_2'\right)_{max} \frac{\left(\omega - \omega_{\mathrm{e}}\right)^2 - \Gamma_{\mathrm{e}}^2 + 2\mathrm{i}\Gamma_{\mathrm{e}}\left(\omega - \omega_{\mathrm{e}}\right)}{\left[\left(\omega - \omega_{\mathrm{e}}\right)^2 + \Gamma_{\mathrm{e}}^2\right]^2}.$$

In type II, referenced as *single transition* (historically known as *paramagnetic*), spin-orbit coupling induces a difference in oscillator strengths. This is caused by different Boltzmann occupancy of split ground levels. This transition is therefore strongly dependent on temperature. For example, electric-dipole-forbidden crystal-field transitions of Fe^{3+} ions in O^{2-} complexes belong to this type. The spectral dependence of ε_2 of this transition is

$$\varepsilon_2 = -2\Gamma_{\mathrm{e}} \left(\varepsilon_2''\right)_{max} \frac{\omega\left(\omega^2 - \omega_{\mathrm{e}}^2 + \Gamma_{\mathrm{e}}^2\right) - \mathrm{i}\Gamma_{\mathrm{e}}\left(\omega^2 + \omega_{\mathrm{e}}^2 - \Gamma_{\mathrm{e}}^2\right)}{\left(\omega^2 - \omega_{\mathrm{e}}^2 - \Gamma_{\mathrm{e}}^2\right)^2 + 4\Gamma_{\mathrm{e}}^2}.$$

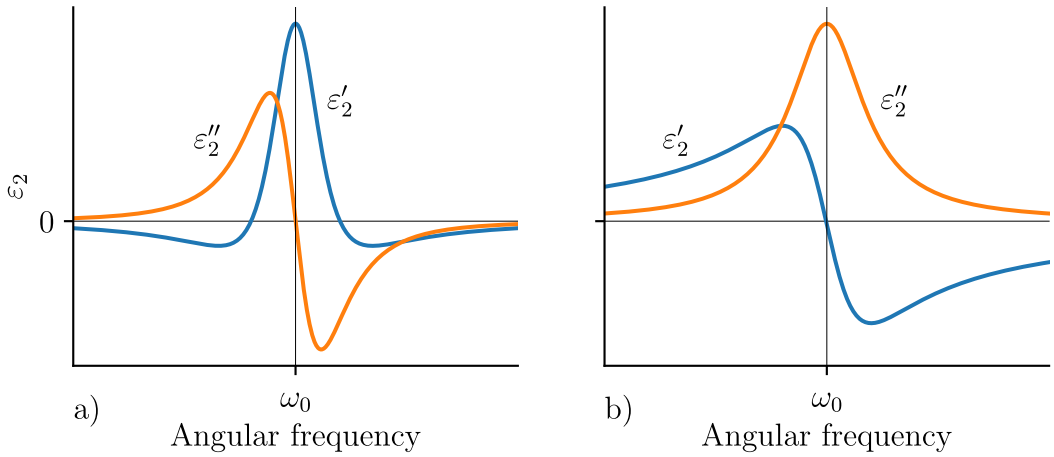

Figure 2.7: Two types of line shapes contributing to the off-diagonal permittivity: a) type I (diamagnetic), b) type II (paramagnetic).

2.6.5 Kramers-Krönig relations

The microscopic models demonstrate that the dielectric permittivity is a function of frequency. Their real and imaginary parts are interrelated through so-called *Kramers-Krönig relations*.

They are a consequence of the fact that the medium cannot respond to impulse before it is applied, i.e. the response function $\chi_{\mathrm{e}}(t)$ is zero for $t < 0$, and the response is not infinitely fast. This, in turn, causes the Fourier transform $\chi_{\mathrm{e}}(\omega)$ to be analytical over the entire complex upper half-plane. Then, through complex

analysis, at following equations that relate the real and imaginary parts can be arrived [19]:

$$\mathrm{Re}(\tilde{\chi}(\omega)) = \frac{1}{\pi} \int_{-\infty}^{\infty} \frac{\mathrm{Im}(\tilde{\chi}(\omega'))}{\omega' - \omega} d\omega',$$

$$\mathrm{Im}(\tilde{\chi}(\omega)) = -\frac{1}{\pi} \int_{-\infty}^{\infty} \frac{\mathrm{Re}(\tilde{\chi}(\omega'))}{\omega' - \omega} d\omega'.$$

These equations, e.g., allow to calculate the refractive index from the absorption coefficient obtained by simple measurement. They, however, apply to many other complex quantities such as Kerr rotation and ellipticity, etc. presented in this thesis.

3. Magnetism

Every substance, to some degree, responds to a magnetic field. According to their response, the materials can be divided into five groups. These groups will be briefly presented in the following sections.

It is worthy of remark that magnetism is a purely quantum phenomenon, and classical physics cannot describe it. Because the magnetic force on an electron is perpendicular to its motion

$$F = -e(\boldsymbol{v} \times \boldsymbol{B}),$$

then no work is done by the magnetic field and the electron's energy is not modified. Therefore no change in magnetization can occur. The Bohr-van Leeuwen theorem presents a more rigorous proof (which can be found, e.g., in [20]). Despite this, QM treatment is not necessary, and many properties of magnetic substances can be described using classical physics with some additional concepts.

3.1 Diamagnetism

Diamagnetism is a property of every material. However, it is so small that any other magnetic contribution will dominate, if present. Therefore, diamagnetism is only observable in substances whose atoms do not have a net magnetic moment, i.e. the atoms have completely filled shells. According to Lenz's law, an induced magnetization opposes an external magnetic field. Also, for example, organic molecules with delocalized electrons have large diamagnetic susceptibilities. The electrons can form large current loops creating magnetic dipoles that oppose the external field. The magnetic susceptibility is virtually independent of temperature, magnetic field, is negative and on the order of 10^{-5} [21]. This type of materials will not be studied in this thesis.

3.2 Paramagnetism

Paramagnetism manifests in materials whose atoms have a net magnetic moment. The magnetic moment comes from the intrinsic spin of an electron and its orbital motion around an atomic core. These materials have a small positive magnetic susceptibility on the order of 10^{-4}, and the induced magnetization is aligned with an external field. Upon removal of the external magnetic field, the magnetization disappears. There are multiple theories describing paramagnetism in various materials. Langevin theory, for example, describes noninteracting localized electrons. The magnetic moments will be randomly oriented without an external magnetic field due to thermal excitations. The temperature dependence of the susceptibility is known as Curie's law

$$\chi_{\mathrm{m}} = \frac{C}{T},$$

where C is the Curie constant dependent on the material.

Another theory, Pauli paramagnetism, describes paramagnetism due to the free electron gas in metals. The magnetic field shifts two subbands of electron spins, increasing the density of electrons with spin antiparallel to the magnetic field resulting in a net magnetic moment.

3.3 Exchange interaction

The three remaining groups of materials exhibit spontaneous magnetic order. The so-called *exchange interaction* enables the individual magnetic moments of atoms to align at long distances. This interaction is a Coulomb repulsion acting with the Pauli principle, which states that two electrons cannot be in the same quantum state.

Consider two electrons with wavefunctions ψ_a and ψ_b with coordinates $\boldsymbol{r}_1$, $\boldsymbol{r}_2$. The total wavefunction, a product of spin wavefunction and spatial wavefunction, must be antisymmetric. The two possibilities are the product of spatial antisymmetric with spin symmetric part χ_T (*triplet state*, $S = 1$) or spatial symmetric with spin antisymmetric part χ_S (*singlet state*, $S = 0$). The wavefunctions for the singlet state ψ_S and triplet state ψ_T can be written as [22]

$$\psi_\mathrm{S} = \frac{1}{\sqrt{2}} \left(\psi_\mathrm{a}(\boldsymbol{r}_1)\psi_\mathrm{b}(\boldsymbol{r}_2) + \psi_\mathrm{a}(\boldsymbol{r}_2)\psi_\mathrm{b}(\boldsymbol{r}_1)\right) \chi_\mathrm{S},$$
$$\psi_\mathrm{T} = \frac{1}{\sqrt{2}} \left(\psi_\mathrm{a}(\boldsymbol{r}_1)\psi_\mathrm{b}(\boldsymbol{r}_2) - \psi_\mathrm{a}(\boldsymbol{r}_2)\psi_\mathrm{b}(\boldsymbol{r}_1)\right) \chi_\mathrm{T}.$$

The energies of the states are

$$E_\mathrm{S} = \int \psi_\mathrm{S}^* \hat{H} \psi_\mathrm{S} \mathrm{d}\boldsymbol{r}_1 \mathrm{d}\boldsymbol{r}_2,$$
$$E_\mathrm{T} = \int \psi_\mathrm{T}^* \hat{H} \psi_\mathrm{T} \mathrm{d}\boldsymbol{r}_1 \mathrm{d}\boldsymbol{r}_2.$$

The *exchange integral* is defined as

$$J = \frac{E_\mathrm{S} - E_\mathrm{T}}{2} = \int \psi_\mathrm{a}^*(\boldsymbol{r}_1)\psi_\mathrm{b}^*(\boldsymbol{r}_2)\hat{H}\psi_\mathrm{a}(\boldsymbol{r}_2)\psi_\mathrm{b}(\boldsymbol{r}_1)\mathrm{d}\boldsymbol{r}_1\mathrm{d}\boldsymbol{r}_2.$$

The exchange integral is included in the Heisenberg Hamiltonian, describing the interaction of two neighbouring spins

$$\hat{H}_\mathrm{ex} = -2J\boldsymbol{S}_1 \cdot \boldsymbol{S}_2,$$

which can be generalized to a sum over all neighbouring atoms

$$\hat{H}_\mathrm{ex} = -2\sum_{i<j} J_{ij}\boldsymbol{S}_i \cdot \boldsymbol{S}_j,$$

where $\boldsymbol{S}_i$ and $\boldsymbol{S}_j$ are spin operators. The sign of J determines the magnetic order, i.e. $J > 0$ indicates a *ferromagnetic* order with neighbouring spins parallel while $J < 0$ indicates *antiferromagnetic* order with antiparallel spins (Fig. 3.1).

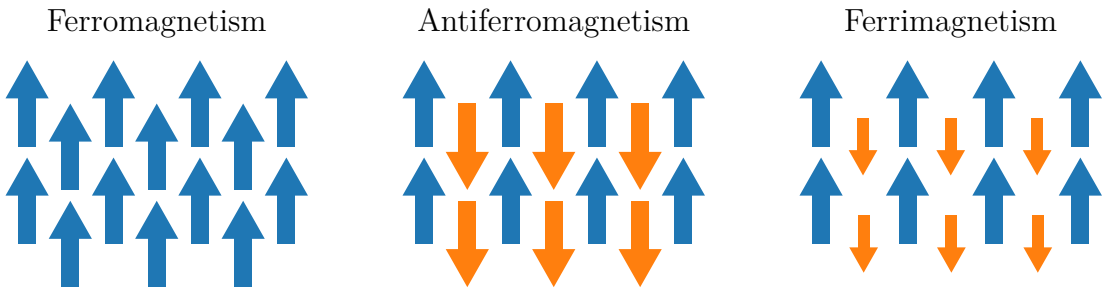

Figure 3.1: Schematic illustration of various magnetically ordered materials.

3.4 Ferromagnetism

As was stated in the previous section, ferromagnetic substances display spontaneous magnetic order and, therefore, nonzero macroscopic magnetization in the absence of an external magnetic field. The magnetic moments of neighbouring atoms are aligned parallel via the exchange interaction. Magnetic order is retained up to the *Curie temperature* T_{C}, after which the thermal excitations overcome the ordering, and the material becomes paramagnetic. Typical temperature dependence of the magnetization M is shown in Fig. 3.2.

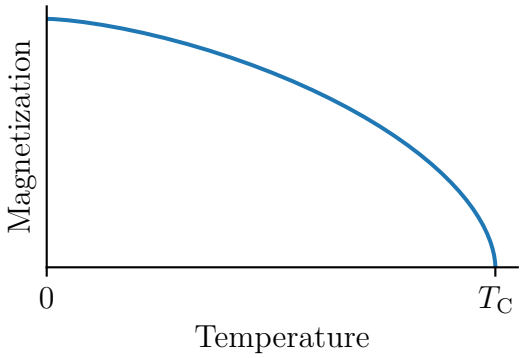

Figure 3.2: Typical temperature dependence of the magnetization of a ferromagnet.

The magnetization value of the magnetically ordered materials depends on the history of an applied external magnetic field. This property is called *hysteresis* (Fig. 3.3). The magnetic material can break up into magnetic domains with different magnetic moment alignment, and the resulting magnetization will be zero. The applied magnetic field starts to reorient the magnetic domains parallel with the field up to the *saturation point* M_{sat}, where all the domains are aligned. After switching off the magnetic field, the magnetization remains at the *remanence value* M_{r}. Increasing the magnetic field into the negative values begins to reorient the magnetic domains, and at the *coercive field* H_{c}, the magnetization is equal to zero. Further increasing the negative magnetic field, the material saturates, and the hysteresis loop can be reproduced again. In some materials the change in the direction of the magnetization can be more sudden, caused by the coherent rotation of the individual magnetic moments parallel to the external field.

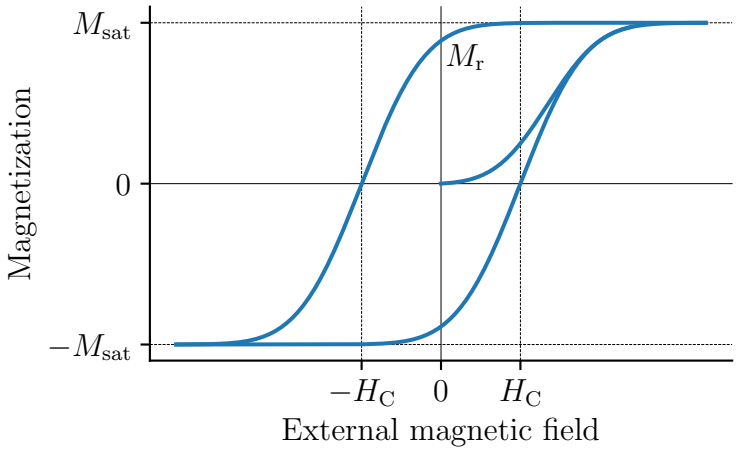

Figure 3.3: Hysteresis loop of a ferromagnet.

3.5 Antiferromagnetism

Negative exchange integral results in the antiparallel ordering of neighbouring spins. The material can be thought of as composed of two magnetic sublattices with equal opposite magnetic moments. An antiferromagnet has no net magnetic moment, and consequently, only weakly interacts with an external magnetic field, which is an attractive property, e.g., for magnetic memories [23], [24]. The temperature above which the antiferromagnet becomes paramagnetic is called *Néel temperature* T_{N}. More complicated antiferromagnetic materials can be composed of more than two noncollinear sublattices.

3.6 Ferrimagnetism

A ferrimagnetic material has two or more magnetic sublattices oriented antiparallel, similar to an antiferromagnet. Nonetheless, the sublattices have unequal magnetic moments, resulting in a nonzero total magnetic moment. The material thus behaves as a ferromagnet and similarly has a Curie temperature T_{C}. The temperature dependence of magnetization of ferrimagnets can be such that the total magnetic moment disappears at the *compensation temperature* T_{Comp} (Fig. 3.4). That is caused by the different temperature dependence of the opposite magnetic moments in different sublattices. Below T_{Comp}, one sublattice dominates and is aligned with an external magnetic field. Above T_{Comp}, the situation reverses, and the second sublattice is parallel to the magnetic field. A temperature change can therefore achieve a reversal of the magnetization. A combination of ferro- and antiferromagnetic properties renders these materials an attractive candidate in the field of spintronics [25], [26].

3.7 Magnetic anisotropy

The magnetization of a material points in a particular preferred direction called the *easy axis*. Along this axis, the material magnetizes the easiest, and after switching off the magnetic field, the magnetization remains at remanence

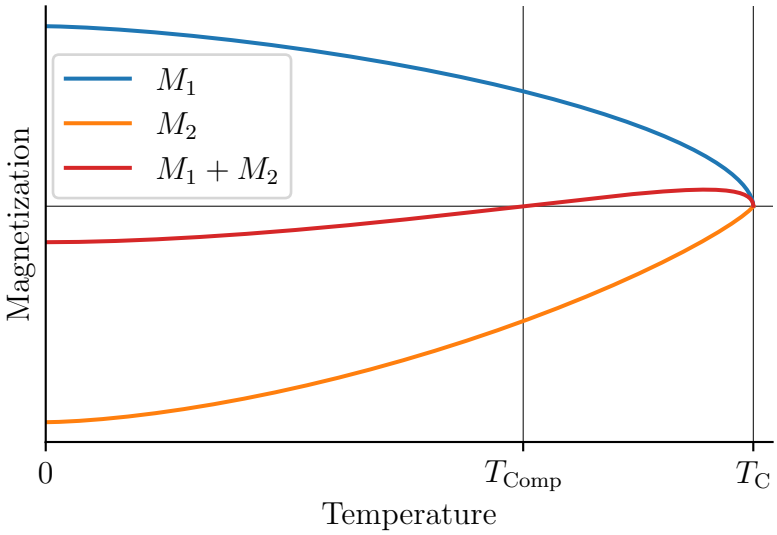

Figure 3.4: Temperature dependence of magnetization of a ferrimagnet with two sublattice magnetizations M_1 and M_2.

value M_{r}.

For uniaxial crystals, the easy direction is determined by the minimum of anisotropy energy density

$$E_{\mathrm{a}} = K_1 \sin^2 \theta,$$

where K_1 is the anisotropy constant, and θ is the angle between the anisotropy axis and magnetization.

There are three main contributions to the anisotropy constant K_1 [21]:

- *shape anisotropy*, which depends on the shape of the sample and generally lies in the plane of a thin layer sample,
- intrinsic *magnetocrystalline anisotropy*, which depends on spin-orbit interactions of the electrons and crystallographic symmetry and aligns magnetization to one of the crystallographic axes,
- *induced anisotropy*, which can be, e.g., induced by annealing the material in a magnetic field or by uniaxial stress.

The stress-induced anisotropy constant K_{i} is expressed as

$$K_{\mathrm{i}} = \frac{3}{2} \lambda_{\mathrm{s}} \sigma_{\parallel},$$

where λ_{s} is the magnetostriction constant, and $\sigma_{\parallel}$ is in-plane stress. If the in-plane stress is produced by lattice mismatch between substrate and thin layer, it can be expressed as [27]

$$\sigma_{\parallel} = \frac{E}{1-\nu} \frac{d_{\mathrm{sub}} - d_{\mathrm{layer}}}{d_{\mathrm{layer}}},$$

where E is Young's modulus, ν Poisson's ratio, d_{sub} and d_{layer} are substrate and layer crystal plane spacings. This anisotropy usually forces the easy axis perpendicular to the sample plane. For spintronic applications, it is favourable to

achieve out of plane magnetization, commonly termed *perpendicular magnetic anisotropy* (PMA), to utilize mechanisms, such as spin-orbit torques, Rashba-Edelstein effect, to manipulate the magnetic moment of the material. [28]

Perpendicular to the easy axis lies the *hard axis*. Magnetizing the material along this axis costs energy, and the moments are less prone to orient parallel to the field. The remanence value M_r in this direction is generally minimal. The field value at which the value M_{sat} is reached for this direction is called the *anisotropy field*. Different behaviour of magnetization along the easy and hard axis is shown in Fig. 3.5.

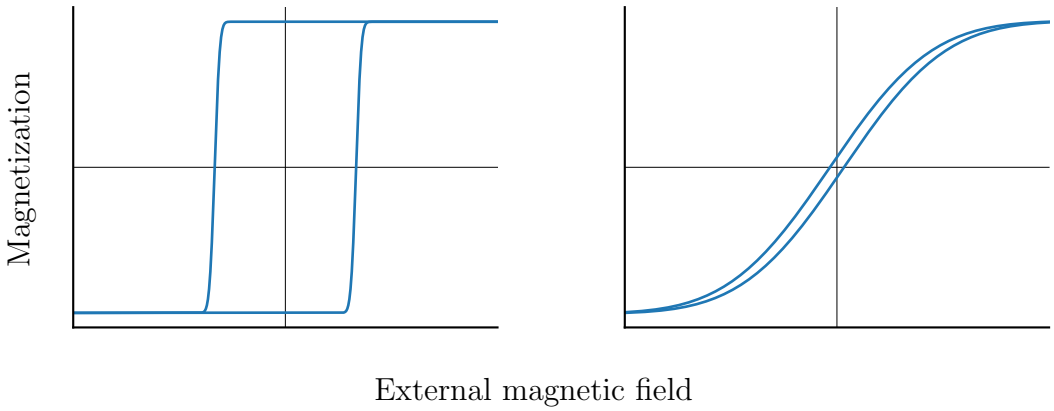

Figure 3.5: Hysteresis loop along the easy (left), and hard (right) axis.

Hysteresis loops are also present in MO effects. Because of the antiparallel alignment of sublattices, ferrimagnets can display anomalous hysteresis loops under certain circumstances. Each sublattice can have its coercive field and saturation magnetization. Suppose two magneto-optical transitions come from different sublattices and overlap in a spectrum with opposite signs. In that case, they can produce an anomalous hysteresis loop, visible in MOKE or Faraday effect (Fig. 3.6). Exploiting this anomaly, the contributions of the sublattices to the magneto-optical spectrum can be resolved and separated.

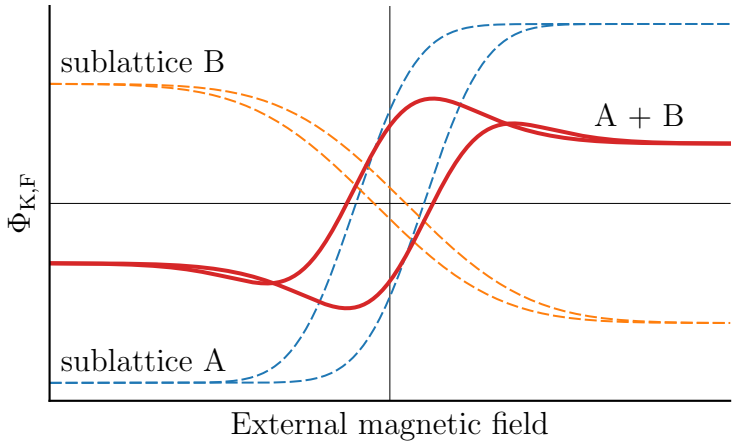

Figure 3.6: Anomalous ferrimagnetic hysteresis loop visible in MOKE or Faraday effect.

4. Experimental techniques

4.1 Spectroscopic ellipsometry

Spectroscopic ellipsometry (SE) is a method that exploits the change in light polarization upon reflection or transmission to study optical properties of surfaces, thin layers, multilayers but also bulk samples. It is often employed to acquire the extinction coefficient, refractive index and thickness of a layer. Because of its high sensitivity, ellipsometry can also be used for in-situ measuring of the growth of thin layers down to atomic thicknesses. The high sensitivity stems from measuring the relative change between Fresnel coefficients. This ratio is expressed as

$$\rho = \frac{r^{\mathrm{p}}}{r^{\mathrm{s}}} = \tan\Psi \mathrm{e}^{\mathrm{i}\Delta}, \tag{4.1}$$

where Ψ and Δ are the *ellipsometric angles*, which describe the amplitude and phase change after reflection.

If a bulk sample with no surface roughness is measured, and therefore the polarization change comes from a single interface, the optical constants of the material can be immediately calculated by inversing relation (4.1), which yields the relation for relative permittivity

$$\varepsilon_1 = \sin^2\phi \left(1 + \tan^2\phi \left(\frac{1-\rho}{1+\rho}\right)^2\right),$$

where ϕ is the angle of incidence. For a sample consisting of multiple layers, a representative model has to be built with known parameters, and unknown parameters are determined through a fitting procedure.

Ellipsometric data in this thesis were collected on commercially available ellipsometer Woollam RC2. This spectroscopic ellipsometer employs two continuously rotating compensators (Fig. 4.1). The two compensators rotate at a constant frequency and a fixed ratio. This method allows measurement of all elements of the Müller matrix and is therefore suitable for measuring anisotropic, depolarizing or optically active samples. The Fourier analysis is needed to recover the elements of the Müller matrix, or the ratio ρ. The rotating compensators method is described in more detail, e.g., in [29].

The ellipsometer comes with the computer program `CompleteEASE` for data analysis. The purpose of the analysis is to obtain unknown layer parameters, be it optical constants or thickness or both. This is done by a model-based fitting procedure. During the analysis, a model representing the sample structure is built. The layers are represented by their thicknesses and optical constants. If the model structure accurately represents the real sample, the simulated SE data will match the measured data. Known optical constants are inserted into the model from the program library or previous measurements. Surface roughness is by default modelled by the Brugemann effective medium approximation (EMA), which mixes the underlying layer with assumed 50 % air content. The unknown optical constants can be fit with standard optical models, such as the Cauchy model or the Sellmeier model. More complicated shapes of optical constants are fit by B-spline smooth curves [30], which are fully Kramers-Krönig consistent,

and subsequently by line shapes based on Lorentz and Drude models. CompleteEASE uses the non-linear Levenberg-Marquardt algorithm for minimizing the mean square error (MSE). Besides the MSE, the physicality of the fit parameters is evaluated, and therefore a certain user experience is required.

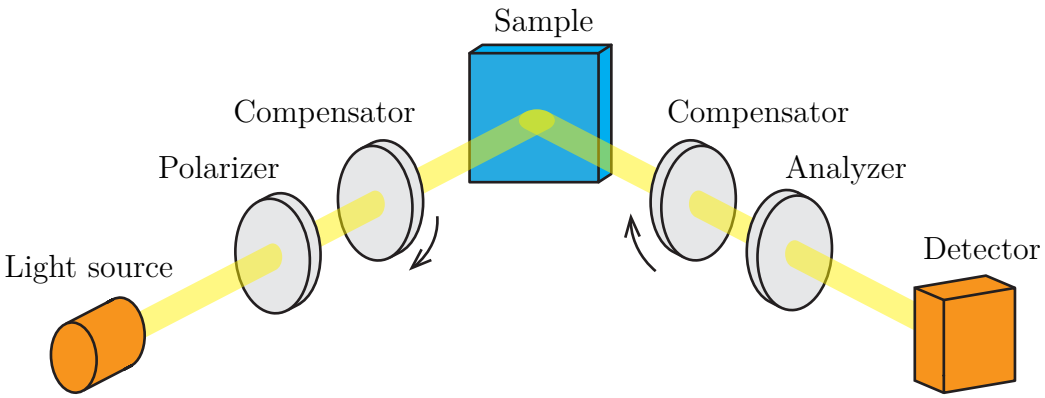

Figure 4.1: Ellipsometer setup with two rotating compensators.

4.2 Magneto-optical spectroscopies

MO spectroscopies measure quantities described in section 1.4. The *rotating analyzer technique* in polar configuration was used for acquiring MO data. The setup consists of a broad spectrum light source, polarizer, waveplate (optional), analyzer and spectrometer (Fig. 4.2).

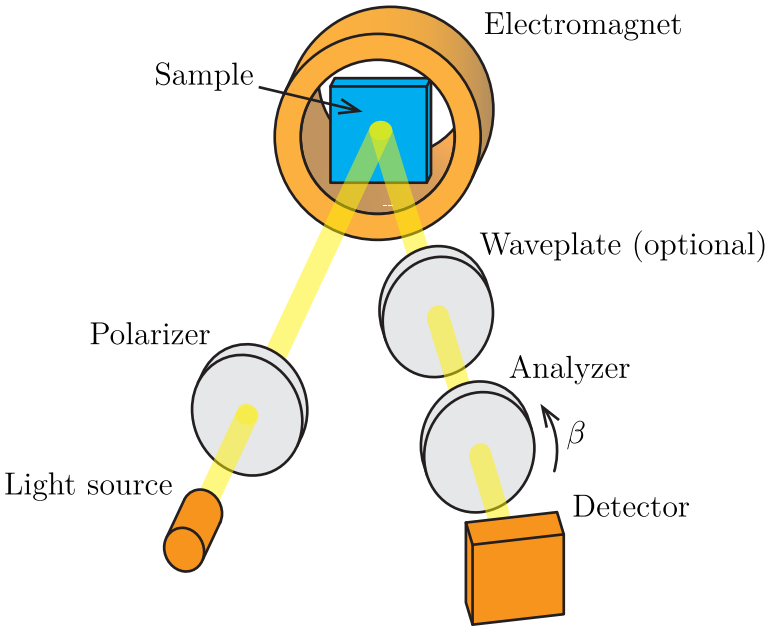

Figure 4.2: Rotating analyzer technique for measuring MOKE spectra. Faraday configuration is similar, with waveplate, analyzer and detector behind the sample.

The technique is based on the older method of nearly crossed polarizers. The optical setup, for example, in reflection configuration, can be described by Jones

formalism as

$$\begin{pmatrix} E_{\mathrm{x}}^{\mathrm{out}} \\ E_{\mathrm{y}}^{\mathrm{out}} \end{pmatrix} = \begin{pmatrix} \cos^2\beta & \sin\beta\cos\beta \\ \sin\beta\cos\beta & \sin^2\beta \end{pmatrix} \begin{pmatrix} 1 & 0 \\ 0 & \mathrm{e}^{\mathrm{i}\delta} \end{pmatrix} \begin{pmatrix} r_{\mathrm{ss}} & r_{\mathrm{sp}} \\ r_{\mathrm{ps}} & r_{\mathrm{pp}} \end{pmatrix} \begin{pmatrix} 0 \\ E_{\mathrm{y}}^{\mathrm{in}} \end{pmatrix},$$

where β is the angle of the analyzer axis and δ is phase retardation. The same equation can be written for transmission measurement. Without loss of generality, for normal incidence, the input polarization has been chosen in the y-direction. Using the definitions of MO angles, the output intensity can be expressed as

$$I^{\mathrm{out}} = I^{\mathrm{in}} R \left(\sin^2\beta + \left|\Phi_{\mathrm{K_p}}\right|^2 \cos^2\beta + \sin(2\beta)\left(\theta\cos\delta - \epsilon\sin\delta\right)\right). \tag{4.2}$$

The second quadratic term can be eliminated because the MO angles are generally small. The first term is the classical Malus law, the intensity between two polarizers with angle β between them. The third term is the contribution from the sample. If the waveplate with retardance δ is left out from the setup, only the rotation θ is measured.

In the real experiment, the output intensity is measured for a number of discrete β values at a fixed magnetic field. It is advantageous to keep the Malus term small for a good signal-to-noise ratio, so the experiment is usually measured for β values from 2 to 5 and -2 to -5 degrees. The β dependence of output intensity is fit with a function based on equation (4.2)

$$I^{\mathrm{out}} = A\sin^2\beta + B\sin(2\beta) + C,$$

and the measured Kerr or Faraday effect is then

$$\Phi_{\mathrm{K,F}} = \frac{B}{A}.$$

This procedure is carried out for every wavelength in the spectrum. However, the total Kerr or Faraday effect can also include contributions, not from the sample. This can be resolved by using the parity of MO effects. Since the linear MO effects are odd in magnetization and other contributions are usually even (constant), the experiment is performed for a positive and negative magnetic field. The pure effect coming from the sample can then be calculated as

$$\Phi_{\mathrm{K,F}}^{\mathrm{sam}} = \frac{\Phi_{\mathrm{K,F}}(B) - \Phi_{\mathrm{K,F}}(-B)}{2}.$$

This method has accuracy down to 1 mdeg, so even very thin layers and small MO effects can be measured. The spectrum is acquired at once with commercial OceanOptics spectrometer with a range of 1.4 eV to 6.2 eV. This allows the measurement to be performed significantly faster than wavelength by wavelength methods and a MO spectrum with reasonable accuracy can be obtained in a matter of minutes.

For MOKE and Faraday measurement, 1 T and 0.62 T electromagnets were used, respectively. The magnetic field can also be swept with the desired step to measure spectral hysteresis loops.

4.3 Pulsed laser deposition

Pulsed laser deposition (PLD) is a versatile technique for the preparation of thin layers. It can prepare high-quality layers of various materials, including metals, insulators, semiconductors, superconductors, and polymers. It is suitable for growing materials with complex stoichiometries such as garnets or perovskites.

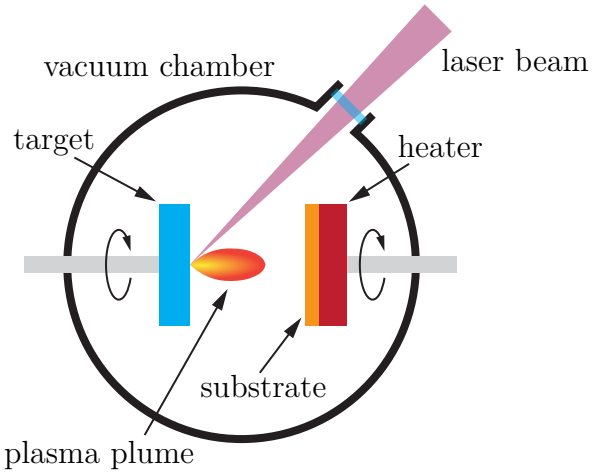

Figure 4.3: The principle of PLD. High-energy laser pulses evaporate the target material creating a plasma plume that deposits on the heated substrate.

The basic principle of PLD is relatively simple (Fig. 4.3). A high-power laser, typically a KrF excimer laser, produces short pulses focused on the target, made out of the desired material. The target material instantaneously vaporizes into ions and neutrals that create a plasma plume. Subsequently, the plasma plume moves with an energy of $\sim$ 1 eV–100 eV towards the heated substrate where it deposits. The substrate is heated to several hundred °C to improve the mobility of the deposited atoms so that they can find the most energetically stable position. The most significant advantage of the PLD is transferring the target stoichiometry to the grown layer. However, during the deposition of volatile elements, the target stoichiometry needs to be adjusted, so the desired composition of the layer is achieved. The substrate and the target continuously rotate for better homogeneity of deposition and ablation.

This method can operate in a range of pressures from $<10^{-7}$ mbar to 1 mbar but needs a lower vacuum than, for example, molecular beam epitaxy (MBE). Some partial gas pressure is required to slow down the plasma, so the substrate or grown layer is not damaged. An oxygen atmosphere is needed to grow oxide layers with good stoichiometry.

Many variables influence the resulting quality of the grown layer, such as laser repetition rate, energy, background gas pressure, substrate temperature, substrate distance from the target and treatment of the layer after the deposition. Therefore they need to be finely tuned.

5. Studied samples

In this thesis, the rare-earth ferrimagnetic garnet thin films are studied. The garnets have one of the most complex crystal structures found in nature. The general characteristics and some properties of this material are briefly described in this chapter.

5.1 Ferrimagnetic garnets

Ferrimagnetic garnets crystalize in a body-centred cubic lattice with 8 formulas $R^{3+}{}_3Fe^{3+}{}_5O^{2-}{}_{12}$ per unit cell, a total of 160 atoms. The oxygen ions define three types of cation sites:

- dodecahedral (c) site, which is occupied by 24 R^{3+} rare-earth ions,
- octahedral (a) site, where 16 Fe^{3+} ions reside,
- tetrahedral (d) site, where the remaining 24 Fe^{3+} are located.

However, the tetrahedral and octahedral sites are not regular polyhedrons but are slightly distorted. The dodecahedral site is an irregular hexahedron obtained by applying torsion to a cube about the body diagonal and then distorting the faces [31].

The cation preference of sites is determined mainly by the ionic radius of the cation. Cation in every site can be substituted with a myriad of elements considering the atomic radius. This allows tailoring of the magnetic and optical properties. The Fe^{3+} ions in the tetrahedral site, for example, can be substituted with Ga^{3+} or Al^{3+} ions to reduce the magnetization. The very large rare-earth ions preferentially occupy the dodecahedral site and can be substituted, e.g., with Nd^{3+} and Bi^{3+}. In garnets, the ratio of dodecahedral ions and Fe^{3+} is denoted by the *composition parameter* R, and for ideal garnets equals 0.6. The ratio varies a bit in real samples and can affect physical their properties. The lattice parameter of iron garnets changes with the ionic radius in the (c) site with the range 12.283 Å–12.529 Å for rare-earth ions. It also, to some degree, depends on other factors, such as the preparation technique, used substrate, stress and strain.

The total saturation magnetization of the iron garnet is

$$M_{\mathrm{sat}} = \left|(M_{\mathrm{d}} - M_{\mathrm{a}}) \pm M_{\mathrm{c}}\right|,$$

where the indices d, a, c label the magnetization of tetrahedral, octahedral and dodecahedral sublattice, respectively. The octahedral and tetrahedral sites with antiparallel magnetic moments contribute with a 2:3 ratio. Therefore the tetrahedral site provides one Fe^{3+} uncompensated magnetic moment with the magnitude of $5\,\mu_{\mathrm{B}}$ at 0 K ($\mu_{\mathrm{B}} = \frac{e\hbar}{2m_{\mathrm{e}}}$, *Bohr magneton*). The magnetic moment of lanthanides, which is the case of this thesis, is determined by the quantum number J, but the antiferromagnetic exchange only aligns the spin antiparallel. For the lower half of the lanthanide series, $J = |L - S|$, and the magnetic moment is aligned parallel and adds to the iron moment. For the upper half, $J = |L + S|$, so the magnetic moment is antiparallel to the Fe^{3+} magnetic moment.

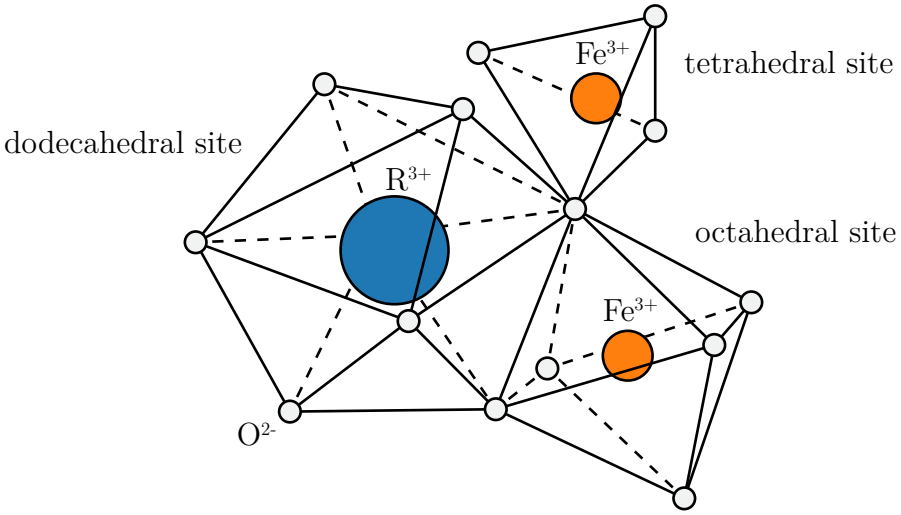

Figure 5.1: One octant of garnet structure, rare-earth ion (blue) in dodecahedral site, iron ions (orange) in tetrahedral and octahedral sites.

The Curie temperature, where the garnet becomes paramagnetic, is in the vicinity of 560 K, only weakly dependent on the rare-earth ion. On the other hand, the compensation temperature varies extremely for each ion. Garnets with rare-earth ions, whose magnetic moment is $< 5\,\mu_B$, have no compensation temperature [21] because the rare-earth magnetic moment is not big enough to cancel out the iron magnetic moment at any temperature.

The most researched representative of ferrimagnetic garnets is yttrium iron garnet (YIG), $Y_3Fe_5O_{12}$. Yttrium is a diamagnetic ion which does not contribute to magnetic or magneto-optical properties, therefore the properties of iron sites or yttrium substituting elements can be studied. The most studied substitution for yttrium is Bi^{3+} which greatly enhances MO effects in the visible region. Garnets have a very complicated MO spectra compared to other structures, such as spinels and perovskites.

Samples studied in this thesis are TbIG and can be divided into two groups: non-doped $Tb_3Fe_5O_{12}$ and $Tb_3Fe_5O_{12}$ doped with Ce^{3+} and Bi^{3+}. These thin layers were deposited either on GGG substrate with crystallographic orientation (111) or crystalline Si substrate. GGG has a lattice constant $a = 12.383$ Å, so the samples grown on GGG are single crystals due to the good lattice match. Samples on Si, with $a = 5.431$ Å, are polycrystalline due to the significant lattice mismatch. All samples were prepared at the Massachusetts Institute of Technology in Boston, USA, by pulsed laser deposition described in the previous chapter. The studied samples are listed in the Tab. 5.1. The exact content of terbium and iron can slightly vary from the nominal values.

Non-doped samples			
Sample name	Sample	Substrate	Nominal thickness [nm]
123TbIG/G	$Tb_3Fe_5O_{12}$	GGG(111)	123
300TbIG/G	$Tb_3Fe_5O_{12}$	GGG(111)	300
123TbIG/S	$Tb_3Fe_5O_{12}$	Si	123
300TbIG/S	$Tb_3Fe_5O_{12}$	Si	300
Doped samples			
Sample name	Sample	Substrate	Nominal thickness [nm]
Ce0.7TbIG/G	$Ce_{0.7}Tb_{2.3}Fe_5O_{12}$	GGG(111)	80–110
Bi0.5TbIG/G	$Bi_{0.5}Tb_{2.5}Fe_5O_{12}$	GGG(111)	-
Bi0.06TbIG/G	$Bi_{0.06}Tb_{2.96}Fe_5O_{12}$	GGG(111)	86
Bi0.01TbIG/S	$Bi_{0.01}Tb_{2.99}Fe_5O_{12}$	Si	-

Table 5.1: Samples studied in this thesis, their composition, type of substrate and nominal thicknesses. The samples will be referenced to with their respective sample name throughout the rest of this thesis.

6. Results and discussion

6.1 Optical properties

Investigated samples were measured on the spectroscopic ellipsometer Woolam RC2 to acquire diagonal permittivity, thicknesses of the layers and surface roughness. Since the area of the samples is small, the ellipsometer light beam diameter was reduced with iris, but lowering the intensity increases measurement error. For most samples, the measurements were done for three angles of incidence, 55°, 60° and 65°. For smaller samples, the angles of incidence were limited to 40°, 45° and 50° to ensure that the light beam spot was not larger than the sample surface. Another option was to use focusing probes supplied with the ellipsometer that reduce the spot diameter from 3 mm–4 mm to 0.3 mm. The probes, however, introduce additional error to the measurement, so for each sample, a measuring method was chosen that resulted in the best model fit.

For the SE analysis, a model representative of the structure was built. The optical constants of the Si substrate were available in the program library. The GGG optical constants were obtained from separate SE measurement of the bare substrate. The optical constants of unknown layers were firstly modelled by B-spline curves and subsequently by a sum of Tauc- and Cody-Lorentz oscillators. Optical constants of the sample 300TbIG/G were fit with a graded layer model consisting of two layers whose optical constants differ by 8 %. This model significantly improved the fit in terms of MSE and is supported by the MOKE measurements. The samples on Si were modelled with thin layer of SiO_2 between the substrate and the TbIG layer, because of the expected oxidation of Si substrate in oxygen background gas during the deposition of the garnet layer. Spectral dependences of SE angles and oscillator fit for one sample (123TbIG/G) are shown in Fig. 6.1 and Fig. 6.2. The fit agrees well with experimental data as follows from Fig. 6.1. The parameters of the oscillator model are listed in Tab. 6.1. The permittivity of the 123TbIG/G sample was modelled solely by Tauc-Lorentz oscillators.

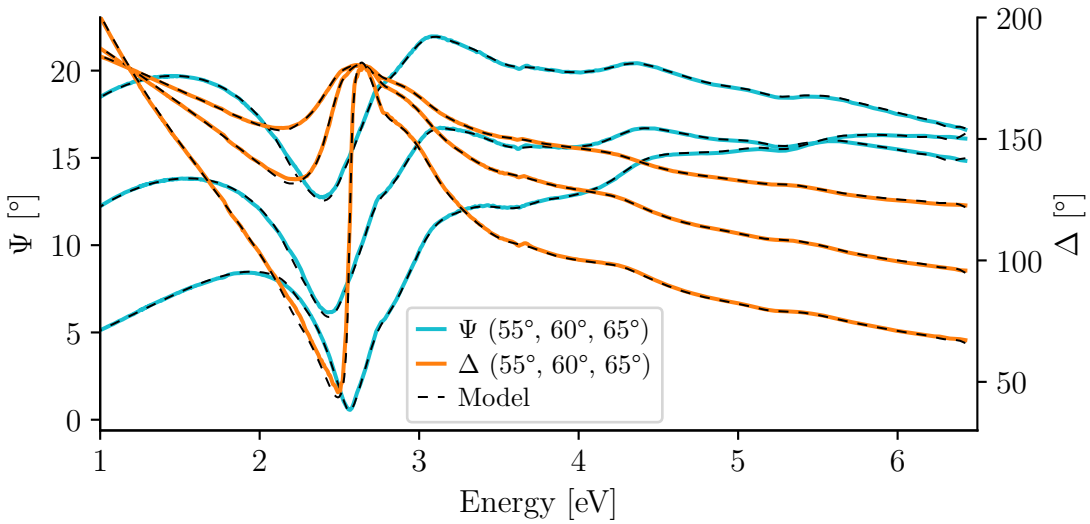

Figure 6.1: SE data and model of the sample 123TbIG/G.

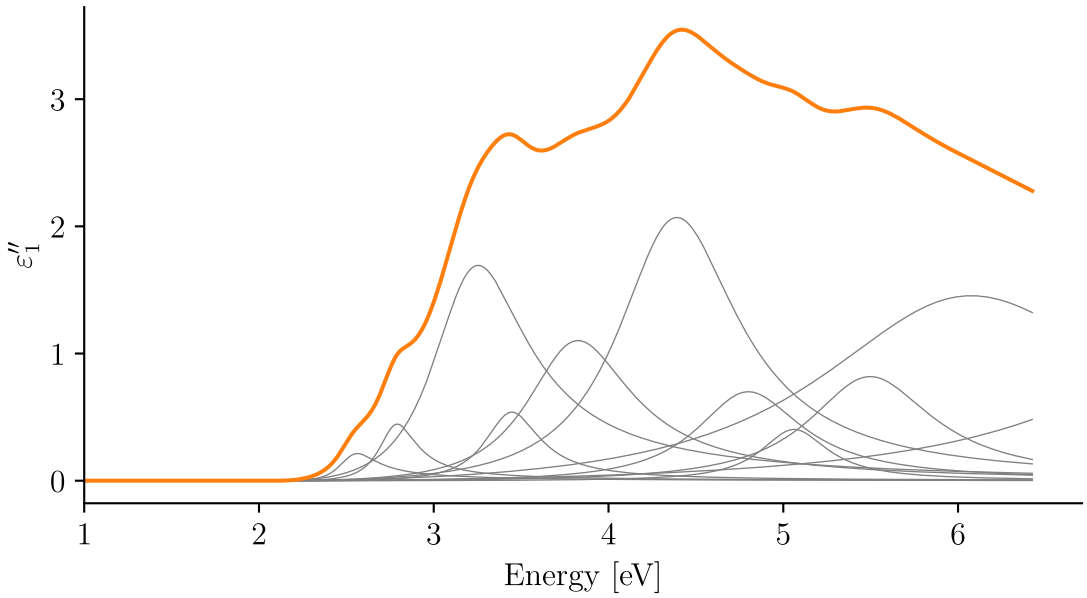

Figure 6.2: Decomposition of the spectral dependence of imaginary part of diagonal element of permittivity tensor into Tauc-Lorentz oscillators for the sample 123TbIG/G.

A [eV]	E_0 [eV]	γ [eV]
1.77	2.53	0.26
2.01	2.77	0.26
9.31	3.20	0.65
1.38	3.43	0.38
4.05	3.79	0.73
6.46	4.37	0.83
1.64	4.79	0.73
0.55	5.05	0.46
1.86	5.49	0.86
7.40	6.06	2.16
5.80	7.85	2.34

Table 6.1: Parameters of the Tauc-Lorentz oscillators used to model the imaginary part of ε_1 spectral dependence of the sample 123TbIG/G. A denotes the amplitude, E_0 central energy of the peak and γ the broadening of the peak. Similar models were used for rest of the samples.

Spectral dependence of the diagonal element of permittivity tensor of non-doped TbIG samples are shown in Fig. 6.3. The amplitude of the permittivity of TbIG across the spectrum slightly varies from sample to sample but the peak positions differ negligibly. Various reasons can cause this. The stoichiometry and structure of the layers can vary for different substrates and thicknesses of deposited layers. The 123 nm samples have $R = 0.57$, while the 300 nm samples have $R = 0.54$. This different composition means that there is less terbium or more iron atoms. Therefore, there may be, e.g., vacancies at the dodecahedral sites, or they may be occupied by an iron ion. Furthermore, the Tb^{3+} ion is known to form more stable Tb^{4+} ions in cubic materials [32] and tends to occupy

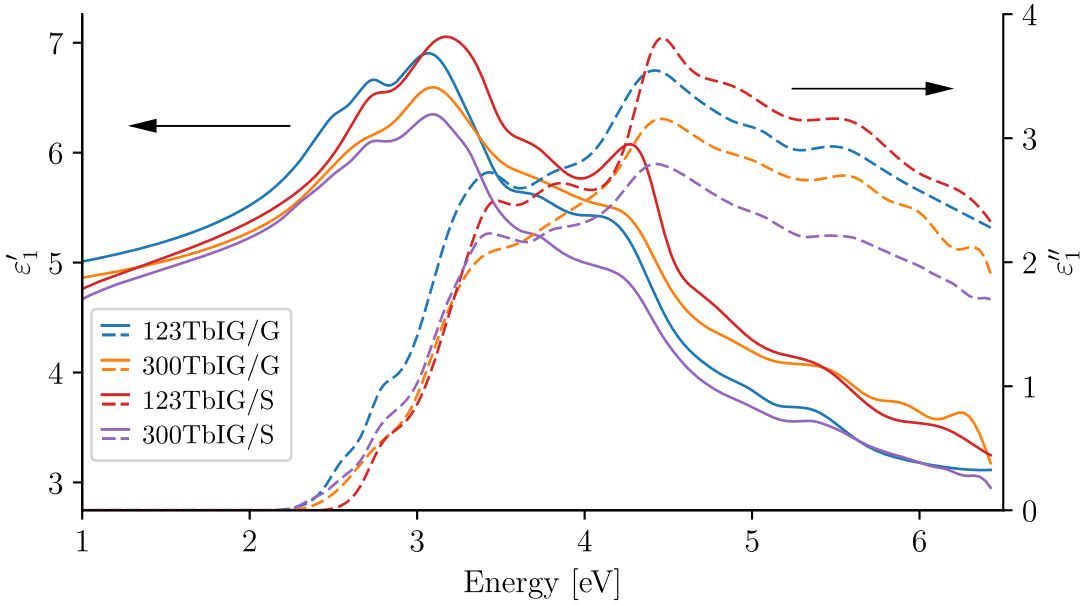

Figure 6.3: Fit relative permittivity of the non-doped TbIG samples.

octahedral sites [33]. The presence of Tb^{4+} can also cause the formation of Fe^{2+} and Fe^{4+} ions. All this effects can affect the optical and other physical properties.

The spectral shape is similar to the YIG spectrum reported in literature, e.g., in [16] and [17]. Iron garnets have a fairly large band gap, $\approx 2.5\,\text{eV}$ (indicated by an onset of imaginary part of ε_1 in Fig. 6.3), while the lattice absorption starts below 0.14 eV, making them particularly attractive for MO isolators in the infrared (IR) range. Several authors [34], [35], [36] explained the spectra at the onset of the absorption and in the visible spectrum. In two papers [37], [38], Scott et al. proposed that the optical transitions of YIG were assigned incorrectly and presented different absorption mechanisms.

It was established that the absorption of garnets at the optical frequencies mainly originates from iron ions. A decrease in absorption across the whole spectrum is observed when diluting the iron at the tetrahedral and octahedral sites. The contribution of the rare-earth ions is usually only minor. Parity-forbidden 4f-4f transitions, located in the IR-visible region, become allowed in the crystal field (CF) but are several orders weaker than iron transitions and not observable [39]. The charge transfer (CT) 4f-5d transitions in ultraviolet (UV) region are also much weaker than iron absorption bands. A stronger absorption can arise from Tb^{4+} ions. Weak absorption peaks around 2 eV and at the absorption edge were assigned to CF transitions between ^6S and ^4G terms that are spin and parity forbidden in the free Fe^{3+} ion. The lowest peak at 2.53 eV is probably corresponding to this type of transitions. The lowest transitions are expected to originate in the octahedral site since the CF splitting is larger than of the tetrahedral site. CF transitions are present up to 3.4 eV but are not visible due to the presence of much stronger transitions. Scott assigned absorption bands around 2.7 eV, 2.86 eV, 3.2 eV and 3.4 eV to the simultaneous CF excitation of two neighbouring Fe^{3+} ions. These transitions should occur at the sum of the energies of the two transitions and should have much higher oscillator strengths than single ion transitions. The observed peaks at 2.77 eV and 3.43 eV could be attributed

to this mechanism. CT transitions have two possible mechanisms that are hard to discern due to their similar manifestation. According to [40], CT transitions between O^{2-}-Fe^{3+} are situated at 2.9 eV and 3.16 eV. On the other hand, in [38], 8 expected transitions between 2.9 eV and 5.2 eV are assigned to CT between octahedral and tetrahedral sites, while the first O^{2-}-Fe^{3+} transition is expected above 4.4 eV. The strong peaks at 3.20 eV and 4.37 eV and also 3.79 eV observed in the spectra of 123TbIG/G may be attributed to CT transitions. However, it is probable that the contributions of different origins are overlapping in the spectra and are thus represented by one peak particularly at 3.2 eV where the biexciton CF transitions are still present. The strong transitions above 8 eV that contribute to the real part of the permittivity were attributed to transitions between oxygen 2p and iron 4s bands [40]. Based on the mechanism of the transitions in the UV region, the observed differences between the measured samples may be caused by defects in oxygen positions. The determined R values do not indicate the deficiency in iron, therefore the lower absorption should be caused by something different. Because the oxygens mediate the CT transitions in between the iron ions, the oxygen defects could decrease the frequency of the transitions and thus lowering the oscillator strengths of the peaks in the UV region.

The thicknesses and surface roughness values for non-doped TbIG are presented in Tab. 6.2. Fit thicknesses for samples on Si substrates do not signifi-

Sample name	t_n [nm]	t_f [nm]	r_s [nm]
123TbIG/G	123	113.72	8.77
300TbIG/G	300	262.65	10.53
123TbIG/S	123	126.77	9.77
300TbIG/S	300	295.75	15.26

Table 6.2: Nominal t_n and SE fit t_f thicknesses and surface roughness values r_s for non-doped TbIG samples.

cantly differ from nominal values. On the other hand, the samples deposited on GGG have smaller fit thicknesses by about 10 %. This can be caused by incorrect calibration of the PLD deposition rate, which can differ for different substrates. The roughness is within the acceptable range for PLD prepared garnets.

Spectral dependence of the diagonal element of permittivity tensor of doped samples compared to non-doped sample 123TbIG/G are shown in Fig. 6.4 and Fig. 6.5.

The thicknesses and surface roughnesses are listed in Tab. 6.3. It can be immediately seen that the bismuth substitution increases absorption in the whole region above the band gap. This observation does not agree with the results presented in [16], where the bismuth only slightly increases absorption near 3 eV. However, the authors measured bulk-like samples whose properties can significantly differ from thin layers. In [41], the absorption of Bi doped YIG increased with increasing bismuth content. The spectra of bismuth samples in this thesis with Bi contents of 0.5 and 0.06 do not substantially differ from each other despite having different content of bismuth. This can be explained by the fact that the preparation of bismuth garnets with ideal stoichiometry is challenging [42]. Therefore, the non-observed but expected absorption increase with increasing bismuth substitution may be compensated by decreased iron content. Additionally,

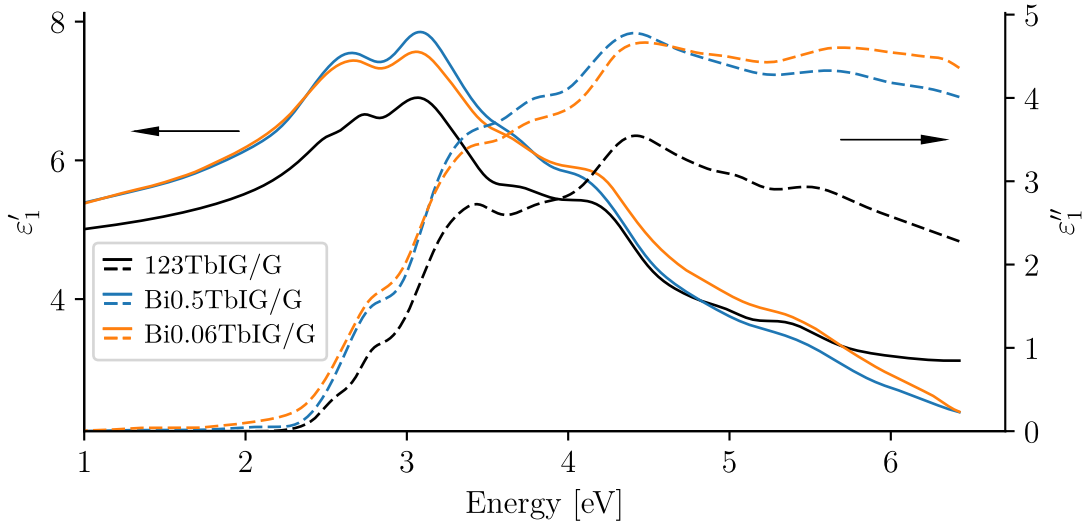

Figure 6.4: Fit relative permittivity of the samples Bi0.5TbIG/G and Bi0.06TbIG/G compared with sample 123TbIG/G.

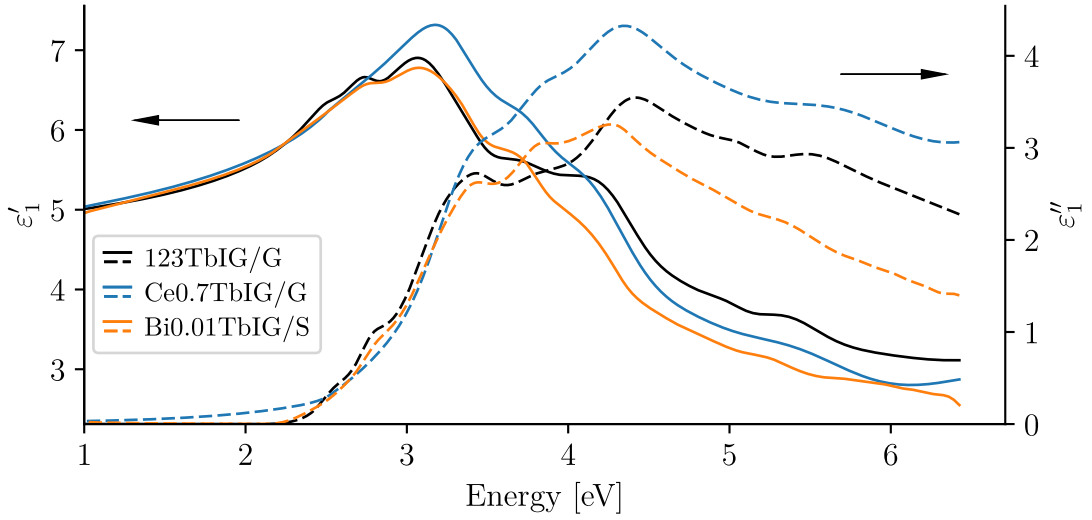

Figure 6.5: Fit relative permittivity of the samples Ce0.7TbIG/G and Bi0.01TbIG/S compared with the sample 123TbIG/G.

the proposed mechanism of enhanced absorption and MO activity of bismuth substituted iron garnets involves transitions between Fe^{3+} and Bi^{3+} ions [43] and therefore depends on iron concentration. The spectrum of Bi0.01TbIG/S is almost unchanged compared to 123TbIG/G (see Fig. 6.5), and the minor differences can be explained by the reasons mentioned in previous paragraphs.

The Ce0.7TbIG/G spectrum exhibits increased absorption as well, compared to the sample 123TbIG/G. It also displays increased absorption in the IR region, around 1.4 eV. This absorption is thought to originate in intraionic electric-dipole 4f-5d transitions in Ce^{3+} ion [44], [45], and is of particular interest for MO applications. Absorption at higher energies is probably coming from higher excited states of Ce^{3+} that are situated at 2.1 eV and 3.1 eV [46]. Absorption in UV is not addressed in the literature and is possibly not connected to Ce but to the differences in TbIG host material, probably due to higher content of iron.

Sample name	t_n [nm]	t_f [nm]	r_s [nm]
Ce0.7TbIG/G	80–110	76.15	1.72
Bi0.5TbIG/G	-	71.97	5.28
Bi0.06TbIG/G	86	87.53	9.87
Bi0.01TbIG/S	-	86.36	19.96

Table 6.3: Nominal t_n and SE fit t_f thicknesses and surface roughness values r_s for doped TbIG samples.

6.2 Magneto-optical properties

The MOKE spectra were measured using the rotating analyzer technique in polar configuration between 1.4 eV to 4.5 eV. The range was limited in the UV by the absorption of the used optical components and in the IR by the range of the used spectrometer. Because it is problematic to perform the MOKE measurement at normal incidence, the experiment was carried out at around 10° angle of incidence. This does not significantly impact the measurement, only the amplitude is slightly lower, but the spectral dependence is the same [6]. This is because the polarization change only happens for the part of the wave vector that is parallel to the magnetization vector that creates the optical anisotropy. Optical anisotropy perpendicular to the magnetization is equal to zero. Firstly, the samples were measured with a polished substrate backside. Then the backside was roughened with a diamond pen to eliminate backside reflections, and the MOKE spectra were measured again.

The Faraday effect was measured in the same energy range, but the spectra are affected by the sample absorption and have significant error above 4 eV. Faraday effect was measured only for samples on GGG substrate since the Si is opaque above 1.12 eV. The Faraday spectra were corrected for the paramagnetic contribution of GGG (Fig. 6.6) and normalized to thickness. The sharp peaks visible in the spectra are absorption peaks of Gd^{3+}.

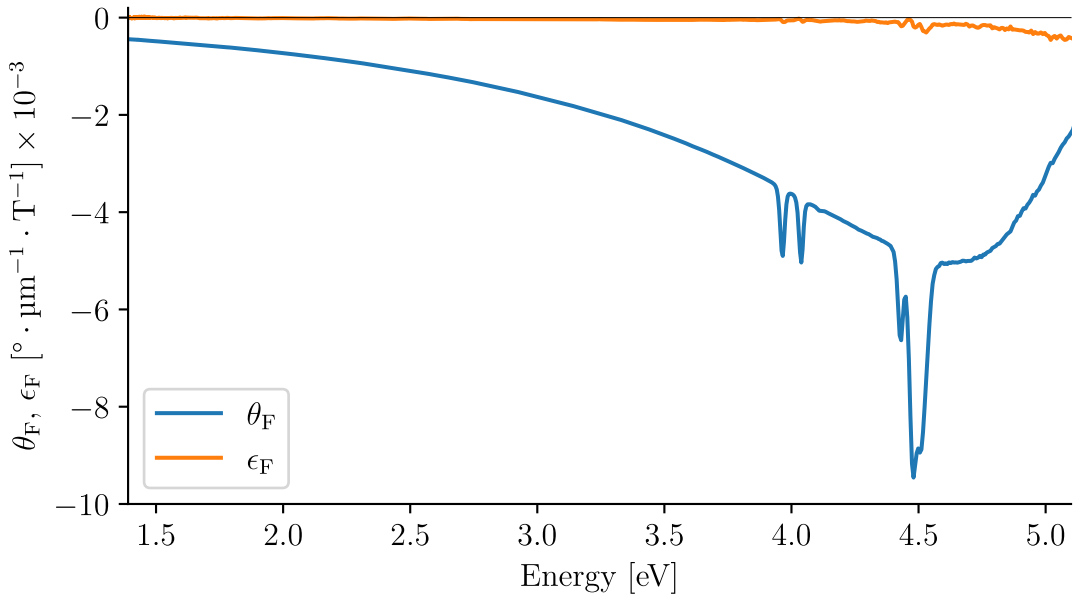

Figure 6.6: Faraday rotation and ellipticity of GGG.

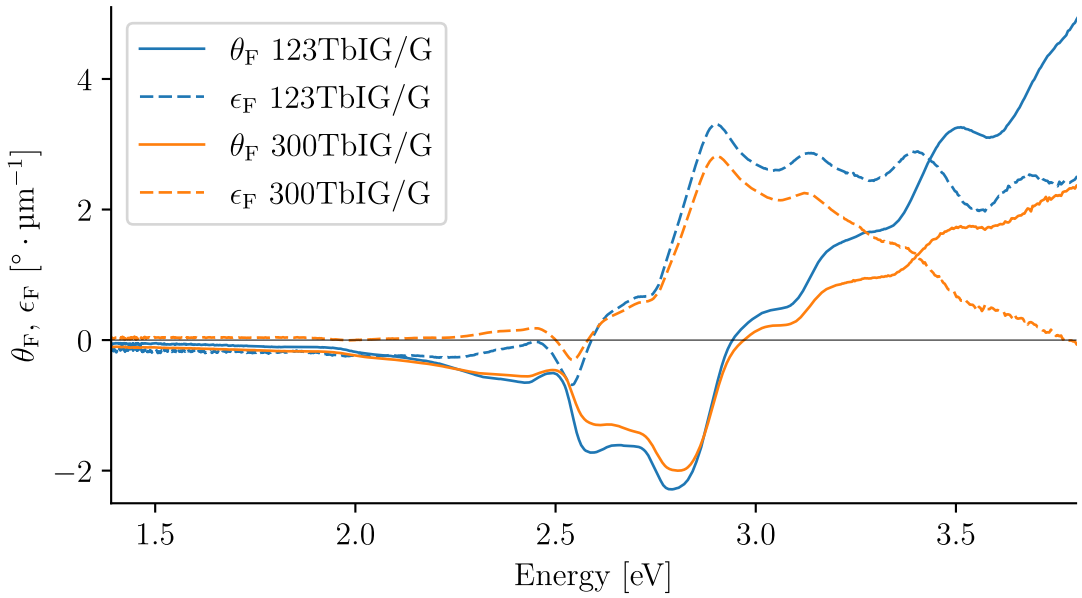

Figure 6.7: Measured Faraday rotation and ellipticity of non-doped TbIG on GGG substrate.

Faraday spectra of non-doped garnet samples on GGG substrate are shown in Fig. 6.7. The spectral dependence agrees with the literature [47], but the magnitude is approximately two times larger in samples measured in this thesis. The difference can be caused by different qualities of the films, as is discussed in the article and above text. The difference between the samples can be caused by differences in composition. The 300TbIG/G spectra above 3 eV are skewed because of significant absorption of the sample resulting in negligible intensity and worse sensitivity of the measurement. Furthermore, the 0.62 T field produced by the magnet was not sufficient to saturate the magnetization of the sample 300TbIG/G. This will be discussed in more detail later in the chapter.

MOKE spectra of non-doped TbIG on polished and roughened GGG substrate are shown in Fig. 6.8 and Fig. 6.9.

The difference between the spectra for polished and roughened backside is significant. Both samples show a notable difference in Kerr rotation and 300TbIG/G also for Kerr ellipticity. The oscillatory behaviour below 3 eV originates in the interference of light reflected from the surface and the layer/substrate interface. This is more pronounced for the thicker sample. Additional rotation is produced by the double Faraday rotation of the substrate itself, which can be greatly reduced by the mentioned roughening. The reflection from the bottom of the substrate will then be supressed by the light scattering.

These comparisons also point to another important fact: the penetration depth is large enough to allow the light reflected from the bottom of the layer to reach the detector up to around 3.15 eV. This observation will become helpful in discussion of hysteresis measurements later in this chapter. The interference is also visible in MOKE spectra for non-doped samples on Si substrate (Fig. 6.10), and is more pronounced because of bigger difference between layer and substrate refractive indices than for the layer/GGG case.

Utilizing the knowledge of the spectral dependence of MOKE and Faraday effect and diagonal element of permittivity tensor, Yeh formalism can be used

to calculate the spectral dependence of the off-diagonal elements of the permittivity tensor. The off-diagonal permittivity can be calculated both from MOKE or Faraday spectra. The accuracy of the calculations can then be checked by modelling the other spectra that were not used for the calculation.

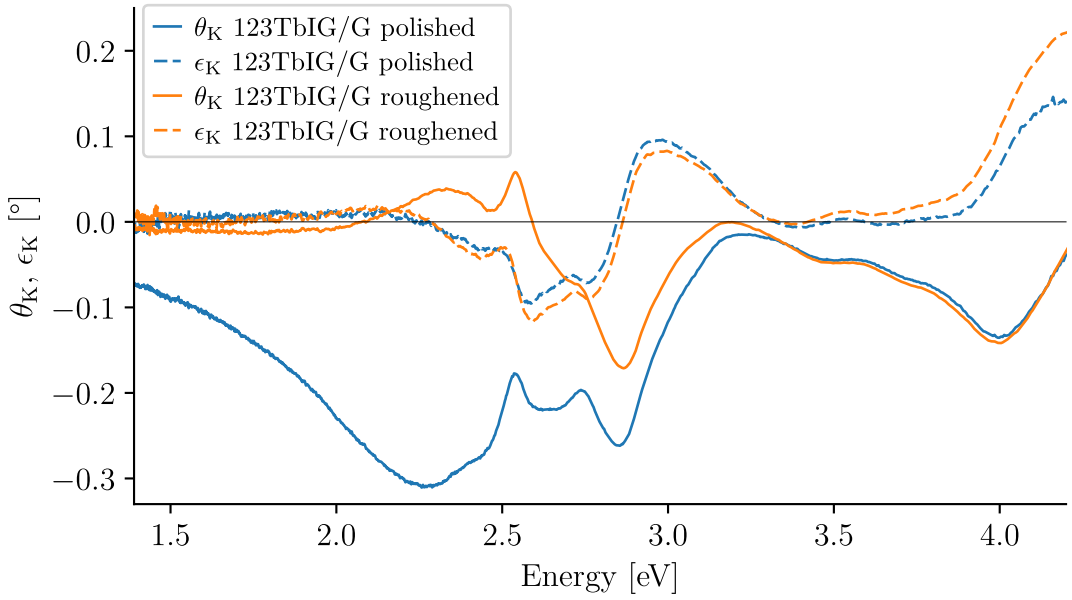

Figure 6.8: Measured Kerr rotation and ellipticity of 123TbIG/G with polished and roughened backside.

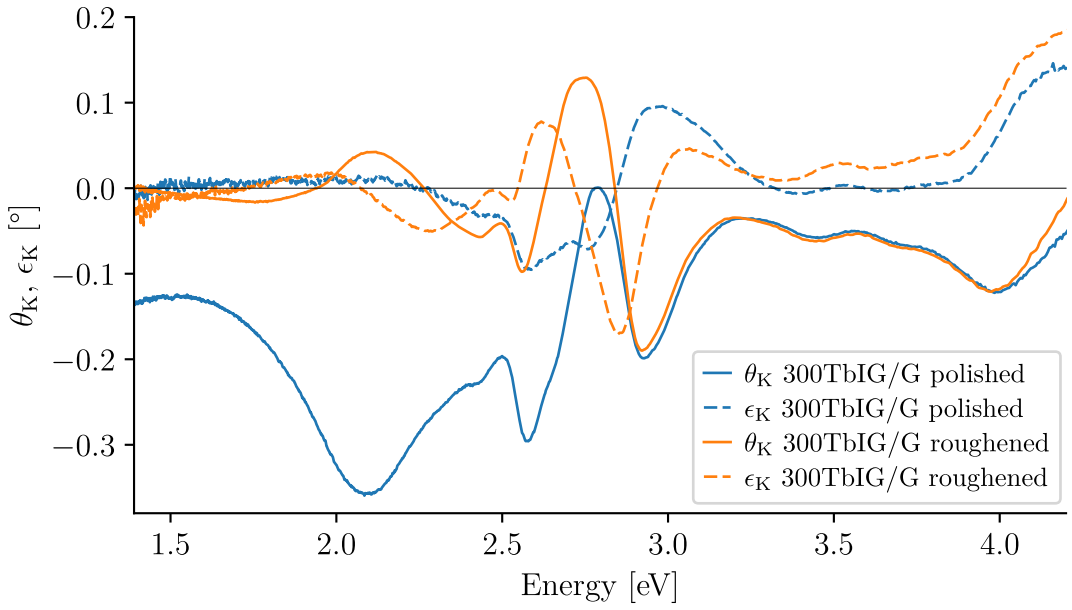

Figure 6.9: Measured Kerr rotation and ellipticity of 300TbIG/G with polished and roughened backside.

The off-diagonal permittivity ε_2 of non-doped TbIG was calculated from all measurements of all samples. The spectral dependencies are compared in Fig. 6.11 and Fig. 6.12. The ε_2 spectra calculated from Kerr measurement of the samples 123TbIG/S and 123TbIG/G significantly deviates from the rest between 2.5 eV

and 3.2 eV. This can be caused by slightly different thicknesses across the layer, which is common in PLD prepared samples. The thicknesses can therefore be different from the fit thickness which results in the inaccuracy of the calculated ε_2 spectra. The 123TbIG/G MOKE spectra may be inaccurate also because

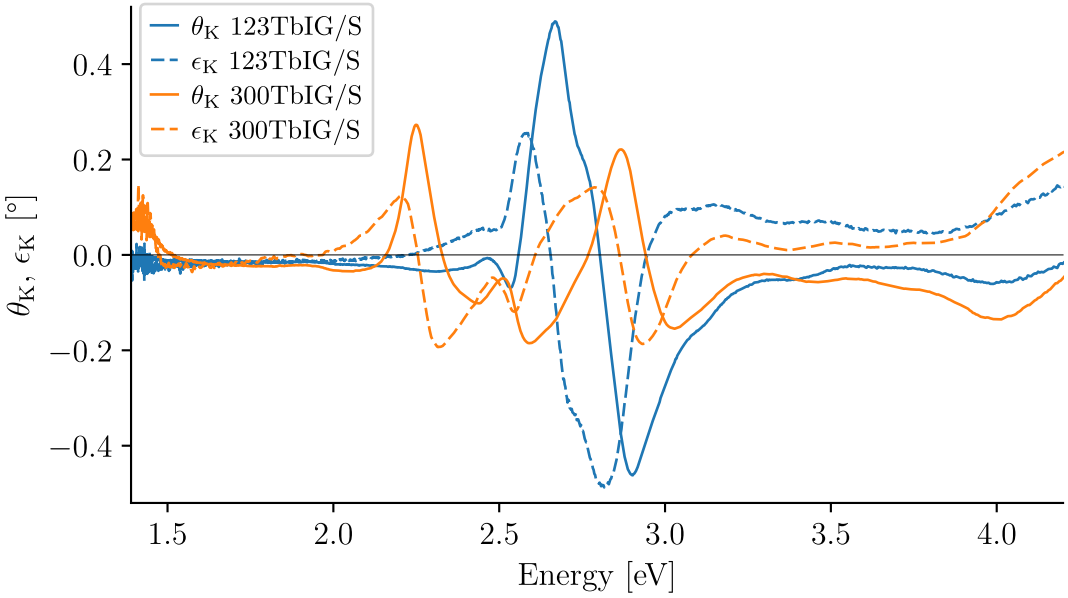

Figure 6.10: Measured Kerr rotation and ellipticity of non-doped TbIG on Si substrate.

despite the roughening of the backside, some light might be still reflected to the detector. The sensitivity of Yeh formalism is also noticeable because of the peak at 2 eV in the real part of off-diagonal permittivity of the sample 123TbIG/G. The MOKE spectra do not show any particular disturbance around this energy (Fig. 6.8). The ε_2 spectra calculated from the Faraday spectra of 300TbIG/G have lower amplitude caused by the inability to saturate the sample at 0.62 T (will be discussed in the following text). Above 3.5 eV, this calculated permittivity is skewed due to inaccuracy of the Faraday spectra caused by high absorption. The inverted peaks at 4 eV are "oversubtracted" peaks of GGG substrate. This can be a helpful indicator of the error in Faraday rotation spectra. If the peaks are more visible, it means that the measured Faraday rotation is lower than it is supposed to. Other than that, the permittivities are consistent between each other. Besides reasons already mentioned in this paragraph, the small differences between the samples could be also caused by factors mentioned earlier in section about optical properties. Most probable is that the stoichiometries of the samples are different or some defects are present. Permittivities calculated from Faraday spectra will be generally more accurate considering the Faraday effect is less sensitive to the influence of multiple reflections at the interfaces.

The permittivity spectral shape is similar to that of YIG shown, for example, in [17], [48] and [49], which indicates that the majority of the MO activity originates in iron sublattices as in YIG. The Tb^{3+} has observable contribution in the IR region [50], [51]. One can see that the off-diagonal permitivity has indeed complex spectral dependence and the identification of the peaks is thus not an easy task. Nonetheless, many peaks were identified, for example, in [48],

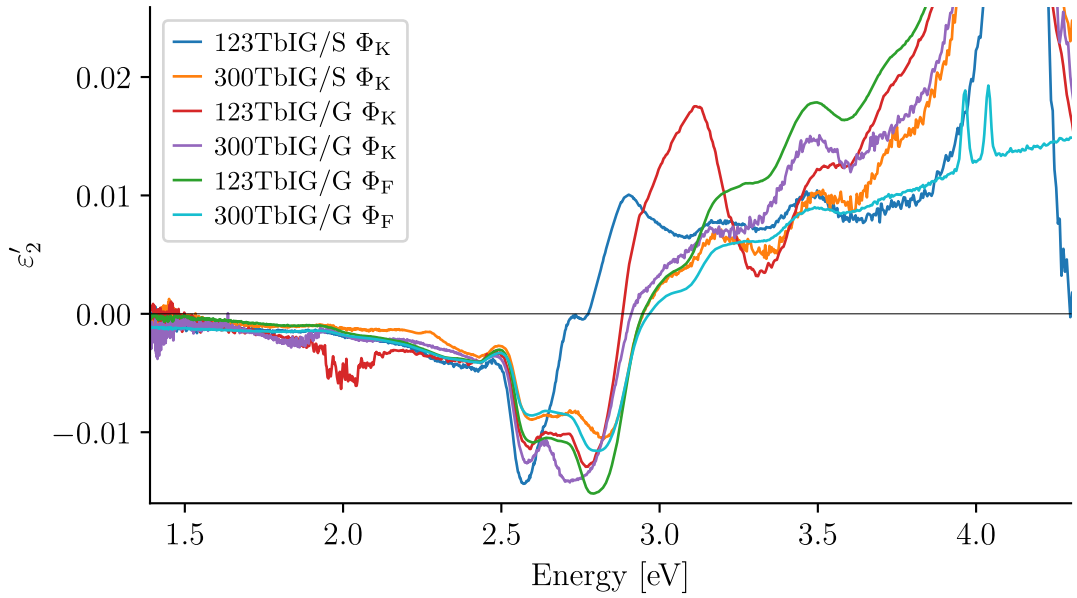

Figure 6.11: Calculated real part of off-diagonal permittivity of TbIG from all measurements of all samples. The Φ_K and Φ_F labels indicate which spectra were used for calculation.

[52], [53]. The literature is consistent in explaining the permittivity dependence entirely by paramagnetic transitions with a few exceptions. Some of the paramagnetic transitions have been matched to peaks in absorption spectra. Some of the peaks at the energies up to 2.5 eV were attributed to crystal field transitions. There are two peaks in visible in the ε_2 spectra that probably belong to this transitions. In the range from 3 eV to 4.5 eV the transitions are thought to be due to the biexciton excitations. This hypothesis is supported by discussion in [49], where the spectrum is separated to individual lattice contributions, with overlapping transitions. The transition around 2.85 eV is with high probability charge transfer transition which exhibits diamagnetic line shape [16], [48].

The observation that the YIG ε_2 spectrum is predominantly paramagnetic is rather surprising since the ground state of Fe^{3+} has zero angular momentum. Therefore, there should be no spin-orbital splitting which is required for existence of paramagnetic transitions. It has been proposed that the ground state can acquire nonzero orbital momentum by hybridizing its orbitals with orbitals of spin-orbit split lowest excited term of neighbouring ion [52].

In figures Fig. 6.13 and Fig. 6.14 are shown the measured MOKE spectra of sample Bi0.01TbIG/S and Faraday effect spectra of doped samples on GGG substrate. One can immediately notice the giant enhancement of the Faraday rotation and ellipticity by bismuth doping. What is interesting is that the substantial increase in bismuth doping from 0.06 to 0.5 does not translate to increase in MO activity. The magnitude of Faraday effect only slightly increases for the more doped sample. The sample doped with Ce also displays an increase in Faraday effect. Significant is the increase of Faraday rotation at the lower side of measured spectral range. Both Bi and Ce doped TbIG are therefore promising materials for application in MO isolators in telecommunication at IR wavelengths [54].

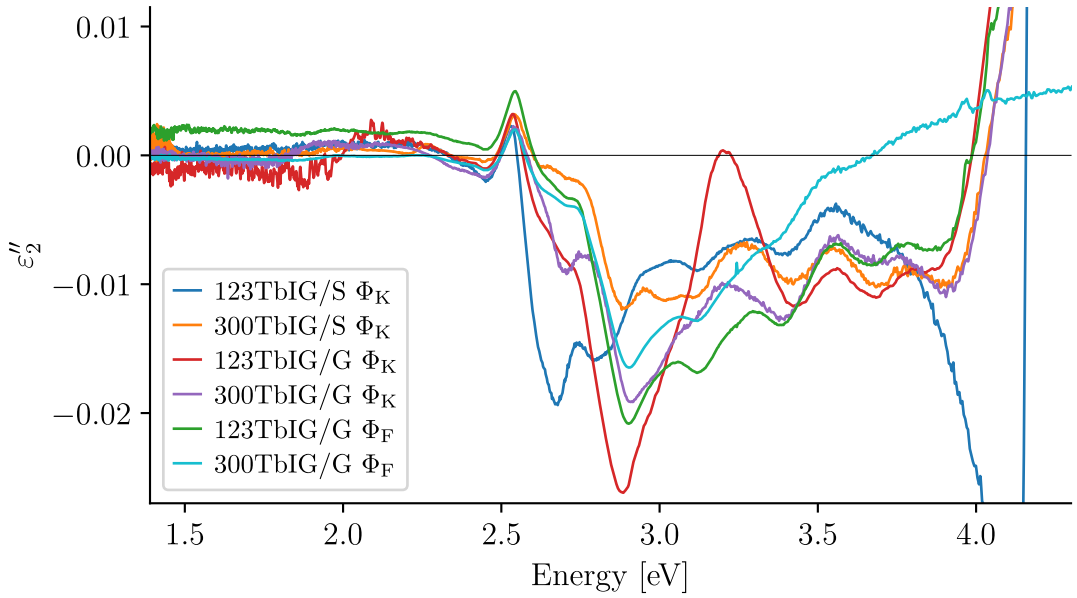

Figure 6.12: Calculated imaginary part of off-diagonal permittivity of TbIG from all measurements of all samples. The Φ_K and Φ_F labels indicate which spectra were used for calculation.

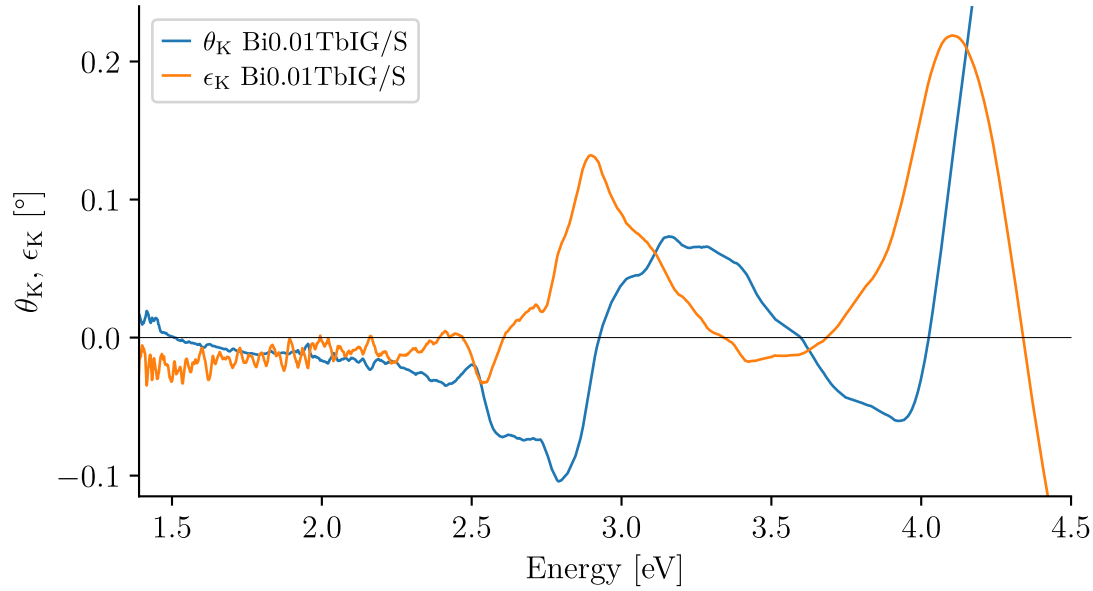

Figure 6.13: Measured MOKE spectra of the sample Bi0.01TbIG/S.

The calculated off-diagonal permitivity spectra for doped samples are shown in Fig. 6.15 and Fig. 6.16. The ε_2 spectra of samples on GGG were calculated from Faraday effect and the permittivity of the sample Bi0.01TbIG/S was calculated from MOKE. The ε_2 of the sample Bi0.01TbIG/S does not visibly differ from that of non-doped TbIG, so the effect of such small substitution is negligible. The significant increase of Faraday effect of the Ce doped sample is caused by the paramagnetic transition centred at around 1.4 eV. Another paramagnetic transition with negative contribution is probably located at 3.1 eV but is of no particular interest for potential applications. The increased Faraday effect of Bi doped sam-

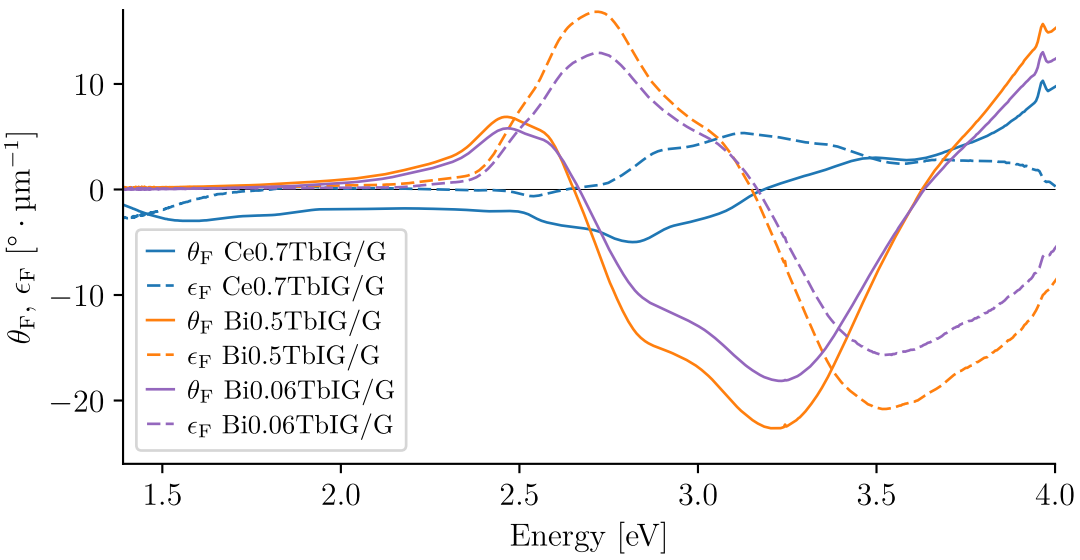

Figure 6.14: Measured Faraday rotation and ellipticity spectra of doped samples on GGG substrate.

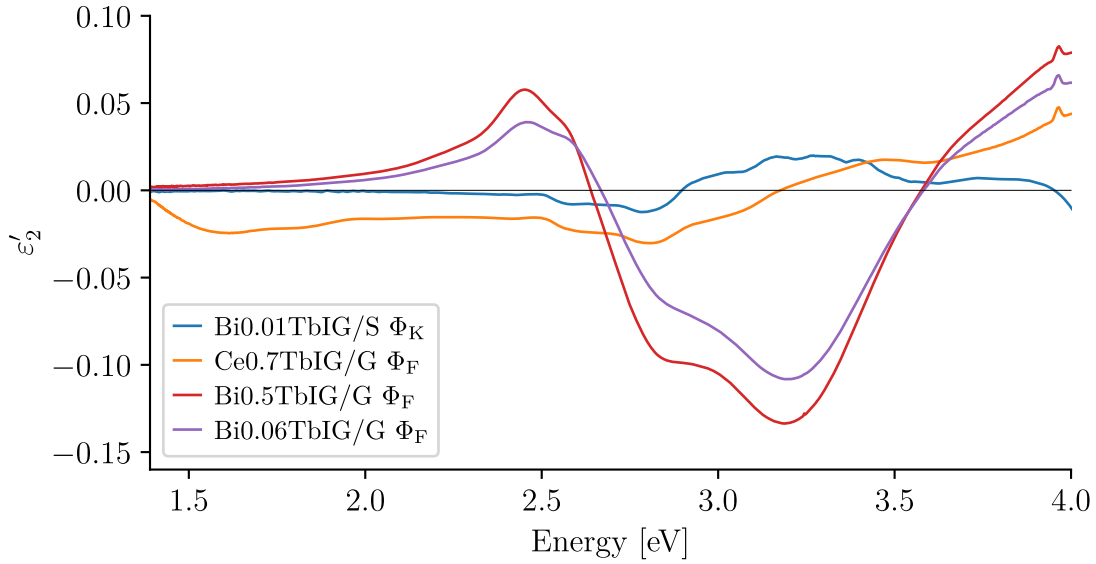

Figure 6.15: Calculated real part of off-diagonal permittivity of TbIG from MOKE and Faraday measurements. The Φ_K and Φ_F labels indicate which spectra were used for calculation.

ples is mainly caused by two diamagnetic transitions at 2.6 eV and 3.15 eV and a smaller diamagnetic transition at 3.9 eV [55]. The original spectra remain largely unaffected. This suggests that the doping with bismuth introduces additional mechanism to the MO activity. The additional mechanism involves spin-orbit splitting of the excited states and covalent interactions between Fe^{3+} and Bi^{3+} [56]. It was determined that the larger peak at 3.15 eV involves transition in the octahedral site while the other two peaks belong to tetrahedral site.

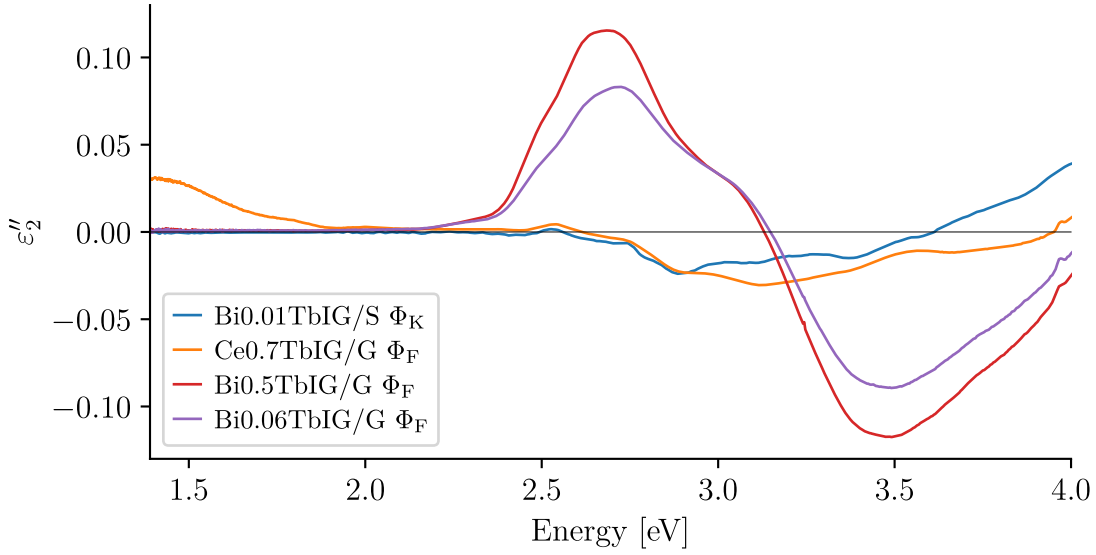

Figure 6.16: Calculated imaginary part of off-diagonal permittivity of TbIG from MOKE and Faraday measurements. The Φ_K and Φ_F labels indicate which spectra were used for calculation.

Spectral hysteresis loops

As was discussed in previous paragraphs, the analysis of the MO spectra is a difficult task. Current methods of assigning MO to the garnet sublattices involve diluting the iron ions with nonmagnetic ions, which preferentially replace iron at one of the sites, and comparing the measured spectra. Some peaks in the MO spectra can be assigned based on the change of the shape of the spectra with temperature. One possible way how to facilitate the analysis is the measurement of spectral hysteresis loops. If the magnetic sublattices of the garnet have different hysteresis behaviour, this should be visible in the hysteresis loops of the MO spectra for transitions coming from different sublattices. This would greatly simplify the assignment of observed peaks. The analysis of hysteresis loops was performed on bismuth iron garnet by Deb et al. [57]. The authors observed anomalous hysteresis loops that were caused by two diamagnetic transitions originating in the two sublattices with opposing magnetization.

For the purpose of this thesis, spectral hysteresis loops were measured on three samples: 300TbIG/G, 123TbIG/G and 0.5BiTbIG/G. The spectra are shown in figures 6.17, 6.18 and 6.19. All three samples exhibit energy dependent shape of the hysteresis loops. This effect is most pronounced in the sample 300TbIG/G, in which the hysteresis loops display significantly different shape in an energy window just 0.06 eV wide. According to the [57], the hysteresis loop can be represented by an error function and thus the total Kerr hysteresis loop is expressed as the sum of three error functions for each sublattice

$$\theta_K = \sum_{i=1}^{3} A_i \operatorname{erf}\left(\frac{B - B_{Ci}}{B_{Vi}}\right),$$

where A_i is the amplitude of the Kerr effect of the sublattice, B the applied external field, B_{Ci} the coercive field, and B_{Vi} the field at which the magnetization of the sample is saturated. After inspection of the spectra, it was concluded that

the observed hysteresis consists of two different shapes. Therefore, the spectra were modelled by two error functions. Firstly, the fit parameters for the error functions were obtained at a fixed energy. Then, the parameters B_{Ci} and B_{Vi} were held constant and the amplitudes were fit for the whole spectrum. The two fit error functions were sufficient to reproduce the observed hysteresis loops in the whole spectral range.

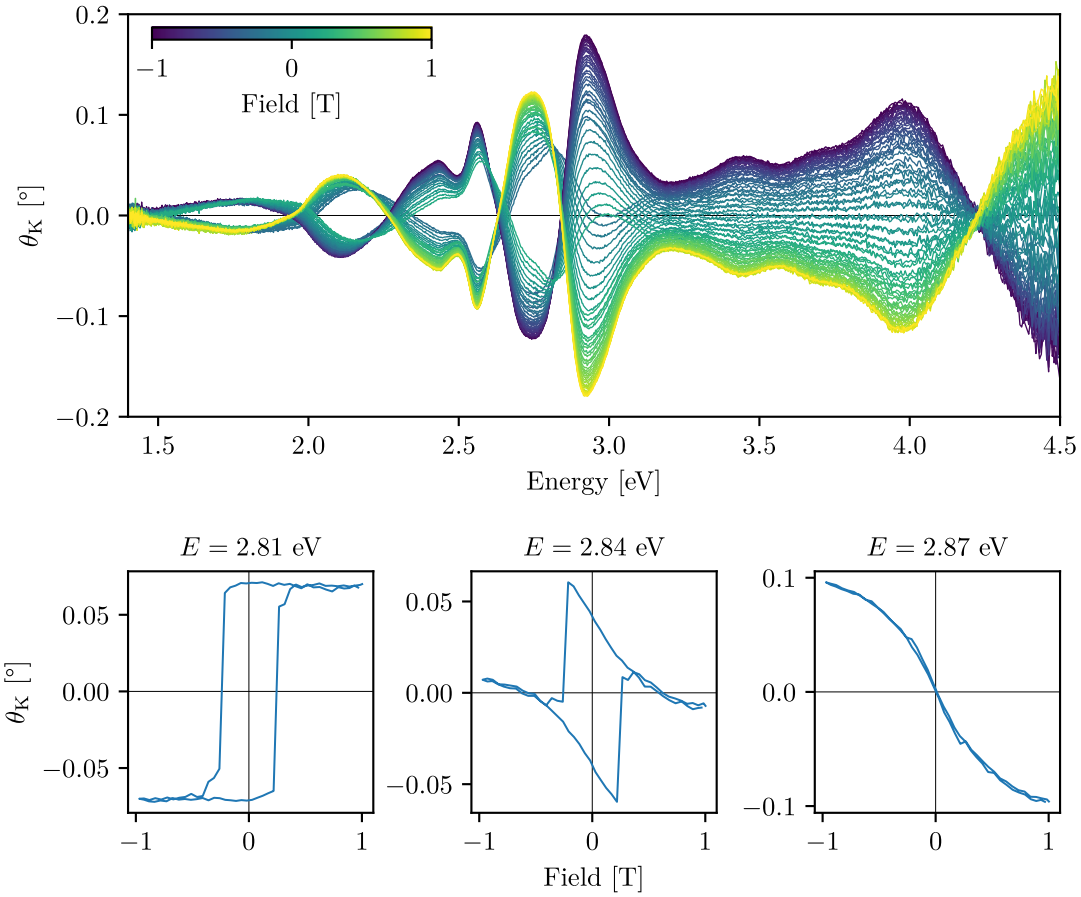

Figure 6.17: Measured Kerr rotation spectral hysteresis loops of the sample 300TbIG/G. The top graph illustrates the spectral shape with colour coded applied external field values. The lower graphs depict slices through the spectrum at energies $E = 2.81\,\text{eV}$, $2.84\,\text{eV}$ and $2.87\,\text{eV}$.

Example of the hysteresis loop decomposition of the sample 300TbIG/G is shown for two energies in Fig. 6.20. The two loops have very different behaviour. The loop labelled as *loop 1* displays low remanence and has a low value of coercive field. On the other hand, the loop labelled as *loop 2*, displays a hysteresis expected for easy anisotropy axis, has remanence equal to saturation value and has a high coercive field. It the following text it will be referenced to these loops as *low* H_C for loop 1 and *high* H_C for loop 2. The spectral dependence of the amplitude of the two loops is shown in Fig. 6.21.

The decomposition of the spectrum into two independent loops was also performed for the samples 123TbIG/G, and 0.5BiTbIG/G (Fig. 6.22, Fig. 6.23). The hysteresis shape of the two loops is basically the same as the shape of the loops of the sample 300TbIG/G (Fig. 6.20).

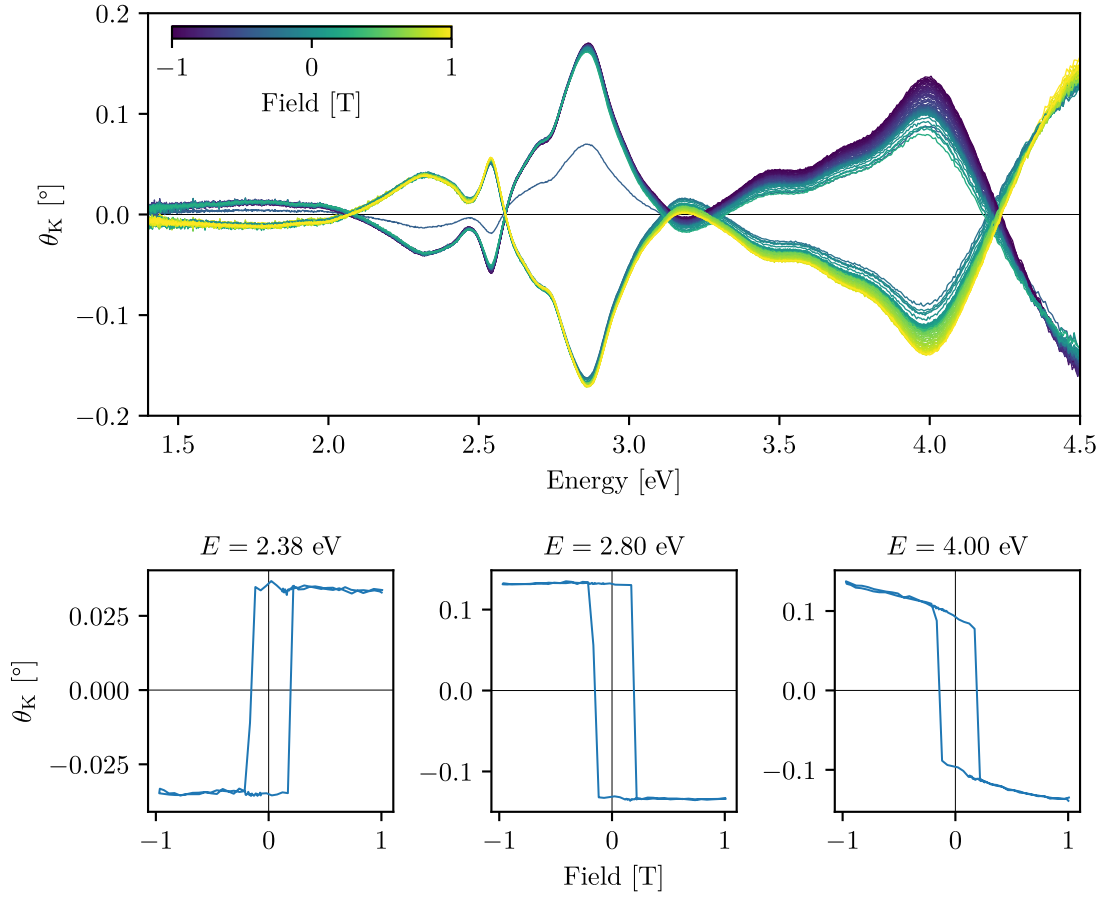

Figure 6.18: Measured Kerr rotation spectral hysteresis loops of the sample 123TbIG/G. The top graph illustrates the spectral shape with colour coded applied external field values. The lower graphs depict slices through the spectrum at energies $E = 2.38\,\text{eV},\ 2.8\,\text{eV}$ and $4\,\text{eV}$.

The spectral dependences of the amplitude do not indicate that they represent the Kerr contributions of the individual sublattices. For the sample Bi0.5TbIG/G (Fig. 6.23), one would expect similar dependence to that in [57]. The contribution to the spectra predominantly comes from the high H_C loop, while the contribution from the low H_C loop is only very weak. It was also determined that the peak around 3.15 eV originates in the octahedral site while the peak at 3.9 eV at the tetrahedral site. The two loops, however, contribute to both of those peaks, with different magnitude.

The spectral contributions to the Kerr rotations of the samples 300TbIG/G and 123TbIG/G are very different but a similar behaviour would be expected from the same material. In decomposed loop spectra of the sample 300TbIG/G, the two loops contribute with similar strength to the spectrum up to the 3.4 eV, but above this energy, only the low H_C loop contributes to the spectra. On the other hand, the Kerr rotation of the sample 123TbIG/G is predominantly mediated by the high H_C loop while the low H_C loop contribution only weakly increases in the UV region.

Furthermore, the hysteresis shape of the two loops for the three measured samples is very different. It is improbable that the remanence would be caused

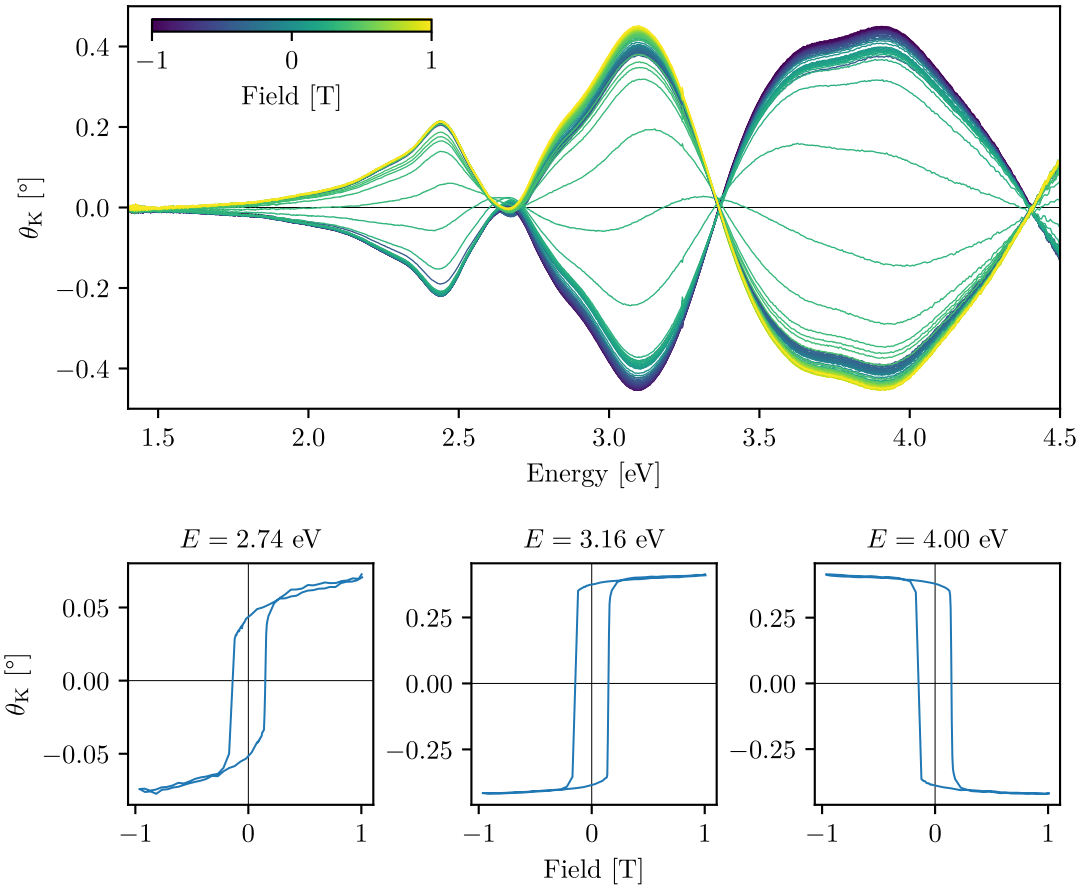

Figure 6.19: Measured Kerr rotation spectral hysteresis loops of the sample Bi0.5TbIG/G. The top graph illustrates the spectral shape with colour coded applied external field values. The lower graphs depict slices through the spectrum at energies $E = 2.74\,\text{eV}$, $3.16\,\text{eV}$ and $4\,\text{eV}$.

only by one sublattice (high H_C loop) and that the other sublattice would exhibit no hysteresis. In a material where the antiferromagnetic exchange enforces magnetic order, a behaviour where the sublattices have similar values of coercive field and remanence would be expected.

Because of this reasons, it was concluded that the individual contributions of the low H_C and high H_C do not represent the Kerr rotation of the particular sublattices of the studied samples. One probable explanation of the observed effect is that the decomposed spectra represent the contributions of two layers with different magnetic anisotropy within the TbIG layer. It is expected that the TbIG grown on GGG would display PMA due to the compressive strain caused by lattice mismatch between the GGG and the TbIG layer [58], and this was indeed reported for example, in [47] and [59]. Based on the square shape of hysteresis loops, the samples 123TbIG/G and Bi0.5TbIG/G exhibit the PMA. The small contribution of the low H_C loop in both samples is probably caused by a thin layer at the surface that has different magnetic anisotropy than the rest of the layer. The different properties of the surface layer may be caused for example, by the heat treatment of the sample after the layer deposition and as a result the stoichiometry may be different. Another possible origin of the observed

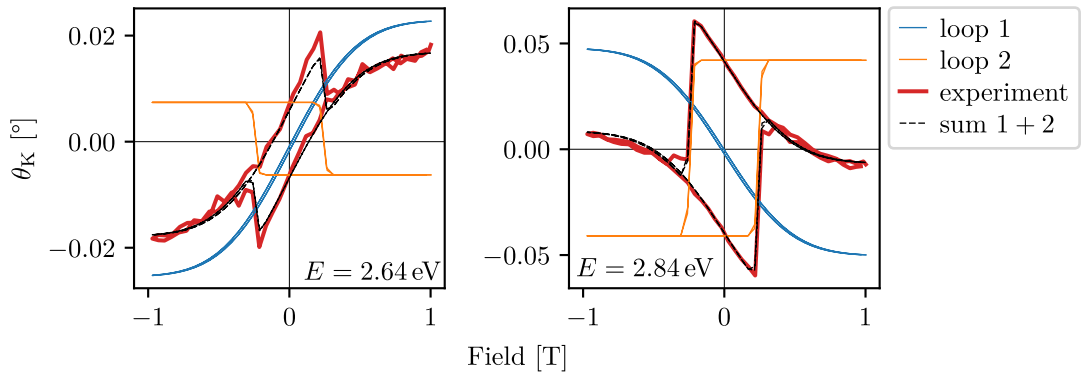

Figure 6.20: Decomposition of the measured Kerr hysteresis loops of the sample 300TbIG/G shown at two energies $E = 2.64\,\mathrm{eV}$ and $2.84\,\mathrm{eV}$.

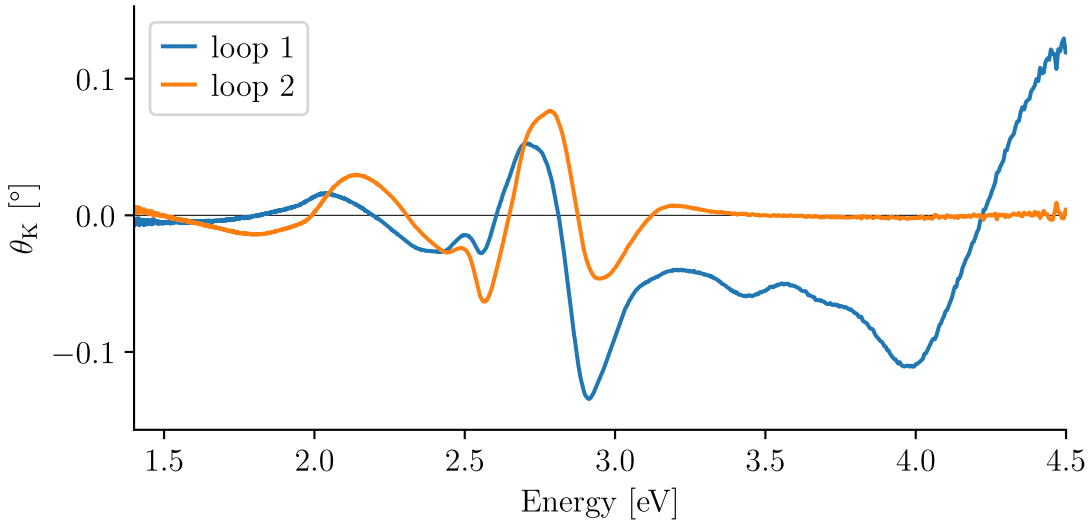

Figure 6.21: Spectral dependence of the amplitude of the two loops that reproduce the measured Kerr spectrum of the sample 300TbIG/G.

phenomena is that the surface of the layer acts as a defect to the periodicity of crystal and therefore the electronic, and consequently other physical properties, can be different from the rest of the sample.

The decomposed spectra of the sample 300TbIG/G(Fig. 6.21) can be explained in similar way. The low H_C top layer is, however, much thicker. The thickness dependent measurements reported in [59] indicate that the PMA may not be retained when increasing the thickness of the TbIG. The 300 nm layer may have formed two layers while only the bottom part retained the expected magnetic anisotropy. Above approximately 3.4 eV, light is not capable of reaching the bottom layer due to the absorption and therefore the contribution to the Kerr rotation originates only from the reflection at the top layer. Below 3.4 eV, the absorption is low enough that the light also interacts with the bottom layer that has slightly different optical properties due to the different magnetic anisotropy. This would also explain the improvement of the SE fit when the graded layer model was used. The thicknesses of the layers are such that the reflected light can interfere, resulting in observed oscillations in Kerr spectrum. The penetration depth argument is supported by two figures (Fig. 6.8, Fig. 6.9), which depict

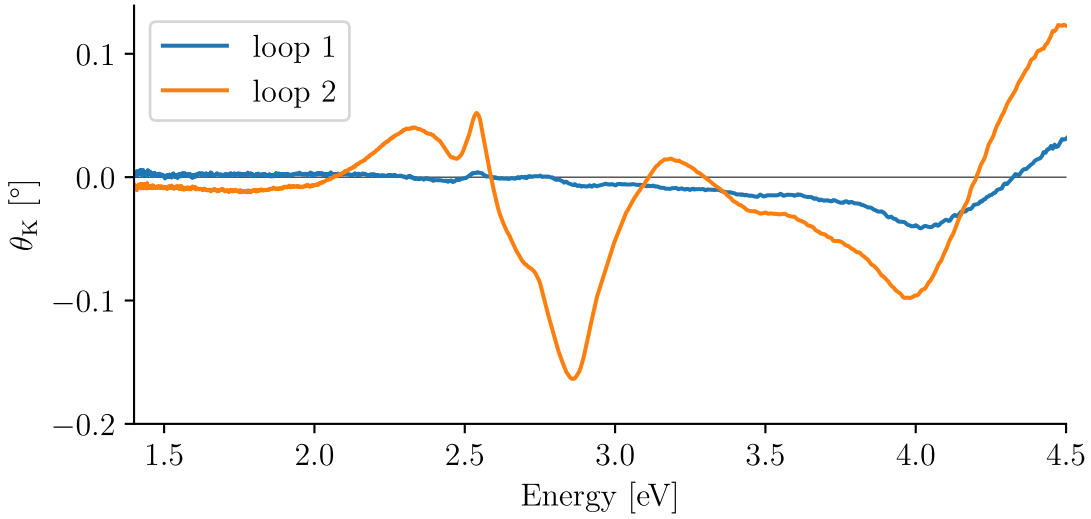

Figure 6.22: Spectral dependence of the amplitude of the two loops that reproduce the measured Kerr spectrum of sample 123TbIG/G. The low $H_C$and high $H_C$loops have the same hysteresis shape as for the sample 300TbIG/G (Fig. 6.20).

the difference between Kerr spectra before and after roughening of the substrate backside. There is a difference up to around 3.3 eV indicating that light is able to penetrate the TbIG layer to this energy. The hysteresis loops of the sample 300TbIG/G also explain one possible reason why the calculated ε_2 spectra were lower in magnitude, which is that the 0.62 T field used in the Faraday measurement was not sufficient to saturate the low H_C layer that contributes substantially to the spectra.

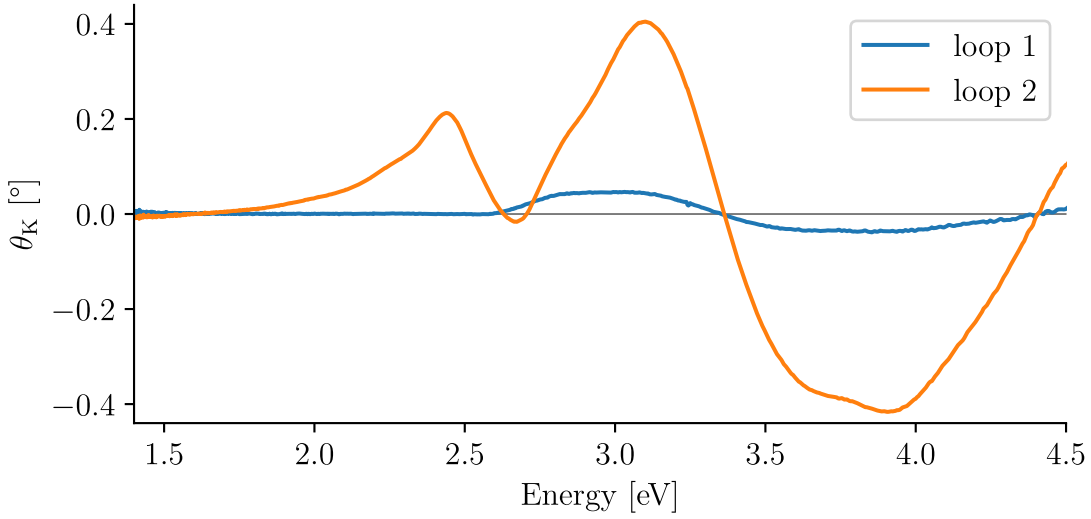

Figure 6.23: Spectral dependence of the amplitude of the two loops that reproduce the measured Kerr spectrum of sample Bi0.5TbIG/G. The low $H_C$and high $H_C$loops have the same hysteresis shape as for the sample 300TbIG/G (Fig. 6.20).

The individual contributions of the sublattices were thus not observed in the polar MOKE measurement. The square hysteresis shape shows that the magnetization of the measured section of the sample is coherently flipped at once in

a narrow window of magnetic field values. The sublattices probably have very similar coercive fields and fields at which the magnetic saturation is reached and therefore the individual contributions cannot be distinguished. It is possible that the contributions of the sublattices would be more visible in a longitudinal MOKE configuration. The magnetic field would act in a direction of the hard axis and the hysteresis parameters of the individual sublattices could be more pronounced. This was probably the reason for the successful decomposition done in [57], since the investigated sample had an in-plane easy axis and the measurement was done in the Faraday configuration. The spectral hysteresis measurements showed that for samples that exhibit PMA, the MOKE measured in a polar configuration may be sensitive to different properties of the layers within the deposited layer.

7. Conclusion

This thesis was focused on systematic investigation of the optical and magneto-optical properties of non-doped and doped terbium iron garnet thin films.

The spectroscopic ellipsometry was used to obtain spectral dependence of optical constants, thicknesses and surface roughness values of all samples. The non-doped samples exhibited variations in the optical constants that could be explained by various reasons, such as different stoichiometry, defects in the material and different deposition parameters. The bismuth doped terbium garnets displayed increased absorption above the band gap, compared to the non-doped garnets, however, the increased absorption in the UV is not consistent with the data reported in literature. This could be connected to the difficulty of preparing stoichiometric bismuth doped garnet layers and therefore the optical properties can differ for similar reasons as in non-doped terbium garnets. The Ce doped terbium garnet exhibited increased absorption in the IR region caused by the intraionic transitions of Ce^{3+}. Higher excited states probably contribute to the absorption in the visible region.

The measured MOKE and Faraday spectra were used for the calculation of the spectral dependence of the off-diagonal element of the permittivity tensor. The ε_2 spectra largely resemble the spectra of YIG, and therefore the majority of the MO activity originates from the iron ions. The terbium displays observable MO activity in the IR region. The samples doped with Bi and Ce also exhibited spectra similar to other garnets doped with these elements. The Ce doped garnets display increased MO activity at around 1.4 eV. The Bi doped samples exhibit giant increase of the MO effects in the whole measured region. The effect was attributed to covalent interactions of Fe^{3+} and Bi^{3+}. The MO transitions were located at the same energies as reported in the literature. The ε_2 spectra of the Bi0.01TbIG/S sample did not significantly differ from that of non-doped terbium garnets indicating that the doping level is insufficient to enhance the MO activity.

MOKE spectral hysteresis loops were measured in the polar configuration for three samples on GGG substrate, for the purpose to separate the sublattice contributions. The spectra were decomposed into two loops that significantly differed in their hysteresis behaviour. One loop exhibited almost non-existent coercive field and remanence, while the second loop had properties that would be expected for the easy axis direction, i.e. it had high coercive value and remained at saturation in zero external field. Based on the spectral contributions of these loops and their hysteresis parameters, it was concluded that these spectra do not agree with expected contributions of the garnet sublattices. Instead, it was concluded that the different loops belong to two layers with different magnetic anisotropy within the deposited layer. For samples 123TbIG/G and Bi0.5TbIG/G it was concluded that the low coercivity loop belongs to the thin surface layer while the rest of the sample is characterized by the high coercivity loop. In the 300TbIG/G sample the low coercivity loop layer was much thicker, and due to the absorption in the UV, the contribution to the MO spectra from the high coercivity loop was zero. At lower energies, the penetration depth was large enough to allow the light to interact with the bottom layer and thus contribution from both layers was observed. The analysis therefore revealed that for the samples with PMA, the

MOKE in polar configuration is not sensitive to the sublattice contributions, but to the different magnetic anisotropy of regions within the deposited layer. It was proposed that the sublattice contributions for samples with PMA could be visible in the longitudinal MOKE measurement since the magnetic field would point in the hard axis direction and therefore potentially revealing different sublattice behaviour.

Bibliography

[1] Bi, L., Hu, J., Jiang, P. et al., On-chip optical isolation in monolithically integrated non-reciprocal optical resonators. *Nat Photonics*, **5**(12), 758–762, doi:10.1038/nphoton.2011.270 (2011).

[2] Stadler, B. J. H. and Mizumoto, T., Integrated Magneto-Optical Materials and Isolators: A Review. *IEEE Photonics Journal*, **6**(1), 1–15, doi:10.1109/jphot.2013.2293618 (2014).

[3] Srinivasan, K., Zhang, C., Dulal, P. et al., High-Gyrotropy Seedlayer-Free Ce:TbIG for Monolithic Laser-Matched SOI Optical Isolators. *ACS Photonics*, **6**(10), 2455–2461, doi:10.1021/acsphotonics.9b00707 (2019).

[4] Born, M. and Wolf, E., *Principles of Optics*. 7th edn., Cambridge University Press, ISBN 1108477437 (2019).

[5] Malý, P., *Optika*. Karolinum, ISBN 978-80-246-1342-0 (2008).

[6] Nývlt, M., *Optical interactions in ultrathin magnetic film structures*. Ph.D. thesis, Charles University (1996).

[7] Azzam, R. M. A. and Bashara, N. M., *Ellipsometry and polarized light*. North-Holland Pub. Co., ISBN 0-7204-0694-3 (1997).

[8] Dupertuis, M. A., Acklin, B. and Proctor, M., Generalization of complex Snell–Descartes and Fresnel laws. *J. Opt. Soc. Am. A*, **11**(3), 1159, doi:10.1364/josaa.11.001159 (1994).

[9] Štefan Višňovský, *Optics in magnetic multilayers and nanostructures*. CRC Taylor & Francis, ISBN 0849336864 (2006).

[10] Zvezdin, A. K. and Kotov, V. A., *Modern magnetooptics and magnetooptical materials*. Institute of Physics Pub., ISBN 075030362X (1997).

[11] Yeh, P., Optics of anisotropic layered media: A new 4 × 4 matrix algebra. *Surf Sci*, **96**(1-3), 41–53, doi:10.1016/0039-6028(80)90293-9 (1980).

[12] Štefan Višovský, Magneto-optical ellipsometry. *Czech J Phys*, **36**(5), 625–650, doi:10.1007/bf01597496 (1986).

[13] Jellison, G. E. and Modine, F. A., Parameterization of the optical functions of amorphous materials in the interband region. *Appl Phys Lett*, **69**(3), 371–373, doi:10.1063/1.118064 (1996).

[14] Ferlauto, A. S., Ferreira, G. M., Pearce, J. M. et al., Analytical model for the optical functions of amorphous semiconductors from the near-infrared to ultraviolet: Applications in thin film photovoltaics. *J Appl Phys*, **92**(5), 2424–2436, doi:10.1063/1.1497462 (2002).

[15] Pershan, P. S., Magneto-Optical Effects. *J Appl Phys*, **38**(3), 1482–1490, doi:10.1063/1.1709678 (1967).

[16] Wittekoek, S., Popma, T. J. A., Robertson, J. M. et al., Magneto-optic spectra and the dielectric tensor elements of bismuth-substituted iron garnets at photon energies between 2.2-5.2 eV. *Phys Rev B*, **12**(7), 2777–2788, doi:10.1103/physrevb.12.2777 (1975).

[17] Kahn, F. J., Pershan, P. S. and Remeika, J. P., Ultraviolet Magneto-Optical Properties of Single-Crystal Orthoferrites, Garnets, and Other Ferric Oxide Compounds. *Phys Rev*, **186**(3), 891–918, doi:10.1103/physrev.186.891 (1969).

[18] Veis, M., *Optical interactions in thin films of selected magnetic oxides*. Ph.D. thesis, Charles University (2009).

[19] Waters, K., Mobley, J. and Miller, J., Causality-imposed (Kramers-Kronig) relationships between attenuation and dispersion. *IEEE Transactions on Ultrasonics, Ferroelectrics and Frequency Control*, **52**(5), 822–823, doi:10.1109/tuffc.2005.1503968 (2005).

[20] Aharoni, A., *Introduction to the Theory of Ferromagnetism*. Oxford University Press, ISBN 0198508093 (2001).

[21] Coey, J. M. D., *Magnetism and Magnetic Materials*. Cambridge, ISBN 0521816149 (2010).

[22] Blundell, S., *Magnetism in Condensed Matter*. Oxford University Press, ISBN 0198505922 (2001).

[23] Kosub, T., Kopte, M., Hühne, R. et al., Purely antiferromagnetic magnetoelectric random access memory. *Nat Commun*, **8**(1), doi:10.1038/ncomms13985 (2017).

[24] Marti, X., Fina, I., Frontera, C. et al., Room-temperature antiferromagnetic memory resistor. *Nat. Mater.*, **13**(4), 367–374, doi:10.1038/nmat3861 (2014).

[25] Finley, J. and Liu, L., Spintronics with compensated ferrimagnets. *Appl Phys Lett*, **116**(11), 110 501, doi:10.1063/1.5144076 (2020).

[26] Kim, S. K., Beach, G. S. D., Lee, K.-J. et al., Ferrimagnetic spintronics. *Nat. Mater.*, **21**(1), 24–34, doi:10.1038/s41563-021-01139-4 (2021).

[27] Fu, J., Hua, M., Wen, X. et al., Epitaxial growth of $Y_3F_5O_{12}$ thin films with perpendicular magnetic anisotropy. *Appl Phys Lett*, **110**(20), 202 403, doi:10.1063/1.4983783 (2017).

[28] Dieny, B. and Chshiev, M., Perpendicular magnetic anisotropy at transition metal/oxide interfaces and applications. *Rev Mod Phys*, **89**(2), 025 008, doi:10.1103/revmodphys.89.025008 (2017).

[29] Li, J., Ramanujam, B. and Collins, R., Dual rotating compensator ellipsometry: Theory and simulations. *Thin Solid Films*, **519**(9), 2725–2729, doi:10.1016/j.tsf.2010.11.075 (2011).

[30] Johs, B. and Hale, J. S., Dielectric function representation by B-splines. *Phys Status Solidi A*, **205**(4), 715–719, doi:10.1002/pssa.200777754 (2008).

[31] Néel, L., Pauthenet, R. and Dreyfus, B., Chapter VII The Rare Earth Garnets. In: *Progress in Low Temperature Physics*, pp. 344–383, Elsevier, doi:10.1016/s0079-6417(08)60155-9 (1964).

[32] Verma, R. K., Kumar, K. and Rai, S. B., Inter-conversion of Tb^{3+} and Tb^{4+} states and its fluorescence properties in MO–Al_2O_3: Tb (M = Mg, Ca, Sr, Ba) phosphor materials. *Solid State Sci*, **12**(7), 1146–1151, doi:10.1016/j.solidstatesciences.2010.04.004 (2010).

[33] Rosenberg, E. R., Beran, L., Avci, C. O. et al., Magnetism and spin transport in rare-earth-rich epitaxial terbium and europium iron garnet films. *Phys. Rev. Materials*, **2**(9), 094 405, doi:10.1103/physrevmaterials.2.094405 (2018).

[34] Dillon, J., Optical absorptions and rotations in the ferrimagnetic garnets. *J. Phys. Radium*, **20**(2-3), 374–377, doi:10.1051/jphysrad:01959002002-3037400 (1959).

[35] Clogston, A. M., Interaction of Magnetic Crystals with Radiation in the Range 10^4–10^5 cm^{-1}. *J Appl Phys*, **31**(5), S198–S205, doi:10.1063/1.1984665 (1960).

[36] Wood, D. L. and Remeika, J. P., Effect of Impurities on the Optical Properties of Yttrium Iron Garnet. *J Appl Phys*, **38**(3), 1038–1045, doi:10.1063/1.1709476 (1967).

[37] Scott, G. B., Lacklison, D. E. and Page, J. L., Absorption spectra of $Y_3Fe_5O_{12}$ (YIG) and $Y_3Ga_5O_{12}$: Fe^{3+}. *Phys Rev B*, **10**(3), 971–986, doi:10.1103/physrevb.10.971 (1974).

[38] Scott, G. B. and Page, J. L., The absorption spectra of $Y_3Fe_5O_{12}$ (YIG) and $Y_3Ga_5O_{12}$: Fe^{3+} to 5.5 eV. *Physica Status Solidi (b)*, **79**(1), 203–213, doi:10.1002/pssb.2220790121 (1977).

[39] Valiev, U. V., Gruber, J. B., Sardar, D. K. et al., Zeeman effect and stark splitting of the electronic states of the rare-earth ion in the paramagnetic terbium garnets $Tb_3Ga_5O_{12}$ and $Tb_3Al_5O_{12}$. *Phys. Solid State*, **49**(1), 91–98, doi:10.1134/s1063783407010167 (2007).

[40] Wemple, S. H., Blank, S. L., Seman, J. A. et al., Optical properties of epitaxial iron garnet thin films. *Phys Rev B*, **9**(5), 2134–2144, doi:10.1103/physrevb.9.2134 (1974).

[41] Jesenska, E., Yoshida, T., Shinozaki, K. et al., Optical and magneto-optical properties of Bi substituted yttrium iron garnets prepared by metal organic decomposition. *Opt. Mater. Express*, **6**(6), 1986, doi:10.1364/ome.6.001986 (2016).

[42] Fakhrul, T., Tazlaru, S., Beran, L. et al., Magneto-Optical Bi:YIG Films with High Figure of Merit for Nonreciprocal Photonics. *Adv. Opt. Mater.*, **7**(13), 1900 056, doi:10.1002/adom.201900056 (2019).

[43] Lacklison, D. E., Scott, G. B. and Page, J. L., Absorption spectra of Bi^{3+} and Fe^{3+} in $Y_3Ga_5O_{12}$. *Solid State Commun*, **14**(9), 861–863, doi:10.1016/0038-1098(74)90151-3 (1974).

[44] Kucera, M., Bok, J. and Nitsch, K., Faraday rotation and MCD in Ce doped yig. *Solid State Commun*, **69**(11), 1117–1121, doi:10.1016/0038-1098(89)90497-3 (1989).

[45] Xu, Y., Yang, J. H. and Zhang, X. J., Quantum theory of the strong magneto-optical effect of Ce-substituted yttrium iron garnet. *Phys Rev B*, **50**(18), 13 428–13 434, doi:10.1103/physrevb.50.13428 (1994).

[46] Gomi, M., Furuyama, H. and Abe, M., Strong magneto-optical enhancement in highly Ce-substituted iron garnet films prepared by sputtering. *J Appl Phys*, **70**(11), 7065–7067, doi:10.1063/1.349786 (1991).

[47] Kumar, N., Kim, N. G., Park, Y. A. et al., Epitaxial growth of terbium iron garnet thin films with out-of-plane axis of magnetization. *Thin Solid Films*, **516**(21), 7753–7757, doi:10.1016/j.tsf.2008.05.032 (2008).

[48] Scott, G. B., Lacklison, D. E., Ralph, H. I. et al., Magnetic circular dichroism and Faraday rotation spectra of $Y_3Fe_5O_{12}$. *Phys Rev B*, **12**(7), 2562–2571, doi:10.1103/physrevb.12.2562 (1975).

[49] Visnovsky, S., Canit, J. C., Briat, B. et al., Magnetic circular dichroism study on YIG films. *Journal de Physique*, **40**(1), 73–77, doi:10.1051/jphys:0197900400107300 (1979).

[50] Umezawa, H., Yokoyama, Y. and Koshizuka, N., Temperature dependence of Faraday rotation in Bi-substituted terbium iron garnet films. *J Appl Phys*, **63**(8), 3113–3115, doi:10.1063/1.340859 (1988).

[51] Vien, T. K., Gall, H. L., Lepaillier-Malécot, A. et al., Magnetooptical and magnetic properties of terbium iron garnet at low temperatures. In: *AIP Conference Proceedings*, AIP, doi:10.1063/1.30041 (1975).

[52] Allen, G. A. and Dionne, G. F., Accurate analysis of the magneto-optical permittivity tensor of $Y_3Fe_5O_{12}$. *J Appl Phys*, **93**(10), 6951–6953, doi:10.1063/1.1555873 (2003).

[53] Doormann, V., Krumme, J.-P. and Lenz, H., Optical and magneto-optical tensor spectra of bismuth-substituted yttrium-iron-garnet films. *J Appl Phys*, **68**(7), 3544–3553, doi:10.1063/1.346314 (1990).

[54] Dulal, P., Block, A. D., Gage, T. E. et al., Optimized Magneto-optical Isolator Designs Inspired by Seedlayer-Free Terbium Iron Garnets with Opposite Chirality. *ACS Photonics*, **3**(10), 1818–1825, doi:10.1021/acsphotonics.6b00313 (2016).

[55] Dionne, G. F. and Allen, G. A., Spectral origins of giant Faraday rotation and ellipticity in Bi-substituted magnetic garnets. *Journal of Applied Physics*, **73**(10), 6127–6129, doi:10.1063/1.352723 (1993).

[56] Dionne, G. F. and Allen, G. A., Molecular-orbital analysis of magneto-optical Bi-O-Fe hybrid excited states. *J Appl Phys*, **75**(10), 6372–6374, doi:10.1063/1.355353 (1994).

[57] Deb, M., Popova, E., Fouchet, A. et al., Magneto-optical Faraday spectroscopy of completely bismuth-substituted $Bi_3Fe_5O_{12}$ garnet thin films. *J. Phys. D: Appl. Phys.*, **45**(45), 455 001, doi:10.1088/0022-3727/45/45/455001 (2012).

[58] Zanjani, S. M. and Onbaşlı, M. C., Predicting new iron garnet thin films with perpendicular magnetic anisotropy. *J Magn Magn Mater*, **499**, 166 108, doi:10.1016/j.jmmm.2019.166108 (2020).

[59] Ortiz, V. H., Aldosary, M., Li, J. et al., Systematic control of strain-induced perpendicular magnetic anisotropy in epitaxial europium and terbium iron garnet thin films. *APL Materials*, **6**(12), 121 113, doi:10.1063/1.5078645 (2018).

List of Figures

1 Structure of a non-reciprocal MO isolator. Taken from [1]. 3
2 Spectral dependence of the transmission for two senses of circular polarization. Taken from [1]. 4

1.1 The polarization ellipse. 8
1.2 Examples of a) linear polarization and b) LCP. 9
1.3 Basic configurations of measuring MOKE. 12

2.1 Reflection and refraction at an interface, field orientations. 13
2.2 Reflection and transmission coefficients for $n_1 = 1$, $n_2 = 1.5$ (left), reflection coefficients for $n_1 = 1.5$, $n_2 = 1$ (right). 14
2.3 Multilayer structure consisting of N layers surrounded by 0 and $N + 1$ half-spaces. 18
2.4 Spectral dependence of the diagonal permittivity tensor element near resonance according to the Lorentz model. 22
2.5 Spectral dependence of the diagonal permittivity tensor element according to the Drude model. 23
2.6 Splitting of energy levels for a) type I and b) type II transitions. . 23
2.7 Two types of line shapes contributing to the off-diagonal permittivity: a) type I (diamagnetic), b) type II (paramagnetic). . 24

3.1 Schematic illustration of various magnetically ordered materials. . 28
3.2 Typical temperature dependence of the magnetization of a ferromagnet. 28
3.3 Hysteresis loop of a ferromagnet. 29
3.4 Temperature dependence of magnetization of a ferrimagnet with two sublattice magnetizations M_1 and M_2. 30
3.5 Hysteresis loop along the easy (left), and hard (right) axis. 31
3.6 Anomalous ferrimagnetic hysteresis loop visible in MOKE or Faraday effect. 31

4.1 Ellipsometer setup with two rotating compensators. 33
4.2 Rotating analyzer technique for measuring MOKE spectra. Faraday configuration is similar, with waveplate, analyzer and detector behind the sample. 33
4.3 The principle of PLD. High-energy laser pulses evaporate the target material creating a plasma plume that deposits on the heated substrate. 35

5.1 One octant of garnet structure, rare-earth ion (blue) in dodecahedral site, iron ions (orange) in tetrahedral and octahedral sites. 37

6.1 SE data and model of the sample 123TbIG/G. 39
6.2 Decomposition of the spectral dependence of imaginary part of diagonal element of permittivity tensor into Tauc-Lorentz oscillators for the sample 123TbIG/G. 40

6.3 Fit relative permittivity of the non-doped TbIG samples. 41
6.4 Fit relative permittivity of the samples Bi0.5TbIG/G and Bi0.06TbIG/G compared with sample 123TbIG/G. 43
6.5 Fit relative permittivity of the samples Ce0.7TbIG/G and Bi0.01TbIG/S compared with the sample 123TbIG/G. 43
6.6 Faraday rotation and ellipticity of GGG. 44
6.7 Measured Faraday rotation and ellipticity of non-doped TbIG on GGG substrate. 45
6.8 Measured Kerr rotation and ellipticity of 123TbIG/G with polished and roughened backside. 46
6.9 Measured Kerr rotation and ellipticity of 300TbIG/G with polished and roughened backside. 46
6.10 Measured Kerr rotation and ellipticity of non-doped TbIG on Si substrate. 47
6.11 Calculated real part of off-diagonal permittivity of TbIG from all measurements of all samples. The Φ_K and Φ_F labels indicate which spectra were used for calculation. 48
6.12 Calculated imaginary part of off-diagonal permittivity of TbIG from all measurements of all samples. The Φ_K and Φ_F labels indicate which spectra were used for calculation. 49
6.13 Measured MOKE spectra of the sample Bi0.01TbIG/S. 49
6.14 Measured Faraday rotation and ellipticity spectra of doped samples on GGG substrate. 50
6.15 Calculated real part of off-diagonal permittivity of TbIG from MOKE and Faraday measurements. The Φ_K and Φ_F labels indicate which spectra were used for calculation. 50
6.16 Calculated imaginary part of off-diagonal permittivity of TbIG from MOKE and Faraday measurements. The Φ_K and Φ_F labels indicate which spectra were used for calculation. 51
6.17 Measured Kerr rotation spectral hysteresis loops of the sample 300TbIG/G. The top graph illustrates the spectral shape with colour coded applied external field values. The lower graphs depict slices through the spectrum at energies $E = 2.81\,\text{eV},\ 2.84\,\text{eV}$ and $2.87\,\text{eV}$. 52
6.18 Measured Kerr rotation spectral hysteresis loops of the sample 123TbIG/G. The top graph illustrates the spectral shape with colour coded applied external field values. The lower graphs depict slices through the spectrum at energies $E = 2.38\,\text{eV},\ 2.8\,\text{eV}$ and $4\,\text{eV}$. 53
6.19 Measured Kerr rotation spectral hysteresis loops of the sample Bi0.5TbIG/G. The top graph illustrates the spectral shape with colour coded applied external field values. The lower graphs depict slices through the spectrum at energies $E = 2.74\,\text{eV},\ 3.16\,\text{eV}$ and $4\,\text{eV}$. 54
6.20 Decomposition of the measured Kerr hysteresis loops of the sample 300TbIG/G shown at two energies $E = 2.64\,\text{eV}$ and $2.84\,\text{eV}$. 55
6.21 Spectral dependence of the amplitude of the two loops that reproduce the measured Kerr spectrum of the sample 300TbIG/G. 55

6.22 Spectral dependence of the amplitude of the two loops that reproduce the measured Kerr spectrum of sample 123TbIG/G. The low $H_C$and high $H_C$loops have the same hysteresis shape as for the sample 300TbIG/G (Fig. 6.20). 56
6.23 Spectral dependence of the amplitude of the two loops that reproduce the measured Kerr spectrum of sample Bi0.5TbIG/G. The low $H_C$and high $H_C$loops have the same hysteresis shape as for the sample 300TbIG/G (Fig. 6.20). 56

List of Acronyms

CF crystal field. 41, 42

CT charge transfer. 41, 42

EM electromagnetic. 5, 17, 19, 21

EMA effective medium approximation. 32

GGG gadolinium gallium garnet. 4, 37, 39, 42, 44, 45, 47–50, 54, 58, 66

IR infrared. 41, 43, 44, 47, 48, 58

LCP left-handed circular polarization. 8, 9, 16, 22, 23, 65

MBE molecular beam epitaxy. 35

MO magneto-optical. 3, 4, 15, 23, 31, 33, 34, 37, 41, 43, 47, 48, 50, 51, 58, 65

MOKE magneto-optical Kerr effect. 11, 12, 31, 33, 34, 39, 44–51, 56–59, 65, 66

MSE mean square error. 33, 39

PLD pulsed laser deposition. 35, 42, 47, 65

PMA perpendicular magnetic anisotropy. 31, 54, 55, 57–59

RCP right-handed circular polarization. 8, 9, 16, 22, 23

SE spectroscopic ellipsometry. 32, 39, 42, 44, 55, 65

TbIG terbium iron garnet. 4, 37, 39–45, 47–51, 54–56, 66

UV ultraviolet. 41–44, 53, 58

YIG yttrium iron garnet. 37, 41, 42, 47, 48, 58